Power absorption mechanisms and energy transfer in X-ray gas attenuators

Martín Ortega Álvaro

Communauté
UNIVERSITÉ Grenoble Alpes

THÈSE

Pour obtenir le grade de

DOCTEUR DE L'UNIVERSITÉ GRENOBLE ALPES

Spécialité : **Physique de la Matière Condensée et du Rayonnement**

Arrêté ministériel : 7 Août 2006

Présentée par

Álvaro Martín Ortega

Thèse dirigée par **Manuel Sánchez del Río**
et co-encadrée par **Yves Dabin**

préparée au sein **ESRF, The European Synchrotron**
et de **École Doctorale de Physique**

Power absorption mechanisms and energy transfer in X-ray gas attenuators

Thèse soutenue publiquement le **19 Janvier 2017**,
devant le jury composé de :

M. Manuel Sánchez del Río
HDR, ESRF Grenoble, Directeur de thèse

Mme. Ana Lacoste
Professeur à L'Université Grenoble Alpes, Présidente

M. Thierry Belmonte
Professeur, Université de Lorraine, Rapporteur

M. Jean-Pierre Boeuf
Professeur, Université Toulouse III Paul Sabatier, Rapporteur

M. Veijo Honkimaki
ID31 Beamline scientist, ESRF Grenoble, Invité

M. Yves Dabin
Group leader of AAM group, ESRF Grenoble, Invité

Acknowledgements

I would like to start thanking my supervisors at the ESRF, Lin Zhang and Yves Dabin, for giving me the opportunity to work in a laboratory as excellent as the ESRF.

Also, I would like to thank Manuel Sánchez del Río, of the Advance Analysis and Modelling group of the ESRF, for his constant availability, his advices and his invaluable help during these years.

I would like to thank M. Jean-Pierre Boeuf, professor at the Université Paul Sabatier, and to Thierry Belmonte, professor and the Université de Lorraine, for accepting being reporters of this thesis and participating in the jury.

Special acknowledgement for the members of the CRPMN of the LPSC: Ana Lacoste, professor at the Grenoble Alpes University; Stéphane Béchu, chargé de de recherche, and Alexandre Bès, ingénieur de recherche. I started this thesis with little knowledge of plasma and without them I still would know as much. Their guidance and collaboration in the diagnosis of the plasma was essential to the results are here presented, as well as their help in understanding what gas going on in the gas attenuator. It was a privilege to work with them.

I also would like to thank M. Tiberiu Minea, professor at the Université Paris-Saclay, for his help during the set-up and implementation of the theoretical model, avoiding me so many hidden pitfalls and enabling the understanding the results.

Thanks to the ID06 staff and in particular to Carsten Detlefs, beamline scientist, and Pierre Wattechamps, beamline technician, for their invaluable help during the setup, the operation of the experiment and their patience explaining how to do all of it myself.

I would like to thank Vincenzo Grilli, technician at the Front End group, for taking care of all the vacuum and mechanical details that he manages so well. Without him I still would be trying to fix the first leak.

I acknowledge also the collaboration of the Réseau des Plasma Froids for the use of their tunable diode lasers.

I also gratefully acknowledge the invaluable help of Nader Sadeghi during the setup, performance and interpretation of the diode lasers diagnosis. His experience made a difference and it was a privilege to work with him.

I would like to thank all my friend from the ESRF with whom I have spent so many good moments, for making the stay at the ESRF and in Grenoble an amazing experience. Also to my parents to support me since the crazy moment I decided to be a physicist.

And to Cristina - for making everything to make sense.

Abstract

The work done in the context of this thesis focuses in the study of an X-ray gas attenuator and the plasma produced within. An X-ray gas attenuator consists on a vessel filled with gas, usually argon or krypton at a few hundreds millibars, that absorbs the low energy fraction of a synchrotron X-ray spectrum, reducing the power received by downstream optical elements without affecting the properties of the high energy part of the spectrum. The absorption of the photons creates a region of hot, ionized gas around the X-ray beam path, decreasing locally the gas density. A detailed energy balance between all the involved processes is required to be able to predict the absorption and operate and design gas attenuators efficiently. A hybrid model combining Monte Carlo and fluid modelling techniques has been developed to determine the energy balance and simulate the X-ray absorption. The model has been validated by experimental studies including power absorption, optical emission spectroscopy and tunable laser absorption spectroscopy. The results of both simulation and experiments show a plasma confined around the X-ray beam path, recombining in the bulk of the gas and with a maximum temperature of several hundreds of Kelvin. The model was able to predict the X-ray absorption within a 10-20% of error, which allows its use as a first approximation for the design and operation of gas attenuators, and also provides a starting point for more refined models.

Résumé

Le travail effectué dans le cadre de cette thèse porte sur l'étude d'un atténuateur de rayonnement X à gaz et du plasma produit à l'intérieur. Un atténuateur a gaz et composé d'un chambre rempli du gaz, généralement argon ou krypton à quelques centaines de millibars, qui absorbe la partie de basse énergie d'un spectre de rayonnement X de synchrotron, en réduisant la puissance reçu par les éléments optiques en aval sans affecter les propriétés de la partie de haute énergie du spectre. L'absorption des photons crée une région de gaz chaud et ionisé autour du parcours du faisceau X, en réduisant la densité du gaz localement. A détaillé bilan énergétique entre tous les processus impliqués c'est nécessaire pour être capable de prédire l'absorption et opérer et dessiner atténuateurs a gaz efficacement. Un modèle hybride que combine techniques de modélisation Monte Carlo et fluides à été développé pour déterminer le bilan énergétique et simuler l'absorption de rayonnement X. Le modèle a été valide expérimentalement pas études incluant absorption de puissance, spectroscopie optique d'émission et spectroscopie d'absorption par laser à diodes. Les résultats des simulation et expériences montre un plasma confiné autour du parcours du faisceau X, recombinant dans le volume de gaz et avec une température maximale de plusieurs centaines de Kelvin. Le modèle a été capable de prédire l'absorption de rayons X avec un erreur de entre 10 et 20%, qui permettre son utilisation comme première approximation pour le dessin et opération de atténuateurs a gaz et aussi comme point de partie pour modèles plus affinées.

Contents

Chapter 1

Introduction

1.1 X-ray synchrotron facilities

The objective of synchrotron radiation facilities like the ESRF is to provide to the scientific community brilliant X-ray sources with high intensity, low divergence and small bandwidth. The photon energy range depends on the specific facility and beamline; at the ESRF, it varies from the 0.3-1.6 keV range of ID32 to the 21-150 keV range of ID31. The applications include a large number of fields, like protein crystallography, materials science, micro and nanotechnology, study of soft matter systems, tomography of palaeontological and cultural heritage samples, or biomedical studies. The number of synchrotron sources is still growing, as shows the recent construction and commissioning of MAX IV in Denmark, NSLS-II in Brookhaven (New York) or the upgrade programs of the ESRF [1] and the APS (Chicago) [2], which aim to increase the brightness and coherence of the available X-ray beams. A side effect of these upgrades is that the emitted power density

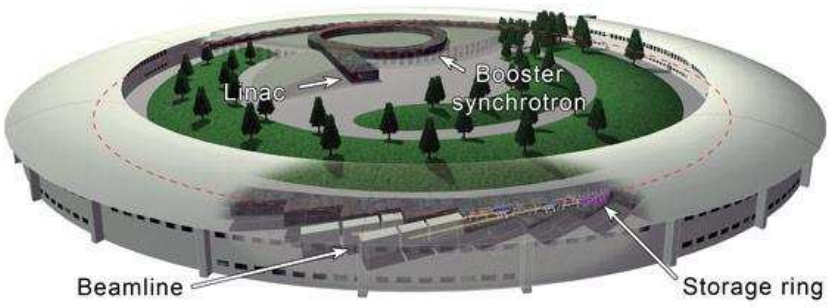

Figure 1.1: ESRF acceleration scheme: linac, booster synchrotron and storage ring.

is increased, up to hundreds of watts per square millimetre and a few kilowatts of total power. This originates a large stress on the optical elements of the beamlines, requiring active cooling systems and power absorption schemes to maintain the elements in working conditions. The objective of a gas attenuator is to contribute to reduce the power of the X-ray beam before reaching these optical elements. The conclusions of this work might also be applicable to gas attenuators working on free electron laser facilities like the XFEL, where an X-ray beam with a much larger instantaneous power but a similar average power and photon energy range.

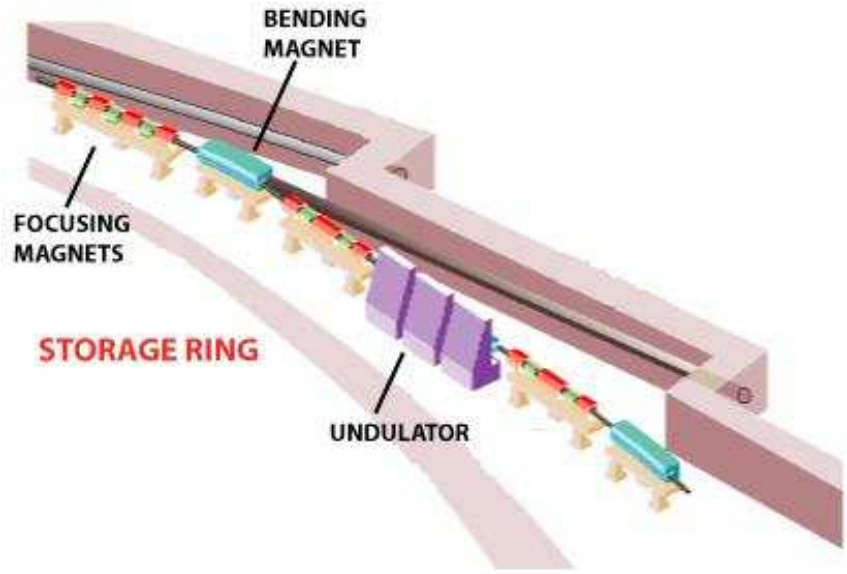

Figure 1.2: Scheme of one of the cells on the ESRF: focusing magnets (quadrupole, sextupoles and octupoles) before and after every bending magnet (BM, light blue) and insertion device (ID, purple). The X-rays are emitted tangent to the electrons trajectory in the BMs and IDs.

The first step in the generation of a synchrotron X-ray beam is the generation of a relativistic electron beam. At the ESRF (figure 1.1), the electron beam starts in a linac (linear accelerator), where the electrons are extracted from a metallic surface and are accelerated up to 200 MeV. The electrons are then injected in a "synchrotron booster", where they are accelerated from the initial 200 MeV up to the final operating energy of 6 GeV. The electron beam is then finally injected in the "storage ring", a closed circuit where the electrons circulate at a constant energy and where the sources of the X-ray beams are placed. The storage ring itself is made of 32 sections (figure 1.2), each of them

composed of a bending magnet (BM) section where the trajectory of the electrons is modified, and a straight section in which the so-called insertion devices (ID) are placed. Both bending magnets and insertion devices may work as X-ray sources. In addition, a series of quadrupole, sextupole and octupole magnets keep the electron been focused between the bending magnets and the straight sections.

The X-ray beam emitted by each source enters then the corresponding beamline. The first cabin is the optical hutch, where the beam is conditioned for its use in the experimental station (figure 1.3). Typically the optical hutch includes several slits to control the size of the beam, a monochromator to select a defined energy or wavelength from the incoming spectrum, absorbers and mirrors to reduce the power incoming to the monochromator, and focusing mirrors to control the focus of the beam. The beam continues then to the experimental hutch (or hutches), where the sample under study is placed, together with the relevant detectors and occasionally further optical elements. The control of the whole beamline is made remotely to prevent irradiation of the personnel carrying on the experiment.

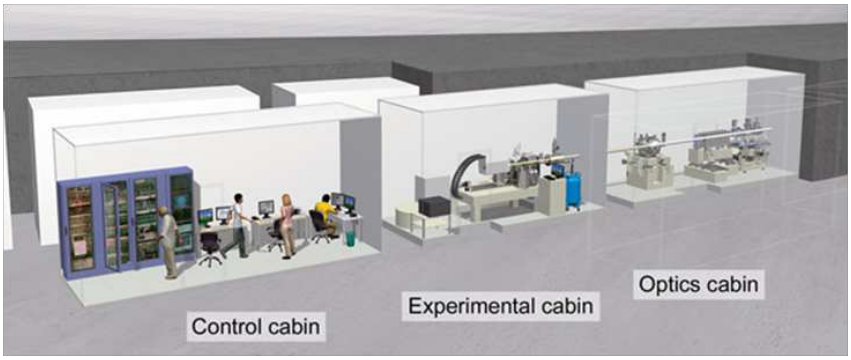

Figure 1.3: Scheme of a typical beamline. The white beam (power) attenuators are placed in the optical hutch, upstream of mirrors or monochromators.

1.2 X-ray sources

The radiation emitted by both bending magnets and insertion devices is based in the same principle: the radial acceleration of an electron in perpendicular to its trajectory. This is achieved by placing a magnetic field also perpendicular to the trajectory, so that

the Lorentz force $\vec{F} = q\vec{v} \times \vec{B}$ provides the acceleration of the electron. At low velocities, the electromagnetic field emitted by an accelerated particle is emitted almost isotropically around the acceleration [3, 4]; however, at relativistic energies the radiation field is bent forward into a small cone of angle $1/\gamma$ rad aperture, where $\gamma = \sqrt{1 - v^2/c^2}$ (equal to 11780 at the ESRF). Of course, if the electron emits continuously while its trajectory changes, the aperture in the plane of the trajectory will be larger. This is exactly how bending magnets work: a constant, usually vertical magnetic field is placed in the electron trajectory, changing it to keep the electron in a closed orbit and emitting radiation in the process, as shown in figure 1.4a. The emitted radiation has a broad spectrum (figure 1.5) that goes from the infrared to the X-ray energies. The characteristic wavelength of this radiation is defined as the wavelength which divides the spectrum in two halves of equal power, and it is given by

$$\lambda_c = \frac{4\pi\rho}{3\gamma^3} \tag{1.1}$$

where ρ is the local radius of the electron trajectory and c the light velocity. In the case of the ESRF bending magnets, it corresponds to 0.5 Å, or 24.8 keV in energy units. The total power emitted by horizontal solid angle by a bending magnet is given in practical units by

$$\frac{dP}{d\theta} = 14.08\frac{E^4 I_b}{\rho} \tag{1.2}$$

where I_b is the electron current in mA, E the electron kinetic energy in keV and ρ the curvature radius in m. For the ESRF bending magnets it corresponds to 146 W/mrad.

An insertion device is based in the same principle, but instead of having a constant magnetic field, a series of magnets are arranged so that the direction of the field changes

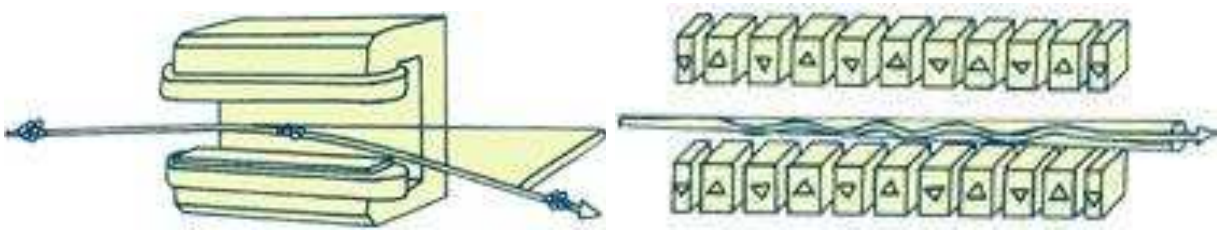

(a) (b)

Figure 1.4: Scheme of the working principle of an undulator (a) and of a bending magnet (b)

alternatively between up-down to down-up with a given spatial period λ_u. The resulting electron trajectory becomes oscillating, with every turn emitting radiation. An important parameter in these devices is the K parameter, the ratio of the aperture of the trajectory to the aperture of the emitted radiation, given by

$$K = \frac{B_0 e \lambda_u}{2\pi m_0 c} \tag{1.3}$$

where B_0 is the magnetic field, λ_u the spatial period of the magnetic field, e and m_0 the electron charge and mass and c the speed of light. If K is much larger than one, the angle of the electron trajectory is much larger than that of the emitted radiation, and there is no interference phenomena. In this case, the resulting spectrum has the same shape as a bending magnet one (figure 1.5), with the total intensity increased due to the multiple turns. The devices emitting this kind of radiation are usually called wigglers. On the other hand, if K is around or smaller than one, the radiation emitted on every turn will interfere with each other, resulting in a spectrum with sharp peaks, or harmonics, at certain wavelengths. The wavelength of the first harmonic is given by

$$\lambda_1 = \frac{\lambda_u \left(1 + K^2/2\right)}{2\gamma^2} \tag{1.4}$$

with the following harmonics having wavelengths which are integer fractions of this value, $\lambda_1 = \lambda_u / n$. These devices are usually called undulators. The wavelength of the harmonics can be adjusted by changing the strength of the magnetic field. In practice, this is done by changing the separation, or gap, of the magnets generating the magnetic field. A closer gap will mean a stronger magnetic field and a higher K value, while a more open gap will mean weaker magnetic field and smaller K. The total power emitted by the insertion devices, both wigglers and undulators, is given by

$$P_T = \frac{N}{6} Z_0 I e \frac{2\pi c}{\lambda_u} \gamma^2 K^2 \tag{1.5}$$

where N is the number of turns and Z_0 the vacuum impedance. The power emitted by insertion devices is usually much larger than that of a bending magnet. For instance, the source used in the studies of this thesis is a ESRF U18 undulator (U18 standing form

the 18 mm of period of the magnetic structure), that at its closest gap of 6 mm emits a total power of 770 W through an aperture of 2x2 mm at 30 m from the source. Wigglers emit even higher power due to the usually stronger magnetic field; the source used in the biomedical beamline of the ESRF, ID17, can deliver at its minimum gap a total power of 19.3 kW [5]. It is clear from these values that some power handling will be required in the optical elements of the beamline.

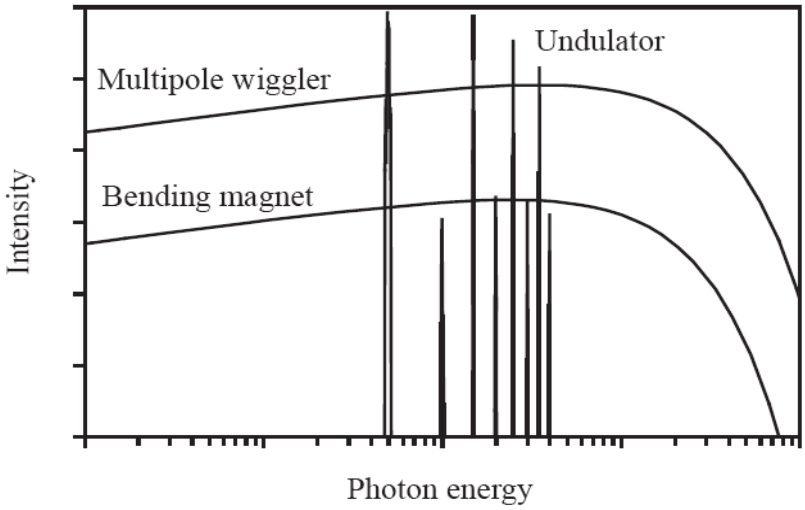

Figure 1.5: Schematic spectra of X-ray beams generated in a bending magnet, in an undulator and in a wiggler.

1.3 Monochromator and absorption schemes

One important element in almost every synchrotron beamline is the monochromator, which selects the operating energy and rejects the rest of the X-ray spectrum. An X-ray monochromator is based in the diffraction of the photons by a single crystal, usually silicon, according to Bragg's diffraction law:

$$n\lambda = 2d\sin(\theta) \tag{1.6}$$

where λ is the photon wavelength, d the interatomic distance of the diffracting planes, θ the diffraction angle and n the order of the diffraction. In practice, all monochromators operate in the first order of diffraction. To maintain the direction of the X-ray beam and

decrease the bandwidth, most monochromators are made up of two parallel blocks (figure 1.6), so that only the photons of the selected energy will maintain the original direction. Additional decrease of bandwidth can be achieved by adding another pair of crystals, in what is known as a 4-bounce monochromator.

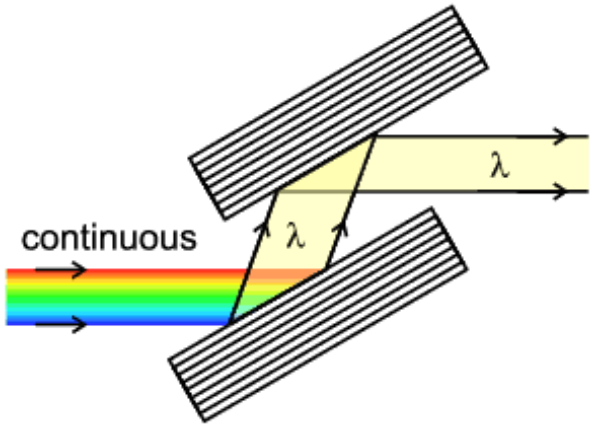

Figure 1.6: Principle of operation of a Double Crystal Monochromator (DCM). Every wavelength is diffracted from the first crystal at a different angle; the second crystal, parallel to the first one, allows a single wavelength to be transmitted parallel to the incident beam.

Given the small transmission bandwidth of arround 10^{-4} for silicon monochromators and the broad spectra coming from both bending magnets and insertion devices, virtually all the emitted power is either absorbed by the first crystal of the monochromator or re-emitted to the surroundings. The fraction of power absorbed as heat load is determined by the mass-energy absorption coefficient. This heat load not only heats up the crystal but also deformates the surface by thermal expansion in the footprint of the X-ray beam [6, 7]. This deformation will make the X-ray beam to diffract in different directions, according to the local angle of incidence, increasing the divergence of the beam and decreasing the transmission after the diffraction in the second crystal. To prevent this effect, specially designed cooling schemes are applied to the first crystal to minimize the deformation of the surface. Still, these cooling schemes also reach a limit, above which a higher incoming photon flux results in a decrease of the output flux with lower performance.

To reduce the heat load on the monochromator without reducing the photon flux, two basic options are available: mirrors and attenuators. An X-ray mirror takes advantage of

the lower-than-one index of refraction of most materials at the X-ray energy, so that they can operate in total reflection at very small angles. If the index of refraction is given by $n = 1 - \delta + i\beta$, the critical angle at which total reflection starts is

$$\theta_c = \sqrt{2\delta} \tag{1.7}$$

with the total reflection occurring at angles $\theta < \theta_c$. The parameter δ is small (10^{-5} - 10^{-6} for typical X-ray mirror materials) and decreases as the photon energy increases, so that for a fixed angle, there is an energy above which there is no external total reflection. This property allows to use the mirror as a low-pass filter, removing the high energy components from an undulator or bending magnet spectrum without affecting the low energy ones; part of the power is absorbed by the mirror and the rest is sent to the monochromator. Because of the small angle of incidence, the footprint of the beam is rather large and the cooling requirements of the mirror easier to provide. This method is useful if the energy after the monochromator corresponds to the firsts harmonics of an undulator or to the lower energy part of a bending magnet or wiggler.

An attenuator takes advantage of the energy dependence of the X-ray absorption of the materials. The absorption of a photon beam passing through a material is given by the Beer-Lambert law

$$I = I_0 \exp(-\rho\sigma z) \tag{1.8}$$

where I_0 is the incident beam intensity, ρ the material density, σ the cross section and z the length of the material. In general, the cross section decreases as the photon energy increases, so that the low energy photons are more absorbed that the high-energy ones. A solid attenuator takes advantage of this effect by placing a slab of material of fixed thickness in the beam path, operating as a high-pass filter so that the low energy components of the white beam are absorbed and the high energy ones transmitted. This method is useful when the monochromator is working at the higher energy harmonics of an undulator, or in the high-energy section of a bending magnet or wiggler spectra. However, the solid attenuator scheme has a number of drawbacks that can be avoided by using a gas attenuator.

1.4 Motivation for a gas attenuator

The main drawback of a solid attenuator is that it has an upper limit on the maximum absorbed power, given by the material choice and the cooling system. At higher powers, the material may reach its melting point. Also, the thermal stresses and thermal cycles at which the material is exposed can damage the bulk or the surfaces of the material, reducing the quality of the transmitted beam. Finally, the absorption ratio is fixed and given by the slab thickness, so that a tunable attenuation can be achieved only by using a number of attenuators with different slab thickness.

A gas attenuator avoids these disadvantages by using a gas as the absorbing medium. A gas is not subject to thermal or mechanical stresses, so that there is no maximum operation temperature; only the walls of the gas chamber require cooling. Likewise, there is no stress associated to the cycles at which the attenuator is exposed. In addition, the X-ray absorption can be controlled my changing the gas pressure, which in turn changes the gas density following the ideal gas law:

$$pV = nRT \tag{1.9}$$

However, some disadvantages exist when operating a gas attenuator. The main one is that the heating of the gas around the X-ray beam path creates a large temperature and density gradient between the beam path and the walls, so that the local temperature is higher than the average one and the local density is lower than average one. The result is that the X-ray absorption, depending on the gas density, cannot be calculated directly from the initial, average gas density. A pressure jump is also usually observed, corresponding to the increase of the average gas temperature. The height of this jump depends on the total volume available to the gas and on whether the gas is continuously pumped or kept stationary and at constant volume.

A few instances of gas attenuators exist today both in synchrotrons and free electron laser facilities. The gas attenuator at LCSL II in Standford, USA [8] consist on a cylinder of 5 m length, 20 mm of diameter, a gas feeding section in the center of the cylinder and

differential pumping sections at the ends to isolate the rest of the beamline, under vacuum. In this case the gas flows continuously through the system. Another examples are those of the gas attenuators used at the ESRF. The one in the biomedical beamline ID17 [5] consist on a 2.2 m long cylinder with beryllium windows at the ends. A different one was designed for ID15 and ID31 [9], consisting on a 1 m long cylinder and diamond windows and it is connected to a variable belly to control the gas pressure by changing the volume of the system (figure 1.7). There is no gas flow in the ESRF attenuators, so that the amount of gas on the system remains constant. Noble gases (argon or krypton) are used to avoid the formation of any reactive species after the irradiation which might damage the windows of the attenuator. The gas attenuator used in this study is described in detail in chapter 2.

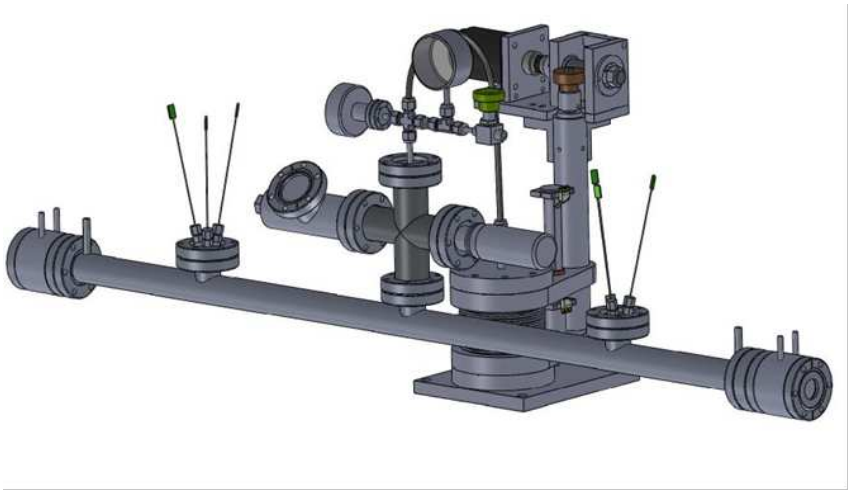

Figure 1.7: Gas attenuator designed for the ID15 and ID31 beamlines of the ESRF [9]. The belly behind the cylindrical gas chamber allows to modify the total volume available and therefore the gas pressure.

To be able to predict the X-ray absorption from a gas attenuator one can not use directly the initial gas pressure but must take into account self-consistently the effect of the gas heating on the power absorption and conversely. This model must include not only the thermal effects but also the power dissipated by scattered and fluorescent radiation, that does not contribute to the gas heating but accounts for part of the power absorbed from the X-ray beam. In addition, the ionization in the gas following the photon absorption and the emission of high energy (>100 eV) electrons will lead to the formation of a plasma in the gas attenuator, which must also be taken into account in the

model. To our knowledge, few studies have been made on gas attenuators, and none of them have considered the plasma phenomena that plays an important role in the power transfer mechanisms. Experimentally, the studies have focused on the power absorption itself and the changes on pressure [5, 9]. Theoretically, the models have only considered the gas flow in windowless attenuators and the heat dissipation without including the plasma physics, only from the thermal point of view [8, 10]. The objective of this thesis is to carry a study including the measurement of some of the plasma properties and to develop a self-consistent model describing the X-ray absorption, plasma physics and heat transfer and to be able to predict the power absorption in existing and future attenuators.

1.5 Plasma physics in the context of a gas attenuator

The plasma created in the gas attenuators is generated first by the photoionization of the gas atoms by the X-rays, followed by the emission of fast photoelectrons and Auger electrons, with energies in the order of hundreds of eV up to a few keV. These fast electrons will interact rapidly with the surrounding gas, further ionizing it. The gas pressure of the attenuator under study, between 10 and 500 mbar, is high enough to ensure that the slow-down of fast electrons will occur in a very small region around the X-ray beam path. There is no external electric field applied to the attenuator, so that once an electron has lost most of it energy it will only diffuse towards the walls or recombine in the bulk of the gas. The only exception to this rule are the electron-electron collisions, in which an electron still might gain some energy at the expense of the other one. Even in this case, the total energy of the population remains constant.

A plasma with similar characteristics, regarding the absence of external fields and the presence of fast-energy electrons, are those created by electron beams [11]. The principal electron loss mechanisms in this kind of plasmas are the diatomic and triatomic recombination, in which the electrons recombine with molecular ions, which are then dissociated. This mechanism is dominant due to the high pressure of the gas in the order of hundreds of mbars, which allows the conversion from atomic to molecular ions. Diffusion is

also expected to be weak, again due to the high gas pressure. Another related plasma is that created after the interaction of an Extreme Ultra Violet (EUV) pulse in a gas of a few mbars of pressure, a kind of plasma of interest in the microelectronic industry. A experimental study in this plasma [12] showed that the electron population cools down to the gas temperature within a few μs after the arrival of the pulse. While in our case the photon source will be continuous, the gas pressure will also be higher, so that we should expect a more efficient thermalization and therefore a low electron temperature.

The study of the gas attenuator included both an experimental study and the development of a model of the X-ray absorption. The experimental study, described in chapter 2, included the measurement of the power absorption and the radial distribution of the excited species of the gas by means of Optical Emission Spectroscopy (OES) and Tunable Laser Absorption Spectroscopy (TLAS). The developed model included a Monte Carlo model, described in chapter 3 to treat the photon absorption and the slow-down of fast electrons, and a fluid model described in chapter 4 accounting for the diffusion and recombination of the plasma as well as the heat transfer. The results of the model are compared to those of the experimental studies in chapter 5. Finally, the conclusions of the thesis are shown in chapter 6

Chapter 2

Experimental studies

The main objective of the experimental studies is to measure the X-ray transmission and absorption of the attenuator for different operation conditions, namely gas pressure and X-ray beam properties. The transmission is determined by the Beer-Lambert law

$$\frac{dI(E)}{dz} = -I(E)\sigma(E)\rho(z) \tag{2.1}$$

where σ is the total photon cross section of the gas, ρ is the gas density, $I(E)$ is the beam intensity, E is the photon energy and z is the position along the beam trajectory. The cross section for these processes is well known, with the possible oscillations near the absorption edges not changing the integral value for all the energies. Only the gas density may change due to heating by the absorption of the X-rays; by measuring the transmission through the attenuator we can obtain the gas density and the absorbed power. However, these measurements will provide only an average value, with no insight on the local values or radial profile of the different gas and plasma parameters. To obtain spatially resolved information, two different techniques will be used here: Optical Emission Spectroscopy (OES) and Tunable Laser Absorption Spectroscopy (TLAS). The parameters obtained with these techniques will help to improve the model of the gas attenuator by providing a further way of comparing the simulated and the actual gas properties.

The OES is a technique based on the measurement and analysis of the light emitted by the plasma, usually from the transition between some electronic, rotational or vibrational

levels of an atom or molecule population. Depending on the transition studied, different information can be obtained, like electron or gas temperature, electron density or heavy species concentration [13, 14]. In our case we will measure the spatial distribution of the plasma as in [15], which requires a relatively simple setup with only a collimator needed and no fine alignment requirements. In addition, it allows the simultaneous measurement of a broad spectrum (200 to 1000 nm), helping to identify the possibility of using other techniques in the future, like the measurement of the rovibrational lines of N_2 impurities to determine the gas temperature.

The TLAS is a technique based on the absorption of a laser beam by the plasma, generally by an excited state of an atom or molecule. The wavelength of a laser with a narrow bandwidth ($\sim$1 MHz) is scanned within a range of a few GHz while the transmitted signal is recorded by a photodiode. From the absorption profile one can obtain the excited states density and the temperature of the gas. This method is common in the study of a variety of plasma sources, like surfatron launchers [16, 17], distributed microwave plasma reactors [18], inductively coupled plasmas (ICP) [19, 20] or dielectric barrier discharges (DBD) [21]. In our case, we are interested in measuring the radial distribution of the exited states of the gas and its temperature; assuming thermal equilibrium, the temperature of the particles will be equal to that of the excited states.

A number of electronic transitions and levels are discussed during the chapter, related to the OES and TLAS measurements. The levels will be expressed either describing the electronic structure or using Paschen notation. For instance, the argon Ar(4s) and Ar(4p) level blocks are represented in Paschen notation as the 1s and 2p level blocks respectively.

Two different gas attenuators were used in two experimental campaigns. The first attenuator, used for the OES measurements, had a gas chamber with a total length of 1.46 m divided in two segments. The first segment was a 6-way cross of 18 mm diameter and 12.6 cm length, attached to the second segment consisting on a 1-m long cylinder of 12 mm diameter and a water-cooled double wall [9]. The second attenuator, used for the TLAS measurements, had a total length of 50.8 cm, with the gas chamber consisting

in two 6-way crosses of 18 mm diameter and 12.6 cm length separated by a cylinder of the same length and diameter. Both gas chambers were isolated from the vacuum of the beamline by two beryllium foils (0.5 mm thickness) placed inside a water-cooled copper frame. The gas pressure was recorded in both cases with a MKS 920B piezoelectric gauge, with a range between 0.1 and 1000 torr.

The X-ray source used in both campaigns was a single U18 in-vacuum undulator at ID06, with a gap between 6 and 10 mm and a beam size variable between 1x1 and 4x4 mm defined by the aperture of the primary slits. The resulting photon flux spectra calculated with the SRW software [22] is shown in figure 2.1 for the 2x2 mm aperture and different gap values; when reducing the aperture the spectra has a similar shape but with narrower peaks. The total power carried by the white beam ranges from about 100 W to 800 W as indicated in table 2.1.

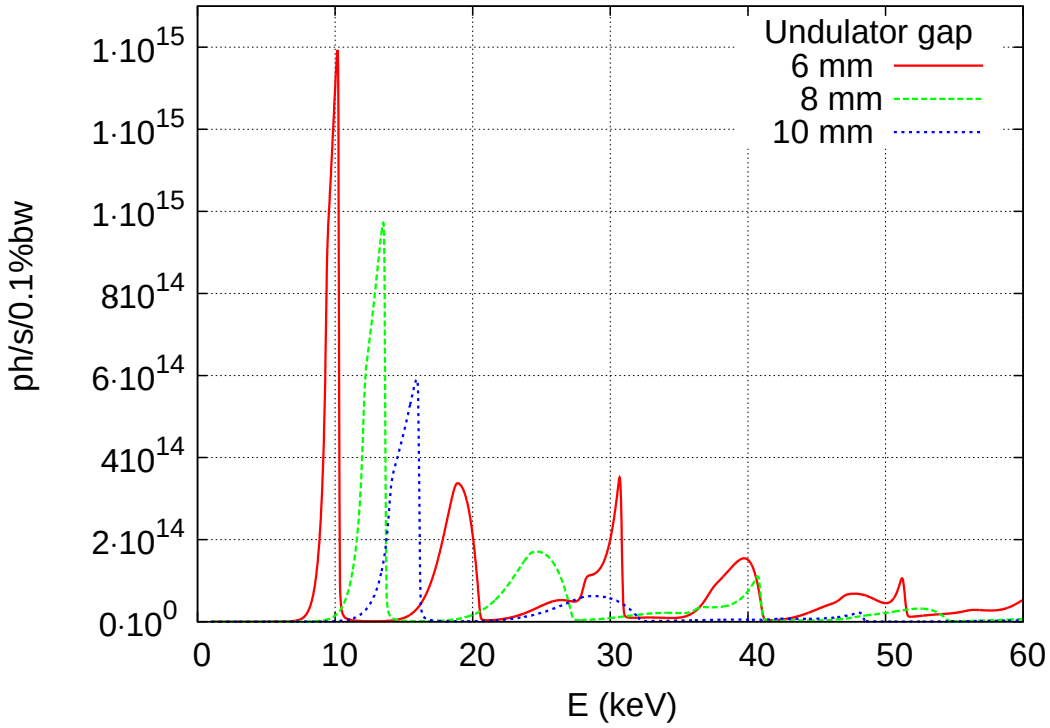

Figure 2.1: X-ray spectra of the U18 undulator calculated with SRW [22] for 200 mA in the storage ring and 2x2 mm beam size for several gaps.

Power (W)			
gap (mm) / K-value / size (mm^2)	6 1.317	8 0.902	10 0.217
1x1	238	152	91
2x2	770	482	278

Table 2.1: Measured total power of the white beam from U18 undulator and 200 mA, for different gaps and beam sizes. The K-value (eq. 1.3) changes with the undulator gap.

2.1 X-ray and power absorption

Two different ways of measuring the X-ray transmission and the power absorption were used during the experiments with the gas attenuator. The first method measured the total power of the X-ray beam before and after the attenuator with calorimeters, providing the total input power of the X-ray beam and the fraction absorbed by the gas. The second method measured the transmission at a chosen energy component of the white beam, usually the one at the first harmonic. The ratio between the transmitted intensities with and without gas allows the calculation of the average gas density without making any assumptions on the white beam spectrum.

The setup of the power absorption measurements is shown in figure 2.2, together with a schematic representation of the gas attenuator. The two calorimeters are placed up- and downstream from the gas attenuator to measure the incoming and transmitted power independently; in the absence of gas, both measured values should differ only in the power absorbed by the attenuator windows. The absorption by the windows will depend on the X-ray spectrum and on the window properties [23]; in our case it is negligible due to the high energy of the X-ray mean and the low Z and small thickness of the window material (0.5 mm of beryllium). Further downstream, a Double Crystal Monochromator (DCM) monochromatizes the beam to the selected energy. The intensity of the selected energy is measured with a beam intensity monitor, consisting on a thin foil of material intercepting the beam and a photodiode detecting the fluorescent and backscattered X-ray signal. The detected signal is proportional to the fluorescent and backscattered photons due to the constant solid angle; in turn, these emitted photons are proportional to the absorbed photons, with the fluorescence yield and the intensity-independent photon cross sections

as proportionality constants. Note that after the monochromator the number of photons is greatly reduced and we are far from saturation.

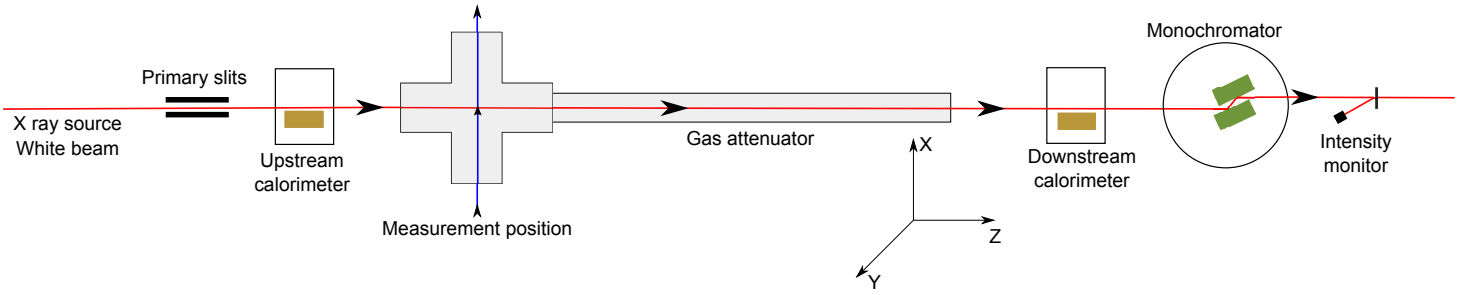

Figure 2.2: Setup of the beamline for the optical and power absorption measurements.

Calorimeter

The calorimeter consisted in a copper block of 2.17 kg which can be lifted onto the beam path, blocking the beam and absorbing all its power, or lowered out of the beam path to perform other measurements on the beamline (figure 2.3). The X-ray beam hits the calorimeter at the end of a hole of 12 mm diameter so that most of the fluorescent and backscattered photons are also absorbed. When the calorimeter is lifted, it is holded by three plastic screws on the sides, so that there is virtually no cooling through the holding system. To perform the measurement, the calorimeter is first lifted to the measurement position. When the temperature is uniform through the copper block, the front end is open and the beam heats up the calorimeter. After a time determined by the user, the front end is closed; a few seconds later the calorimeter reaches equilibrium and its temperature becomes constant. From the time the front end has been open (Δt in seconds) and the temperature difference between the initial and final states (T_1 and T_2 in K) the power of the beam can be calculated as

$$P = E/\Delta t = \frac{m}{\Delta t}\int_{T1}^{T2} C_p(T)dT \tag{2.2}$$

where m is the mass of the block in mol and $C_p(T)$ is the heat capacity of copper in J/mol/K. The expression for $C_p(T)$ is [24]:

$$C_p(T) = a + 2bx + 3cx^2 + 4dx^3 + 5ex^4 \quad \text{where } x = T(K)/280 - 1 \tag{2.3}$$

a	24.1693
b	2.06695
c	-0.636411
d	-3.54644
e	5.72283

Table 2.2: Coefficients of the copper heat capacity on equation 2.3.

The value of the coefficients are shown in table 2.2. The measured power are the incident (P_{in}) and the transmitted (P_{trans}) ones; the absorbed power is defined as the difference between them: $P_{abs} = P_{in} - P_{trans}$.

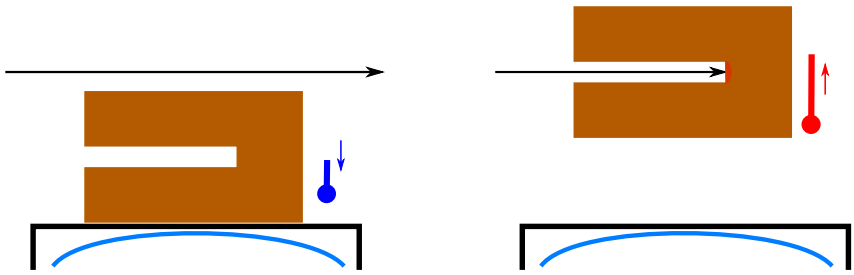

Figure 2.3: Scheme of the working of the calorimeter. Before the measurement (left), the calorimeter rests on a water cooled plate, letting the beam pass to the next beamline element. During the measurement (right), the X-ray beam is absorbed at the end of the hole, absorbing also backscattered photons; the temperature rise stops when the beam is turned off.

The temperature of the calorimeter is scanned at a constant frequency during the measurement, as shown in figure 2.4. The initial and final temperatures are taken as the average of the temperatures before and after the exposure to the X-ray beam. The decrease of temperature after the beam is turned off is due to the heat transfer within the copper block. To increase the resolution on the start time, it is calculated as the crossing of the initial temperature level with a linear regression including the first 4 to 5 points of the calorimeter scan. As for the end time, it is taken as the point in which the derivative of the temperature scan falls below the value that it maintains during the scan, which is

approximately constant. These methods proved useful to reduce the dispersion of several measurements taken with the same X-ray beam properties.

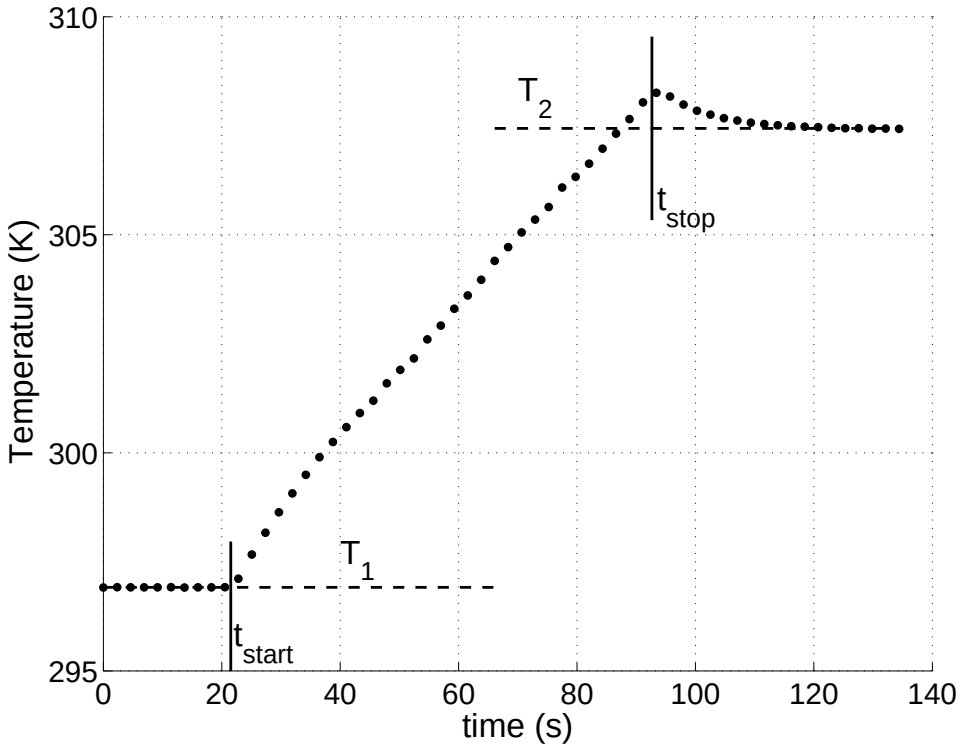

Figure 2.4: Sample of a calorimeter acquisition and corresponding data treatment. The number of points used for the initial and final average temperatures and for the linear regression of the leading edge are set manually for each measurement.

Double crystal monochromator (DCM)

The DCM and intensity monitor measured the X-rays transmitted through the attenuator at a selected energy, with an energy bandwidth which in the case of the ID06 monochromator is of $\frac{\Delta E}{E} \approx 10^{-4}$. The transmission of the DCM, given a flat surface of both crystals, is independent of the incoming intensity of the X-ray beam. However, the absorption of the X-ray beam by the first crystal heats up and deformates the surface, creating a bump that deflects the beam at different angles instead of at a single one [6, 7]. To take this effect into account, we need to measure the intensity at several angles, so that all the monochromatic intensity emitted at different directions is measured. This is done by scanning the transmission as a function of the angle of the second crystal; the result is the

rocking curve of the first crystal (figure 2.5) whose integral is proportional to the X-ray beam intensity and independent of the deformations on the first crystal.

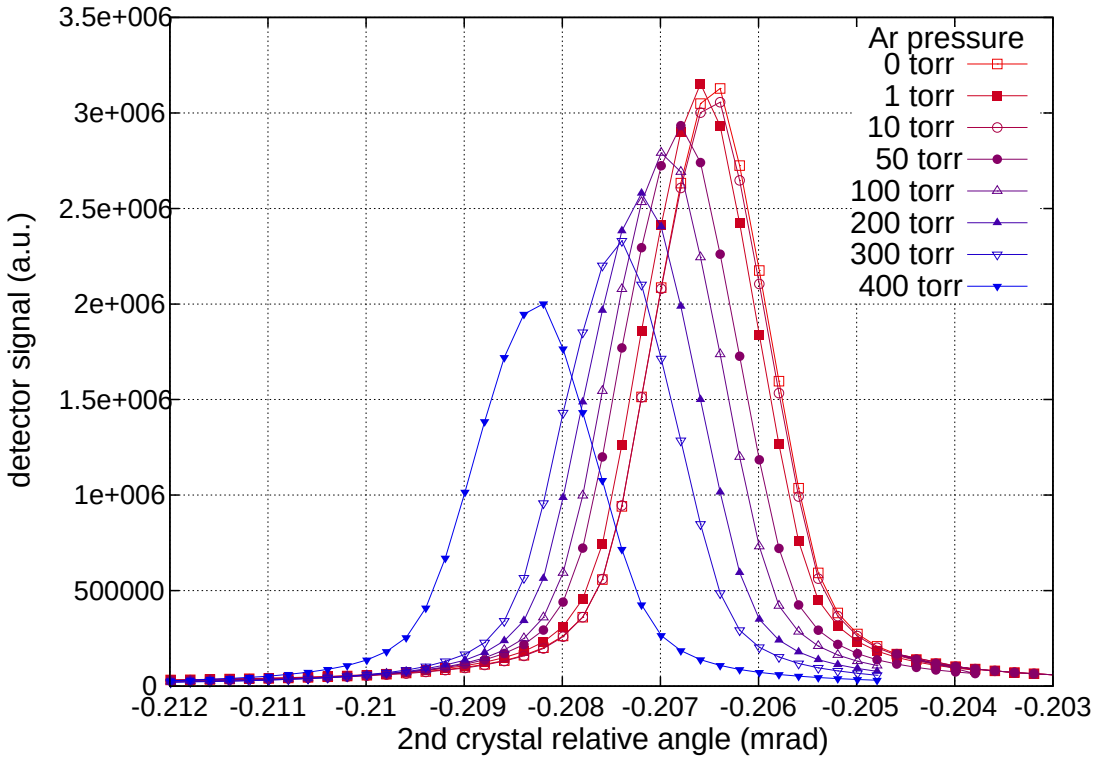

Figure 2.5: Rocking curve of the DCM first crystal for 6 mm gap of the undulator at 19.75 keV and different argon pressures.

Measured this way, the signal given by the intensity monitor is proportional to the photon flux, so that the ratio of the signals with and without gas in the attenuator is proportional to that of the X-ray intensity:

$$\frac{I(E)}{I_0(E)} = e^{-\sigma(E)\rho\Delta z} = e^{-\mu(E)\Delta z} \tag{2.4}$$

where $\sigma(E)$ is the gas cross section at the selected energy in cm^2/g taken from the NIST XCOM database [25], ρ is the gas density in g/cm^3, Δz is the length of the attenuator in cm and $I(E)$ and $I_0(E)$ are the measured intensities at the given energy with and without gas in the attenuator respectively. $\mu(E) = \sigma(E)\rho$ is the mass absorption coefficient in cm^{-1}. From this ratio the average gas density along the beam path can be calculated as

$$\rho = \frac{1}{\sigma(E)\Delta z} \log\left(\frac{I(z,E)}{I_0(E)}\right) \tag{2.5}$$

Once the gas density is know, the intensity absorbed by the gas for all the energies can be calculated, taken as the intensity not transmitted:

$$I_{abs}(E) = I_0(E) - I(E) = I_0(E) - I_0(E)e^{-\sigma(E)\rho\Delta z} = I_0(E)\left(1 - e^{-\sigma(E)\rho\Delta z}\right) \tag{2.6}$$

Integrating the number of absorbed photons in all the energies we obtain the total absorbed power:

$$P_{abs} = \int_E N_{abs}(E) \cdot E \cdot dE \tag{2.7}$$

where $N_{abs}(E)$ is the number of photons. However, the X-ray intensity $I_0(E)$ is usually given in photons/s/0.1% bandwidth, so in practical units the power absorbed is written as

$$P_{abs} = \int_E I_0(E)\left[1 - e^{-\sigma(E)\rho\Delta z}\right] \cdot 1.602 \cdot 10^{-16} \cdot dE \tag{2.8}$$

where P_{abs} is in watts. Note that this formula can also be used to obtain the gas density from the power absorbed measured by the calorimeters, given a know X-ray spectrum: the only free parameter is the gas density.

Also from the average gas density we can use the ideal gas law to obtain a gas temperature. This is not exactly the average gas temperature because the relation between gas density and temperature is inversely proportional; the average gas density is proportional to the average of the *inverse* of the temperature:

$$< \rho > = < \frac{p \cdot MW}{RT} > = Cte \cdot < \frac{1}{T} > \approx Cte \cdot \frac{1}{< T >} \tag{2.9}$$

where MW is the molecular weight of the gas, R is the ideal gas constant and p is the measured gas pressure. Still, this temperature will give us an approximate idea of the temperature of the gas along the x-ray beam path.

Power absorption results

Both calorimetric and DCM measurements were used in the two experimental campaigns carried on the gas attenuator. The calorimetric measurements were used not only to obtain the power absorption and gas density of the attenuator, but also to validate the white beam total power as simulated by SRW. In the cases where there was a disagreement between experimental and simulated power, the corresponding simulated spectrum was rescaled as to have the same power as the experimental one. The DCM measurements were used to obtain directly the gas density, and from it and the rescaled simulated spectrum, the absorbed power. The agreement between the two methods was within 10% in the worst case.

The results of the power absorption, calculated from the X-ray transmission measurements (eqs. 2.5 and 2.8), are shown in figures 2.6a and 2.6b), plotted versus the gas pressure. The data from the two experimental campaigns are shown separately to simplify their interpretation. Figure 2.6a shows the results for the first experimental campaign, in which both argon and krypton were used, and where the attenuator length was 1.46 m. Figure 2.6b shows the results for the second campaign, using only argon and where the attenuator length was 0.5 m. The difference on length explains the difference on the scale of the absorbed power: the longer attenuator absorbs more than the shorter one. Apart from this, the first observation that can be done is the general increase of the absorption with the gas pressure, for each given set of X-ray beam properties (spectrum, size and power). This is something expected, since an increase in pressure means an increase in density and, according to the Beer-Lambert law, in the X-ray absorption. Also, in figure 2.6a we can see that krypton absorbs more than argon, also expected because of its higher X-ray cross section. The change in the trend observed for krypton at 550 mbar and 770 W of (nominal) input power is due to the variations on the actual input power. The input power may be reduced down to a 80% of the nominal one because of the decrease in the synchrotron current, which is refilled periodically. To account for the effect of the changes of the input power, the *fraction* of the absorbed power is shown in figures 2.6c and 2.6d for the first and second experimental campaigns respectively. The fraction of the absorbed power increases with the gas pressure, without exceptions. Another observation is that

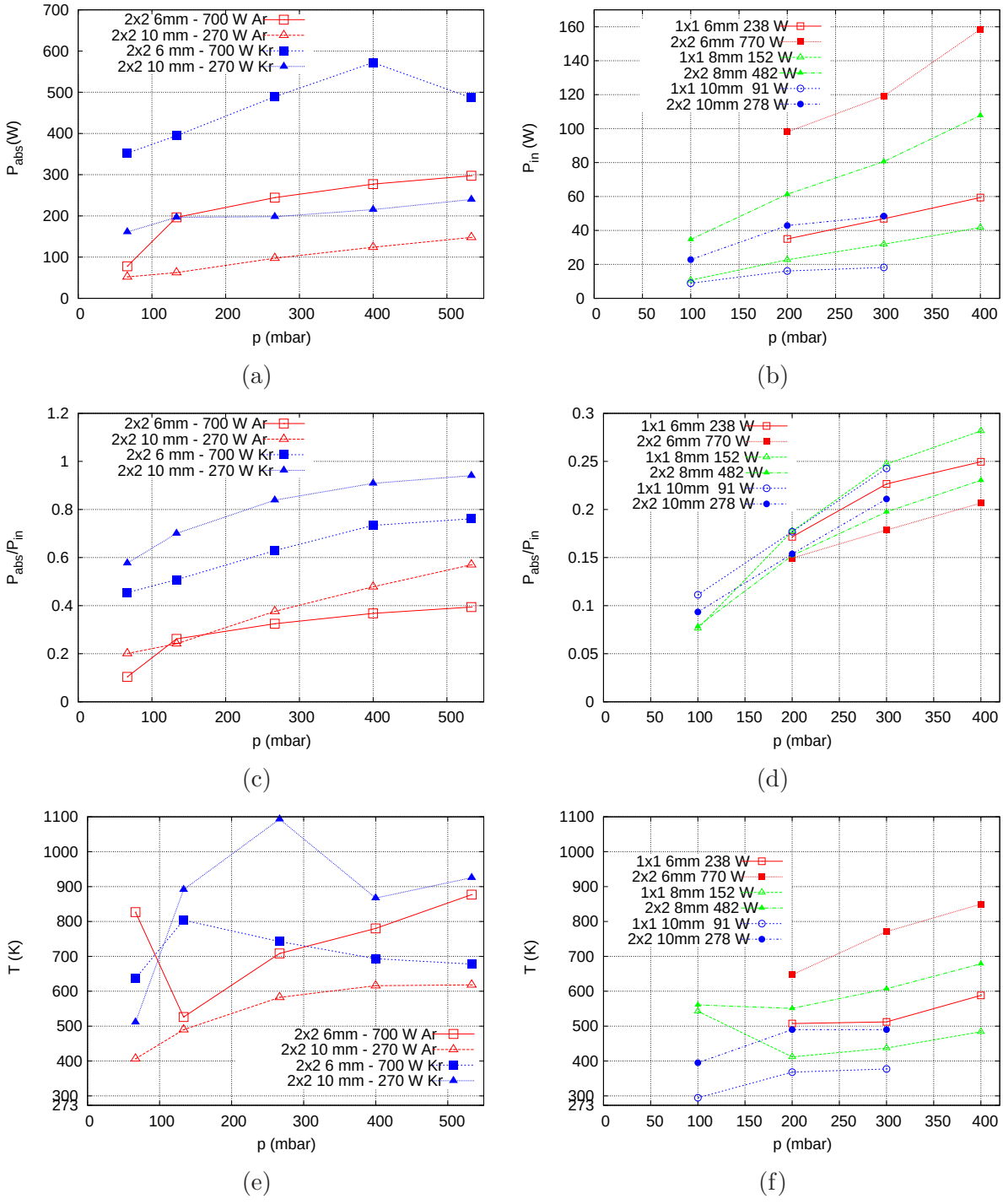

Figure 2.6: Results obtained from the X-ray absorption measurements: total absorbed power (6a and 6b), fraction of absorbed power (6c and 6d) and average gas temperature (6e and 6f). The results for each experimental campaign are shown separately: the 6a, 6c and 6e figures correspond to the OES setup (1.46 m length) where argon and krypton were used, and the 6b, 6d and 6f figures correspond to the TLAS setup (0.58 m length) where only argon was used. The key on each plot indicates the X-ray beam size, undulator gap (related to the spectrum), nominal power and, in plots 6a, 6c and 6e, gas used.

the absorbed fraction is higher for lower input power, although the total absorbed power is still lower. The reason is that, as the input power increases, so it does the heating of the gas. This results in an increase in temperature and a decrease in density and absorption ratio.

The corresponding temperatures (figures 2.6e and 2.6f), calculated from equation 2.9, do not follow a clear trend, having cases where the temperature increases with the pressure and cases where it decreases. There are two possible reason for this behaviour. First, as we increase the pressure, both the heating and the cooling increase, and the balance between them is complex enough to not follow a constant trend. For example, an increase in pressure could increase the heat transfer by convection. Second, the temperatures obtained are not a local value but an average one, and therefore do not tell anything about the local values or the axial temperature profile along the beam path, which could impact the average temperature in different ways. Because of the shorter length of the attenuator of the second campaign (figure 2.6f), the temperatures obtained in that case should be more representative of the temperature than those of the first campaign (figure 2.6e).

The comparison (made in chapter 5) of these results with the theoretical model described in chapters 3 and 4 will be the main indicator on whether the model includes all the processes involved in the X-ray absorption and energy dissipation and, more important, whether it can be applied to the prediction of power absorption for existing and future attenuators.

2.2 Optical Emission Spectroscopy (OES)

The objective of the OES measurements is to determine the size of the region with a high concentration of excited species. These species may be created either by direct excitation from the ground state by fast electrons or by recombination of diatomic ions resulting in the emission of a neutral, excited atom. Therefore, the measurement of the region with excited species becomes a measurement of the fast electrons range and of the diffusion of

ions and neutral heavy species. In this case, we study the transitions between the 2p and 1s levels of both argon and krypton, between 500 and 1000 nm of wavelength (figures 2.7 a and b). Except for the lines coming from N_2 impurities in the argon spectra, between 300 and 400 nm, the 2p-1s lines are the only ones appearing in the measured spectral range.

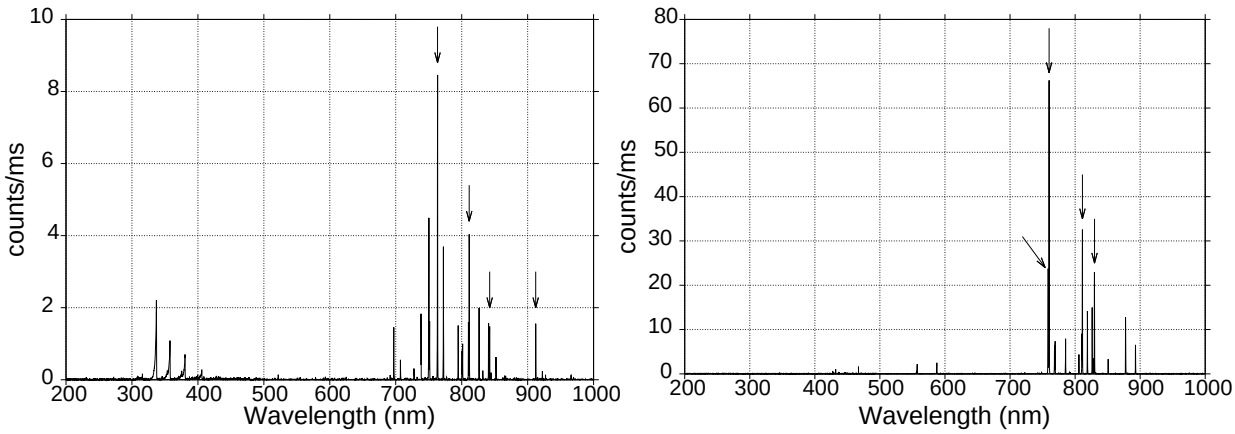

(a) (b)

Figure 2.7: Complete OES spectra from argon (a) and krypton (b). The arrows indicate the lines used in the OES scans, specified in table 2.3.

To perform the OES measurement, two flanges of the gas chamber were fit with fused silica windows, with a transmission higher than 95% in the 200-1000 nm spectral range. The light emitted by the plasma was collected by a 0.5 mm collimator an directed to an optical fiber, in turn connected to an Avantes AVS-MC2000 spectrometer (figure 2.8). The range of the spectrometer goes from 200 to 1000 nm (figure 2.7), with a resolution of $\sim$0.15 nm. The collimator and fiber assembly were connected to a motorized table, allowing for spatial scans on the vertical (for horizontal line-of-sight) or horizontal (for vertical line-of-sight) directions.

The light emitted by the plasma on a particular emission line is given by the spontaneous emission equation

$$\epsilon = \frac{1}{4\pi} n_2 A_{21} \tag{2.10}$$

where A_{21} is the Einstein coefficient between the upper and lower levels, n_2 is the upper state density and ϵ is the emission coefficient in photons per unit of time, volume and steradian. According to the equation 2.10, the spatial variations in the emission coefficient

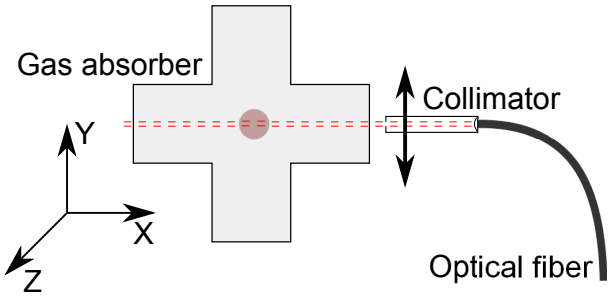

Figure 2.8: Schematic view of the optical setup for the OES measurements. The collimated line of sight is focused on the entry aperture of an optical fiber, the other end being connected to the spectrometer. The collimator is mounted on a movable table so that it is possible to scan the signal at different Y positions. The X-ray beam crosses the attenuator in the Z direction.

are proportional to the upper state density variations. However, the signal measured by the spectrometer is not the local emissivity but its projection integrated along the line of sight of the collimator and fiber:

$$I(y) = \int_L \epsilon(x, y) dx \tag{2.11}$$

where L is the length of the line of sight. Assuming azimuthal symmetry of the emissivity $\epsilon(x, y) = \epsilon(\sqrt{x^2 + y^2}) = \epsilon(r)$, its relation with the projected intensity can be expressed via the Abel transform

$$I(y) = 2 \int_y^R \epsilon(r) \frac{r}{\sqrt{r^2 - y^2}} dr \tag{2.12}$$

which can be inverted analytically

$$\epsilon(r) = -\frac{1}{\pi} \int_y^R \frac{dI(y)}{dr} \frac{1}{\sqrt{y^2 - r^2}} dy \tag{2.13}$$

A number of methods exist to solve this inversion problem numerically [26, 27] to obtain the radial profile. The lines used in this work belong all to the 2p-1s transitions (table 2.3) for both argon and krypton, which were found to have sufficient intensity in all the experimental cases. The lines were chosen arbitrarily among the most intense ones.

To verify whether the optical system can capture variations on the active plasma region size, a set of three scans with asymmetric beam profiles (4x1, 2x2 and 1x4 mm) were recorded with krypton gas at 400 mbar. For each scan, the four lines shown in table 2.3

Ar		Kr	
Wavelength (nm)	transition	Wavelength (nm)	transition
763.38	2p6→1s5	758.60	2p5→1s4
811.40	2p9→1s5	760.09	2p6→1s5
842.46	2p8→1s4	811.24	2p9→1s5
912.23	2p10→1s5	829.81	2p7→1s4

Table 2.3: Transitions of each gas used to perform the spatial scans using OES.

were recorded simultaneously. The results are shown in figure 2.9, in which we can appreciate that the four lines recorded yield the same spatial profile for the same beam size, and that this profile becomes narrower when we reduce the beam size in the perpendicular direction to the line of sight. This not only demonstrates the good spatial resolution of the setup but also that the active plasma region is effectively confined around the X-ray beam.

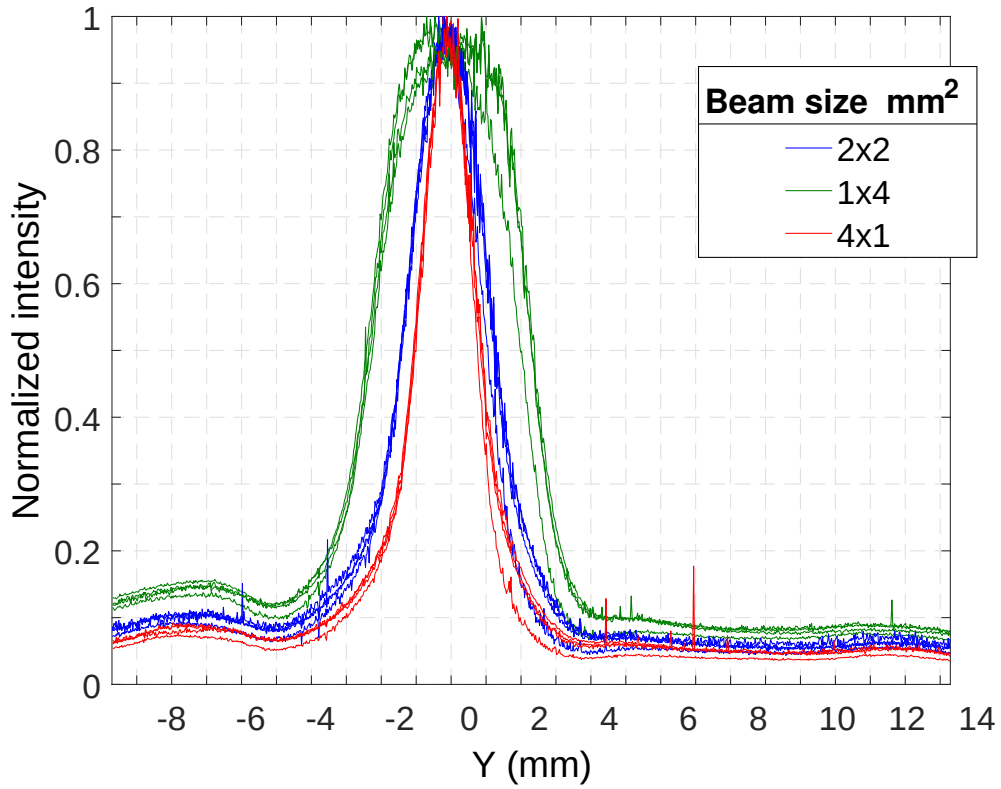

Figure 2.9: Scan of the OES signal along the vertical direction, for 400 mbar Ar and an X-ray beam of 6 mm gap in the undulator and a variable beam size (shown in the legend). The channel intensities have been normalized to its maximum value to simplify the comparison.

The next step is to study the azimuthal symmetry of the plasma region. To this end, two scans, one horizontal and one vertical, were taken using a square-shaped beam of 2x2

mm and a gas pressure of 400 mbar argon, with a gap in the undulator of 10 mm (∼270 W input power). These scans are shown in figure 2.10, together with their respective Abel transforms. Both scans have a similar profile around the center, with more intense wings in the horizontal than in the vertical one. However, this difference might be the effect of a difference in the stray light, due to a difference in the cross section of the attenuator. In the horizontal scan, it was a cylinder of 12 mm radius with a flange only in the vertical side, while in the vertical scan it was a 18 mm radius 6-way cross section with flanges in both sides. The difference in the stray light will be less important around the center, where the light comes mainly from the plasma itself and where both scans and their respective Abel transforms coincide. Therefore, we can conclude that the plasma shows a similar profile in the horizontal and vertical directions. While this alone is not enough to demonstrate the azimuthal symmetry (and the validity of the Abel transform), it can be justified by the diffusion of electrons and other particles. Although the diffusion is small enough to keep the plasma confined around the X-ray beam, even a small amount could smooth the corners of a square-shaped beam, making the approximation of azimuthal symmetry reasonable. In addition, the results of the Abel transform will be used to study only the overall size of the plasma region, not the details of its distribution.

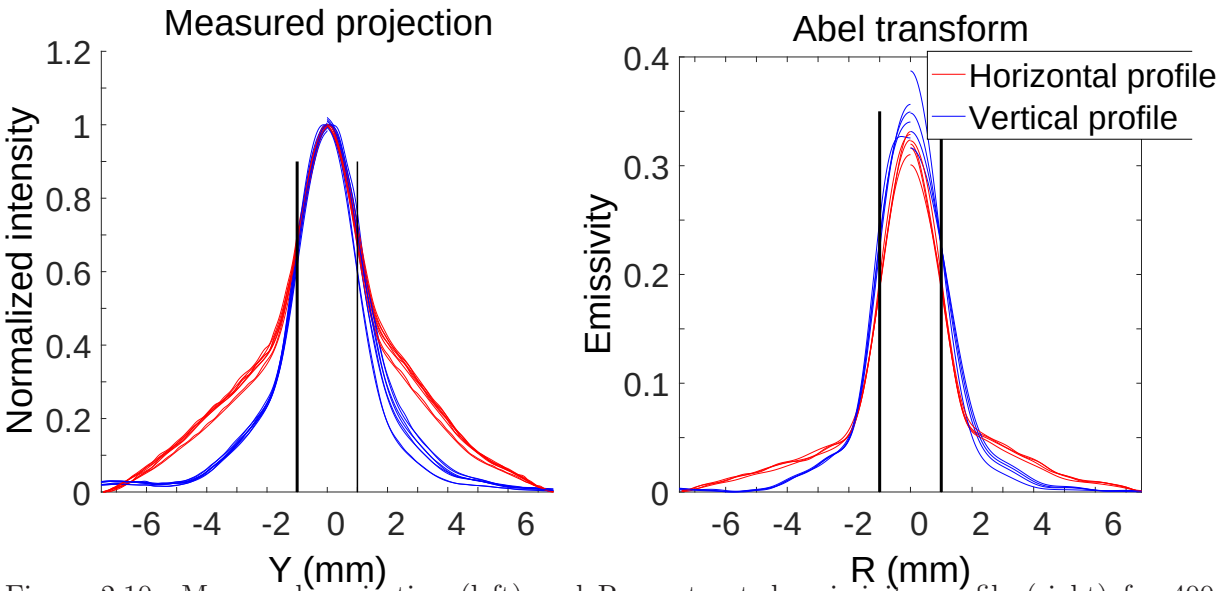

Figure 2.10: Measured projection (left) and Reconstructed emissivity profile (right) for 400 mbar argon, undulator gap of 10 mm and beam size of 2x2 mm. the signal of the 4 different channels has been normalized to the same maximum value. Note that in the region of the highest intensity, both horizontal and vertical profiles match.

Once the hypothesis of good enough spatial resolution and azimuthal symmetry have been verified, we can compare the size of the plasma region for different gas, chamber pressure and beam properties. The results for the full width at half maximum (FWHM) of the recorded profile and the reconstructed emissivity are shown in figure 2.11. In all the cases the X-ray beam was square-shaped. For every X- ray beam and attenuator configuration, the change in the gas pressure did not changed significantly the FWHM of the active plasma region, remaining fairly constant within all the operation conditions (50-550 mbar). This means that even at the lowest pressure, the thermalization distance of the fast electron (distance traveled between their emission point and the point where their energy becomes thermal) is much smaller than the size of the beam, so that the active region in which the electrons slow down and excite the gas atoms is determined by the beam size.

If we compare the different cases among them we observe that the power of the X-ray beam does not affect much the size of the active region: for argon, the two measurement series were made with the same beam size and different gaps (therefore power), resulting in almost identical active region sizes. Only when changing the beam size, as was made in the two series with krypton, the size of the active region changes. As for the difference between different gases, when using krypton the active region is smaller than for argon, for the same gas pressure and beam size. The reason is that krypton has a larger electron-impact cross section ($\sim$1.5 times that of argon for ionization and excitation collisions), resulting in a more effective slow-down of electrons and a decrease of the region where the ions and excited species are produced.

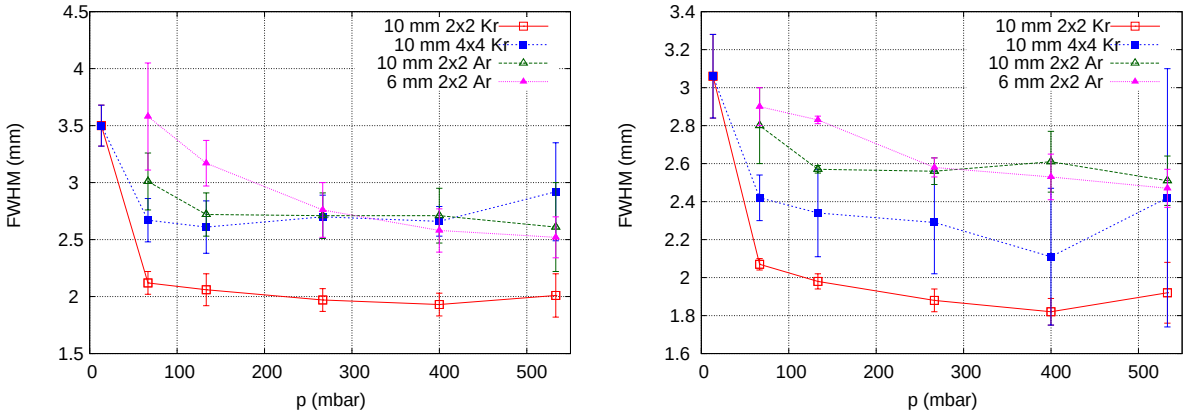

Figure 2.11: FWHM of the projected profile (a) and the reconstructed emissivity (b) as a function of the pressure for different gases and beam parameters. The plotted value is the average of the FWHM from each of the four channels used.

2.3 Tunable Laser Absorption Spectroscopy (TLAS)

The objective of the TLAS measurements is to obtain the metastable density of the $1s_5$ level of argon and the local gas temperature from the absorption profile. The laser used for this kind of experiments usually has a wavelength centered around a transition in the optical range, a bandwidth of a few MHz (relative bandwidth of around 10^{-8}) and a scanning range of a few GHz. Thus, the shape of the transition can be recorded without a spectrometer, just measuring the transmission of the laser through the plasma with a photodiode. In the same experimental campaign the first images of the operation of the gas attenuator were taken (figure 2.12).

The laser set-up of the TLAS measurements (figure 2.13) consisted on a diode laser (DFB, Toptica, Littrow configuration) tuned to the 772.38 nm ($3.88 \cdot 10^5$ GHz) transition of Ar, with a hop-free mode scanning range of 20 GHz and a wavelength bandwidth of 5 MHz. The selected wavelength corresponds to the $1s_5 \rightarrow 2p_7$ transition of argon. The laser beam is split in three branches directed to a reference cell, to a Fabry-Perot interferometer and to the gas attenuator chamber. The reference cell consist on a low pressure (∼1 mbar) glow discharge and it is used to set the laser wavelength before the measurements. The Fabry-Perot interferometer has a free spectral range (FSR) of 0.375 GHz and is used to calibrate the frequency shift of the laser. The beam directed to the

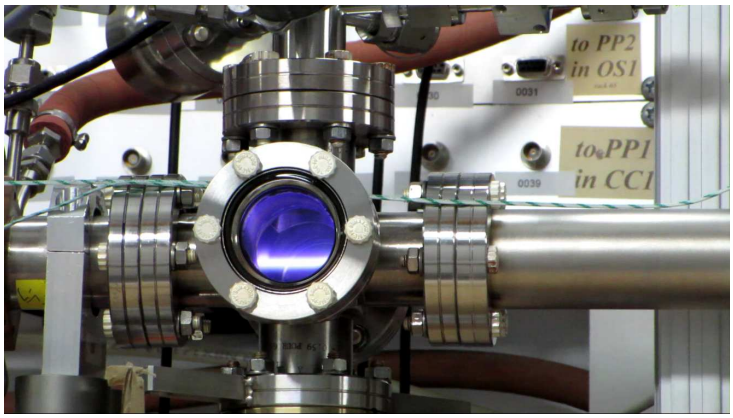

Figure 2.12: Composed imaged of the plasma inside the gas attenuator and the chamber and window containing the gas. The well-defined emitting light region illustrates the confinement of the plasma around the X-ray beam path.

attenuator is reflected on a mirror mounted on a motorized support and can scan the attenuator in perpendicular to the X-ray beam, in the same way as the with the OES. A diaphragm reduces the laser beam size to 0.5 mm in diameter. All three branches are terminated with photodiodes whose signals are simultaneously collected by an oscilloscope and recorded digitally. To obtain the absorption signal, the background of the photodiodes I_{back} has to be subtracted from the transmission signal I_{off} (X-ray off, no plasma and no absorption), and the light emitted from the plasma I_{plasma} has to be subtracted from the absorption signal I_{on} (X-ray on, plasma and absorption). The shape of those four acquisitions is shown in figure 2.14. The absorption signal is calculated as

$$A(\nu) = log\left(\frac{I_{off}(\nu) - I_{back}}{I_{on}(\nu) - I_{plasma}}\right) \tag{2.14}$$

where $A(\nu)$ is the absorption signal as a function of the frequency ν.

The absorption of the laser beam is described by the Beer-Lambert equation

$$\frac{dI(\nu, x)}{dx} = -k(\nu, x)I(\nu, x) \tag{2.15}$$

where I is the laser intensity in ph/s/m^2, ν is the laser frequency, x is the position along the laser beam and k is the local absorption coefficient. For an electronic transition like

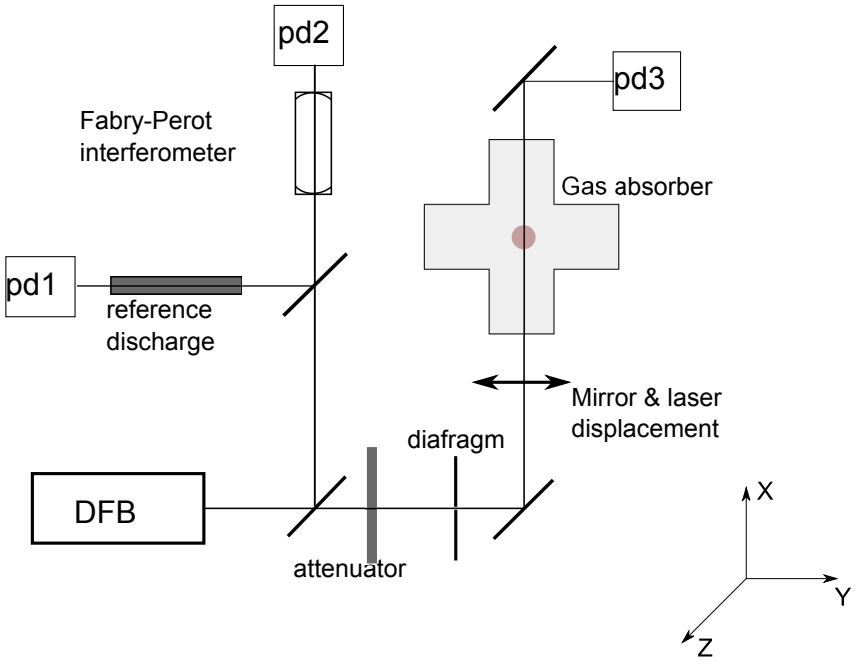

Figure 2.13: Scheme of the laser absorption setup. The laser beam position can be moved perpendicular to the X-ray beam, in the plane of the paper.

the measured here, k can be written as

$$k(\nu) = \left[\lambda^2/(8\pi)\right] \left[\eta_l - \eta_u\right] g_u A_{ul} \phi(\nu) \tag{2.16}$$

where A_{ul} is the Einstein coefficient of the transition, $\phi(\nu)$ is the line profile and $\eta_u = n_u/g_u$ and $\eta_l = n_l/g_l$ are the level density per number of states of the upper and lower states respectively (n the state density and g the degeneracy). The terms of η_u and η_l correspond to the stimulated emission and pure absorption respectively. In our plasma conditions η_l is expected to be much larger than η_u and therefore the stimulated emission can be neglected and the absorption coefficient simplified:

$$k(\nu) = \left(\lambda^2/8\pi\right) n_l(x) g_u/g_l A_{ul} \phi(\nu) \tag{2.17}$$

Since $n_l(x)$ is a function of the position, the measured absorption for each frequency and beam position is the integral along the line of sight

$$A(\nu, y) = log\left[I(\nu, 0, y)/I(\nu, L, y)\right] = \left(\lambda^2/8\pi\right) g_u/g_l A_{ul} \int_0^L n_l(x, y)\phi(\nu) dx \tag{2.18}$$

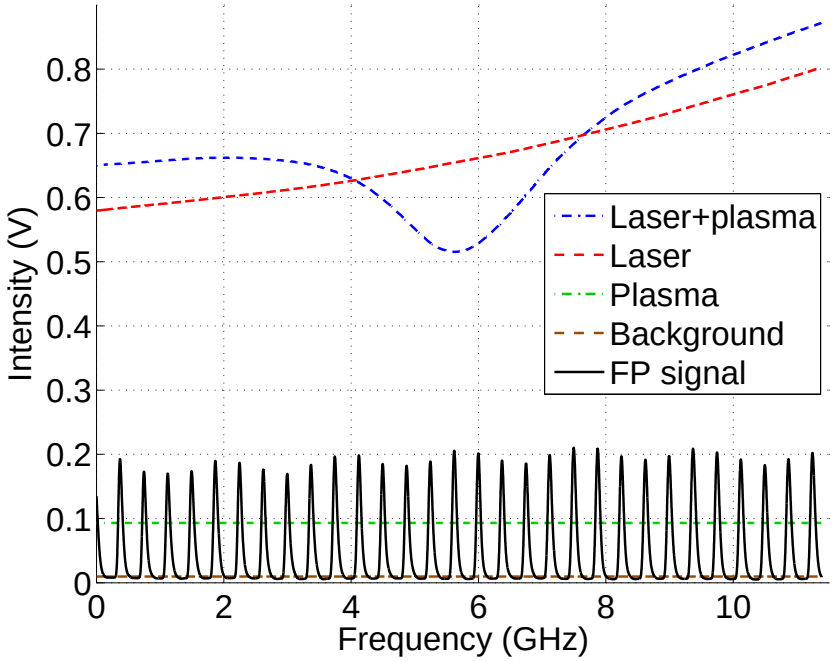

Figure 2.14: Measurement of the signals required to obtain the absorption profile: background, plasma signal (both with laser off), transmission (laser on, X-ray off) and absorption (laser on, X-ray on). The Fabry-Perot signal is recorded every time to calculate the frequency shift of every point of the curves.

where L is the length of the plasma at the measured position. The integral over the line shapes gives

$$S(y) = \int_{-\infty}^{\infty} A(\nu, y) d\nu = \left(\lambda^2/8\pi\right) g_u/g_l A_{ul} \int_{-\infty}^{\infty} \int_{0}^{L} n_l(x, y) \phi(\nu) dx d\nu \tag{2.19}$$

The line shape integral equals to one, giving a simplified expression

$$S(y) = \left(\lambda^2/8\pi\right) g_u/g_l A_{ul} \int_{0}^{L} n_l(x, y) dx = \frac{1}{C} \int_{0}^{L} n_l(x, y) dx \tag{2.20}$$

which relates the integral value over the line shape at each position with the projected metastable density along the line of sight, with the constant C depending on the specific transition ($1.36 \cdot 10^7$ s/m^2 for the studied $1s_5 \rightarrow 2p_7$ transition [16]). If, as in the OES case, one assumes that the metastable density $n_l(x, y)$ has azimuthal symmetry, it is possible to apply equations 2.12 and 2.13 to obtain its value as a function of the radial position $n_l(r)$.

The line shape of the absorption signal is determined by several broadening mechanisms: natural, Stark, Doppler and Van der Waals broadening. In our experimental conditions the expected total broadening will be higher than 1 GHz. Following refs. [28,29],the natural absorption broadening contributes with only around 6 MHz, so it can be neglected here. The Stark absorption has a Lorentzian profile with a FWHM given by:

$$\Delta\nu_S(FWHM) = 0.08 \cdot 10^{-16} N_e(Hz) \tag{2.21}$$

which can become important for electron densities higher than 10^{15} $1/\text{cm}^3$. The Doppler broadening, due to the thermal movement of the atoms, gives a Gaussian profile with a FWHM of

$$\Delta\nu_D(FWHM) = 7.6 \cdot 10^{-7} \nu (T_g/M)^{1/2}(Hz) \tag{2.22}$$

where T_g is in K and M is the atomic mass in a.m.u. This mechanism becomes dominant at low electron density and low pressure (< 10 mbar). The remaining contribution is the Van der Waals broadening due to collisions of thee metastables with other neutral atoms. It has a Lorentzian profile with a FWHM of

$$\Delta\nu_{VdW}(FWHM) = Kp(300/T_g)^{0.7}(Hz) \tag{2.23}$$

where the temperature is in Kelvin and the p is the pressure in mbar. K is a transition dependent constant, which for the measured transition has a value of $1.59 \cdot 10^7$ [16].

The absorption measurements were carried out, for every gas pressure and X-ray beam properties, at steps of 0.5 mm around the absorption maximum and with larger steps (1 and 2 mm) in the regions where the absorption signal became weaker. The transmission (laser on, X-ray off) and absorption (laser on, X-ray on) measurements were taken for every position, while the plasma and background signals are constant for all the points and were taken only once for every set of operating conditions. The absorption signal is then calculated using equation 2.14, and the fitted to a Voigt function using the Gaussian and Lorentzian components in formulas 2.22 and 2.23, with the gas temperature as the

free parameter. The measurements were performed for 100, 200, 300 and 400 mbar of argon gas, 6, 8, and 10 mm gap in the undulator and a beam size of 1x1 and 2x2 mm.

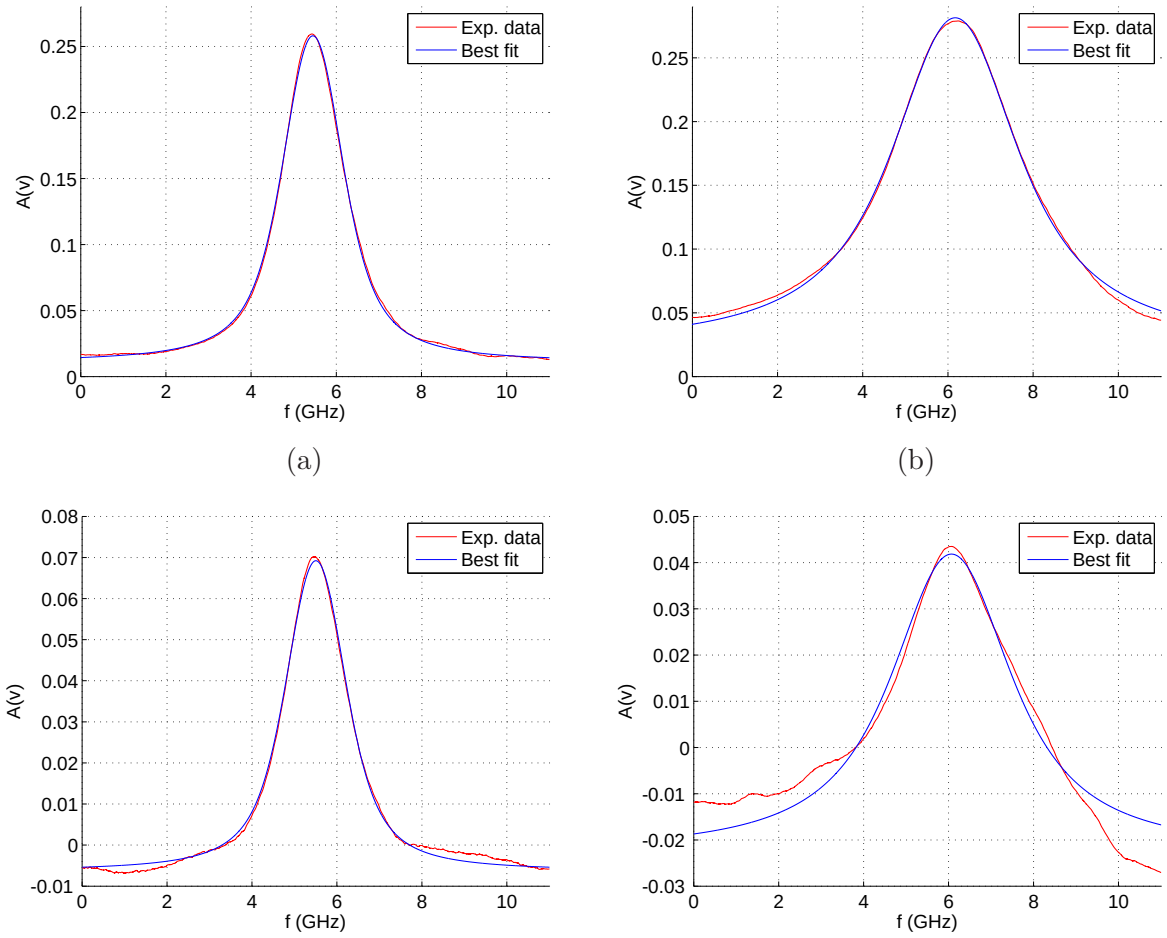

Figure 2.15: Absorption signal at center for 100 mbar (a) and 300 mbar (b) and at 4.5 mm from center at the same pressures (c and d), together with the best fit for each case. In all the cases the undulator gap was 6 mm and the beam size 2x2 mm.

Figure 2.15 shows the fits for 100 and 300 mbar of pressure at the center and at 4.5 mm from the center of the attenuator. The signal becomes much smaller at this distance from the center, so that the noise becomes more important and the quality of the fit decreases. This can also be noted in figure 2.16, where the metastable density obtained from equation 2.20 and the gas temperature obtained from the fit are shown. The metastable density is higher at the center and decreases monotonically towards the wall of the attenuator, as it could be expected. However, the temperature has nonphysical oscillations in the

region where the metastable density is low; this is due to a bad fit. The only meaningful temperature results are those obtained around the metastable density peak, where the fit quality is better and the relative noise lower. This means that while we can compare the complete metastable density profile obtained from the TLAS, only a central temperature can be obtained from it.

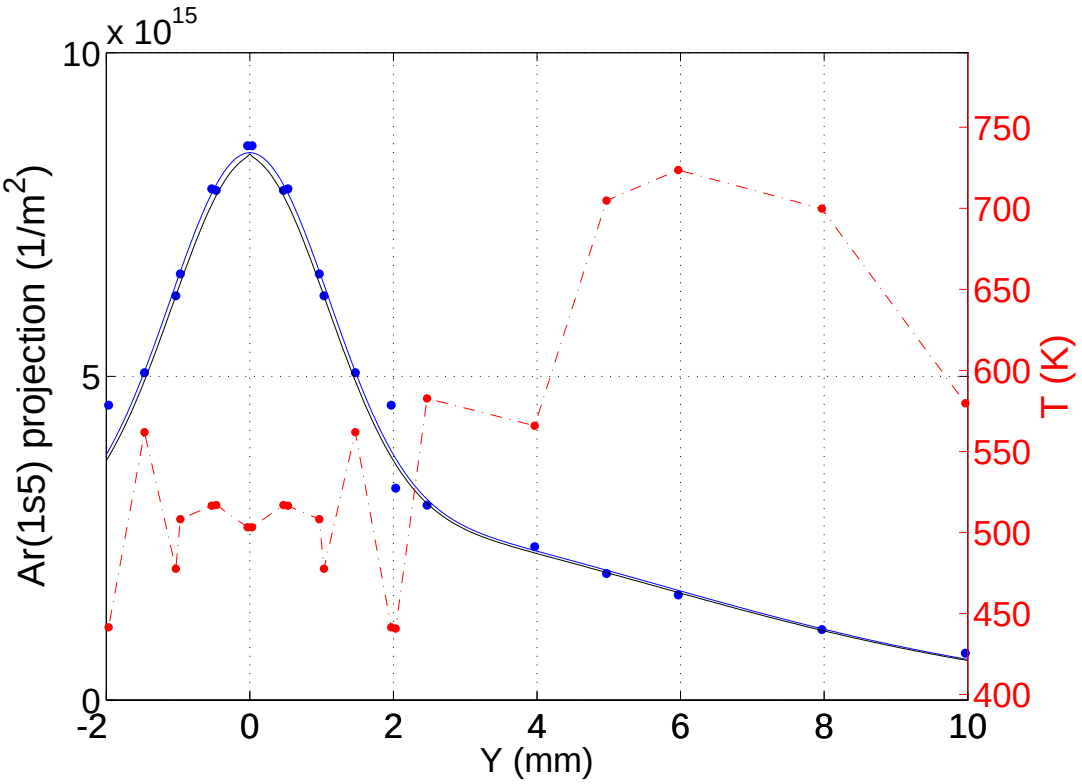

Figure 2.16: Metastable density projection and fit temperature of the absorption profile for the case of 100 mbar, 6 mm gap undulator and 2x2 mm X-ray beam size. The oscillations in the fit temperature are due to the small signal far from the center, resulting in large noise and a bad fit.

The central temperature is taken as the average of the five central points, and the error as the difference between the maximum and the minimum temperature within those points. The results calculated this way are shown in figure 2.17 together with the temperatures obtained from the X-ray absorption measurements. We can see that in general the TLAS temperatures are lower than those obtained from the X-ray absorption, which might be due to uncertainties in the Doppler and Van der Waals broadening coefficients or to an non-negligible Stark broadening. A contribution of the latter to the line broadening

would lead to a correspondent decrease of the fitted Van der Waals broadening, so that the total Lorentzian component remains constant, and an increase of the resulting gas temperature. However, to perform this procedure knowledge of the electron density and temperature is required.

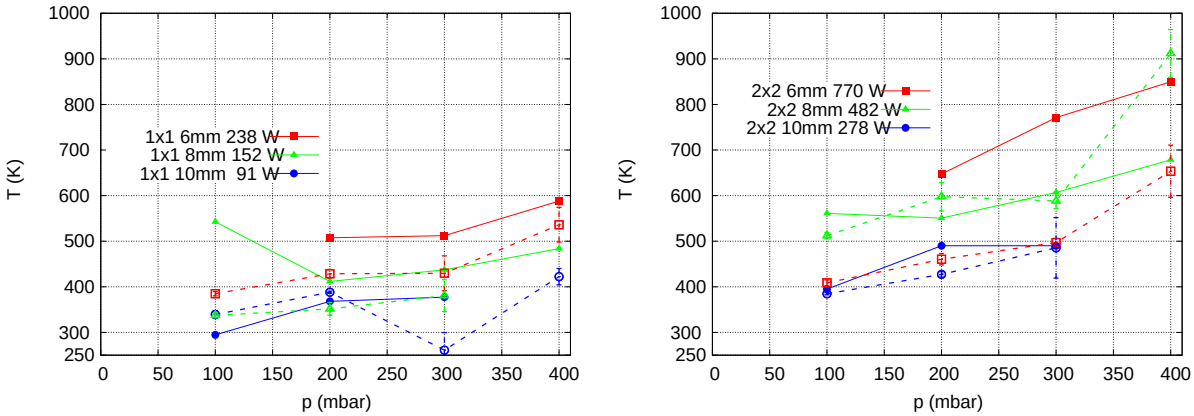

(a) (b)

Figure 2.17: Comparison of the temperatures obtained by X-ray transmission (fill lines) and by TLAS (dotted lines) with beam sized of 1x1 mm (a) and 2x2 mm (b); the separation has been made for clarity on the plots.

To obtain the radial profile of the metastable density, we need first to verify whether the system has enough spatial resolution. As in the OES measurements, we measure the absorption profile for two beam sizes, 1x1 and 2x2 mm for identical gas pressure (100 mbar) and undulator gap (6 mm). The results of the normalized measured projection and corresponding metastable density profile are shown in figure 2.18, in which the two beam sizes yield very different profiles. In comparison, the profiles obtained for the same beam properties and different gas pressure (figure 2.19) are almost identical within the X-ray beam region, with the higher pressure case showing a more sharp drop of the metastable density far from that region. A probable reason is that, as the particle density increases, the metastable mobility decreases and the quenching reactions ratio increases, with the result that the metastable atoms decay before diffusing far from the central region.

As in the OES case, the FWHM of the metastable density and projected profiles do not change significantly with pressure or beam power, but only with beam size (figure

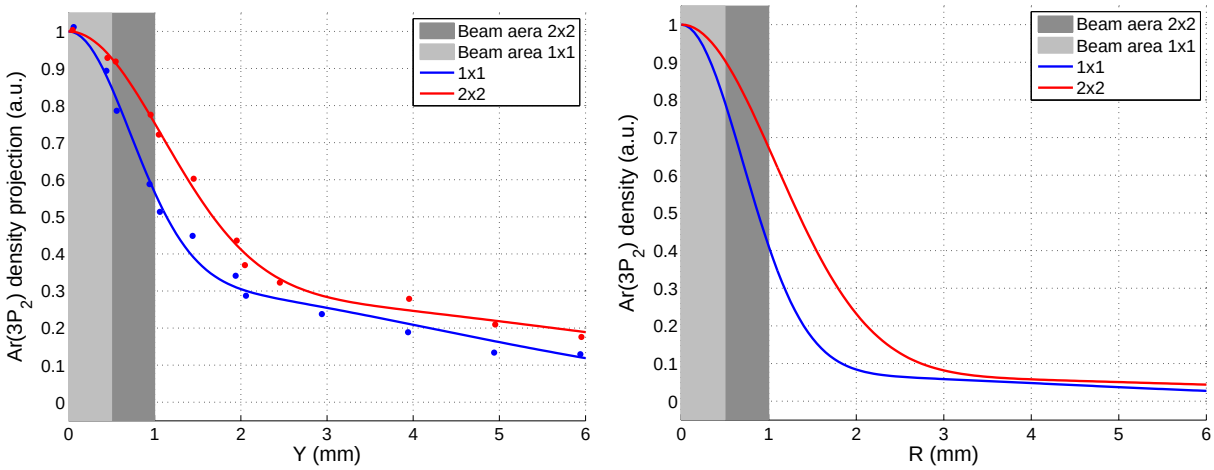

(a) (b)

Figure 2.18: Metastable projection normalized profile (a) and reconstructed metastable density profile (b) for beam sizes of 1x1 and 2x2 mm and 6 mm of undulator gap. The gas pressure was 100 mbar in both cases.

2.20). The reason is the same as before: event at the lower pressure case, the gas density is high enough to prevent fast electrons to diffuse far away from the X-ray beam and to prevent metastable atoms to diffuse within their lifetime from the place where they are born. This was true in the OES case where the measured states were 2p states, which decay rapidly to 1s states; in this case we have measured the metastable 1s5 state which decays to the ground state only through a previous transition to a resonant level, assisted via electron collision. The fact that both spatial profiles yield similar results means that also the diffusion losses of neutral heavy species is small, in any case smaller than the decay rate of the metastable atoms.

The results of the metastable density profiles will be used in chapter 5, together with those of the 2p density profiles and the X-ray power absorption and transmission, to validate a first principles model developed in chapters 3 and 4.

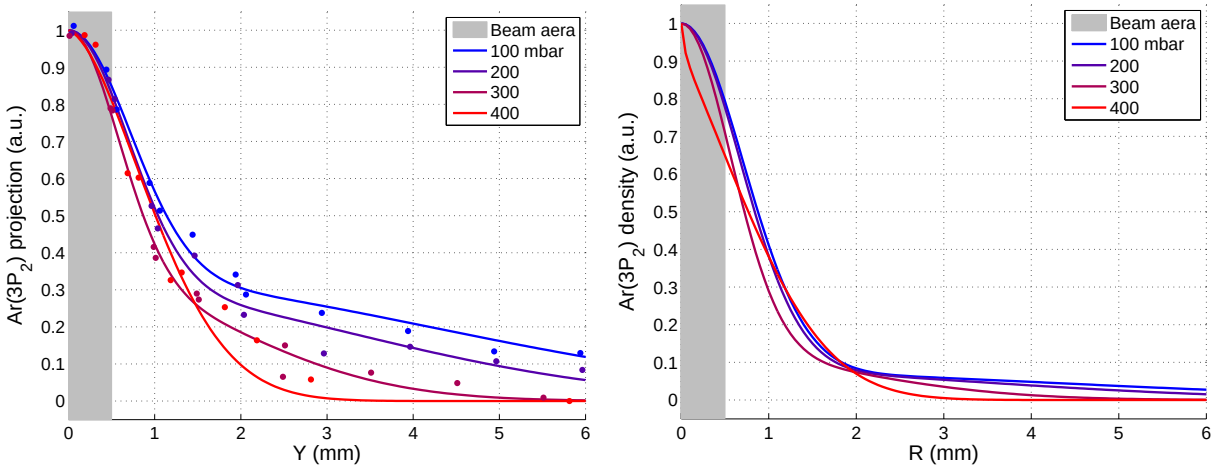

(a) (b)

Figure 2.19: Metastable projection normalized profile (a) and reconstructed metastable density profile (b) for a beam size of 1x1 mm and 6 mm of undulator gap.

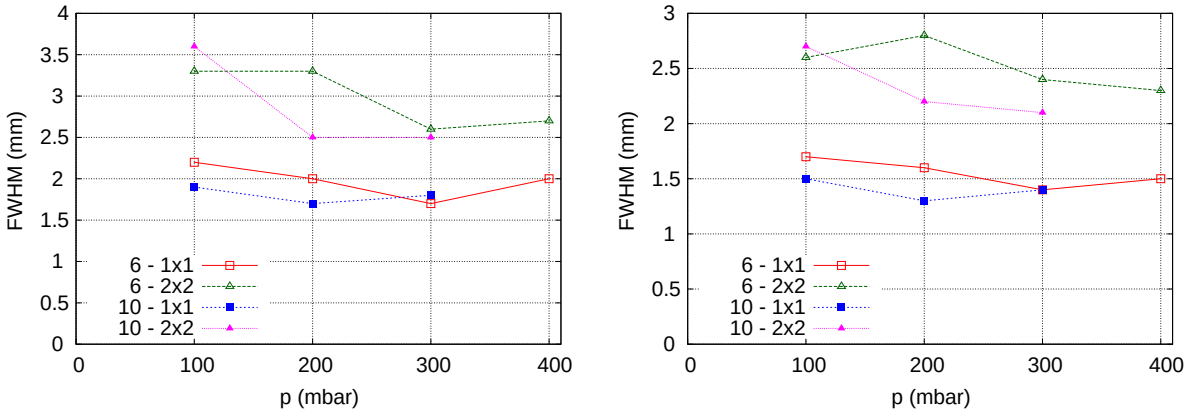

(a) (b)

Figure 2.20: FWHM of the $Ar(3p_2)$ projection profile (a) and density profile (b).

Chapter 3

High energy and Monte Carlo modeling

To predict the X-ray absorption by the gas attenuator, we need to model the X-ray absorption processes, the slow-down of photoelectrons, the plasma processes and the heat transfer. All these processes have very different characteristic energies, from the keV range of the X-ray absorption to the meV range of the heat transfer. A global model including selfconsistently all of them would be extremely inefficient and computationally demanding due to the orders-of-magnitude difference on the characteristics energy. Therefore, a set of modules has been developed, each one treating in detail the phenomena corresponding to each energy range. The consistency of the results is obtained after a few iterations between these modules.

The high energy processes described in this chapter includes the X-ray absorption by the gas, the decay of the highly excited ions after photoionization and the slow-down of photo and Auger electrons from their initial energy down to a few eV [30]. It consist on a Monte Carlo model that simulates the evolution of the electrons after the X-ray absorption. Monte Carlo models are based on the simulation of a representative number of particles and are widely used in high energy and nuclear physics. The use of analytic formulas is practically impossible because of the anisotropy of the problems (which prevents the use of Beer-Lambert laws) and the non-equilibrium of the particle population, both with itself and with the surroundings (which prevents the use of diffusion equations).

Geant4 [31,32] and PENELOPE [33,34] are two well-know examples of Monte Carlo software, which have also been applied to calculations of synchrotron radiation interaction with matter [35, 36]. However, these models assume a fixed background with constant properties like density, temperature, composition or electromagnetic fields, so that any change in the background properties would require a new run of the simulation. In addition, they model the transport of particles (in particular electrons) only down to ∼1 keV, which makes them impractical for the simulation of most types of plasmas.

In plasma modeling, Monte Carlo models are usually coupled to Particle-In-Cell (PIC) models, leading to the so called PIC-MC models [37]. In the PIC models the electric field present in the plasma is calculated at every defined time step from the charged species populations and boundary conditions, and the movement of individual charged particles under this field is then simulated. The Monte Carlo algorithm tracks the collisions between particles every time step, modifying consequently the energy and velocity of the particles. Such PIC-MC models have been applied to a variety of plasmas [38, 39], including the plasmas generated from photon sources [40]. However, these models become impractical when the particle density and the number of collisions increases too much, so that the time step becomes too small to obtain a result within a reasonable computing time.

The high energy model developed for the gas attenuator calculates the X-ray absorption processes and the decay of inner shell ions analytically, then switching to a Monte Carlo model for the electron slowdown to energies of a few eV. The diagram of the algorithm is shown in figure 3.1. The gas density and composition, attenuator geometry, electric field and background electron population are taken as input on every simulation. The results of the model are the number of ions and excited species and the properties of the electron population, as well as the power lost through radiation processes. This model is not self-consistent on its own, since it requires the input on the background media. The complete self-consistent model in achieved by adding a Fluid Model (described in chapter 4) which takes the output of the MC model and calculates the steady state gas and plasma parameters, including those needed by the MC model as input.

The time-dependent parameters of the ESRF X-ray beam are shown in table 3.1 for the 3 main modes of operation. The X-ray spectrum depends on the source; the one used here corresponds to the U18 undulator of ID06 (figure 2.1). In this work we have limited ourselves to the 'continuous' mode, in which the frequency of the flashes is high enough to consider the X-ray beam as continuous in the fluid model. The high energy model will simulate single flashes, assuming that all the absorption processes happen in the same instant. After a time of usually 0.5 to 2 ns, as will be shown in the results of the simulations, the electrons have lost most of their energy relaxing towards a steady-state and the MC simulation stops.

Operation mode	continuous	16-bunch	4-bunch
# of bunches	992	16	4
current (mA)	200	90	16
bunch size (ps)	20	48	55
Flash frequency (MHz)	352.2	5.68	1.42
Time between bunches (ns)	2.84	176	704
Photons per flash	divide total intensity (ph/s) by frequency		

Table 3.1: Electron beam parameters of the main ESRF operation modes. The energy of the electrons is 6 GeV in all cases and the ring perimeter 882 m

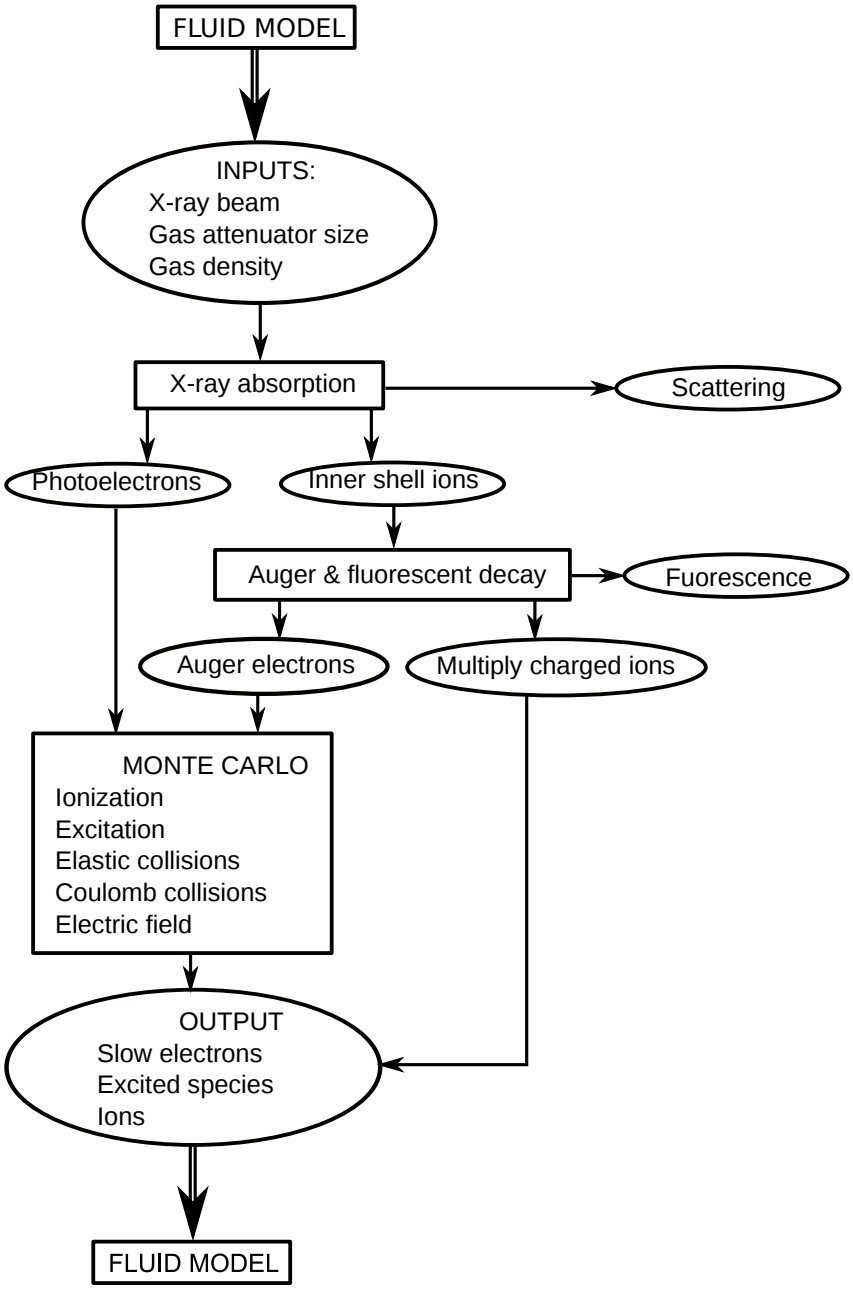

Figure 3.1: Flow diagram of the model for the high energy processes. Part of the model inputs (gas density and steady-state electron population) are taken from the fluid model. The X-ray absorption and the excited ion decay are calculated analytically from the cross sections and decay ratios. The electron slow down is calculated using a Monte Carlo model. The outputs are sent to the fluid model, which calculates the steady-state solution, closing the loop.

3.1 Photon interaction processes

The first step in the modelling of the attenuator is the absorption of the X-ray photons by the gas. There are three competing processes in the energy range of the X-rays: photoionization, Compton (inelastic) scattering and Rayleigh (elastic) scattering. The photoionization is the dominant one at the relevant energy range (figure 3.2) while at higher energies the total cross section decreases and the gas becomes virtually transparent to the X-rays.

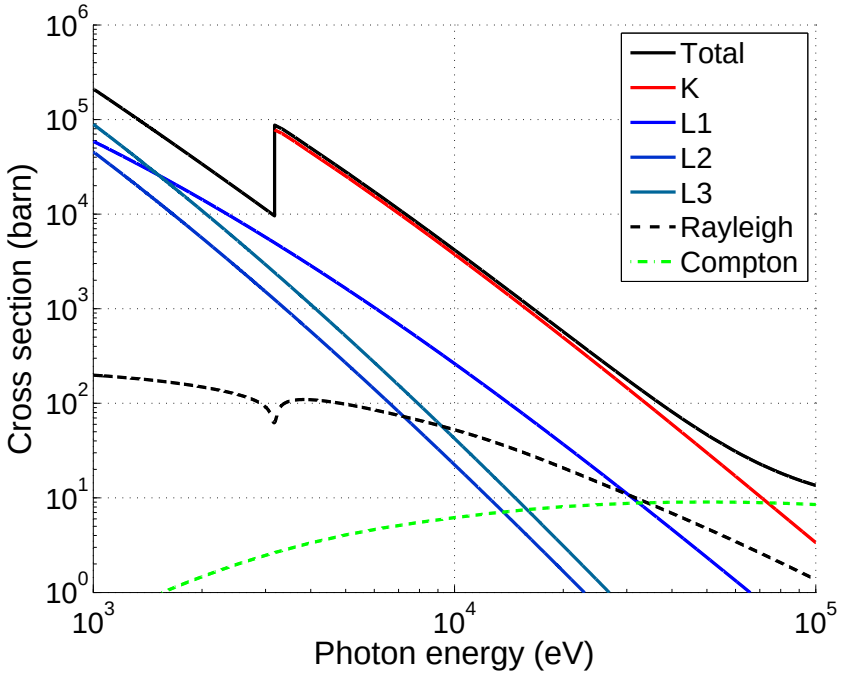

Figure 3.2: Photon interaction cross sections for Ar. Above the K edge, most of the ionization occurs in the K shell. Data taken from the EPDL library [41]

The absorption of the X-ray beam is described by the Beer-Lambert law (equation 2.1) using the total cross section, resulting from the sum of all the different processes considered. The number of photoelectrons is then calculated analytically

$$N_{e,X}(E - E_X) = N_\gamma(E)\frac{\sigma_X(E)}{\sigma_T(E)}\left(1 - e^{\rho\sigma_T(E)\Delta z}\right) \tag{3.1}$$

where $N_{e,X}$ is the number of photoelectrons emitted from the X shell (X = K, L1, L2, L3...), E_X and σ_X are the binding energy and cross section of the X shell respectively,

σ_T is the total cross section of the photon processes and N_γ is the number of incoming photons. The initial energy of the photoelectrons is that of the absorbed X-ray photon minus the binding energy of the atomic shell. Due to the different binding energy of each atomic shell, the photoelectron energy spectrum contains replicas of the incident white beams, at energy offsets given by the binding energies of the atomic shells (figure 3.3). The cross section data for these processes is well know and has been compiled in several databases. Here we have used the Evaluated Photon Data Library (EPDL [41]).

The direction of the emitted photoelectron is given by the Sauter-Gavrila equation for polarized light [42]:

$$\frac{d\sigma}{d\Omega} = \frac{4}{m_e^2}\alpha^6 Z^5 \frac{\beta^4(1-\beta^2)^2}{\left[1-(1-\beta^2)^{1/2}\right]^5} \cdot \left\{ F\left(\beta,\theta,\phi\right) \cdot \left(1 - \frac{\pi\alpha Z}{\beta}\right) + \pi\alpha Z G\left(\beta,\theta,\phi\right) \right\} \quad (3.2)$$

where $\beta = v/c$ is the electron velocity in speed of light units, Z is the atomic number of the element, α is the fine structure constant and F and G are two functions dependent only on the Lorentz factor and the scattering angles. At low energies, the dependence of the cross section with θ and ϕ can be approximated by $sin^2(\theta)$ and $cos^2(\phi)$ respectively, so that the most likely direction of emission is in perpendicular to the photon direction and in the plane of polarization. In general the synchrotron radiation is polarized in the horizontal direction; the photoelectrons will be then emitted preferentially in the horizontal plane and in perpendicular to the X-ray beam. Although we could expect that, at the gas pressure of the attenuator (few hundred mbars), the angular distribution of the electron velocity will become rapidly isotropic, we have keep the angular dependence of the electron emission so that the model could be used for experimental conditions with lower pressure.

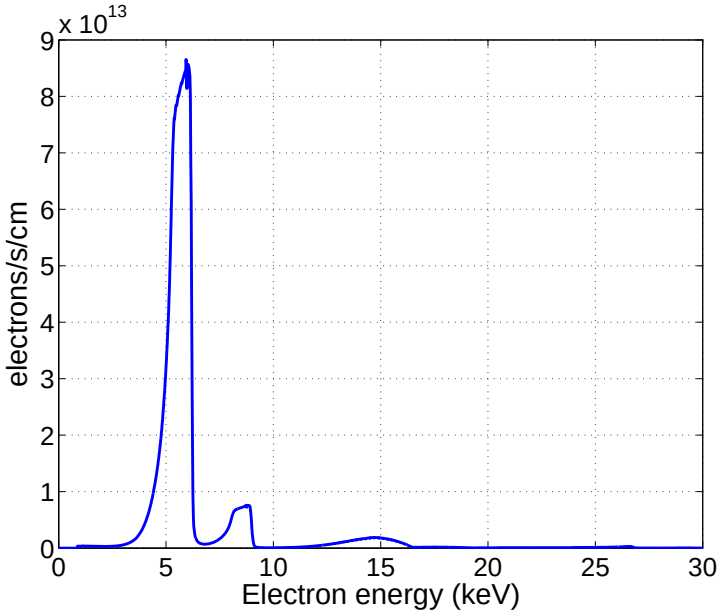

Figure 3.3: Photoelectron energy histogram (bin size 100 eV) after the absorption of an X-ray beam emitted by a U18 undulator at 6 mm gap (first harmonic at 10 keV) by 200 mbar Ar right after the entrance window. Note the doubled peak at 6 and 8 keV corresponding to the first harmonic of the X-ray spectrum shifted by the K and L binding energies respectively.

3.2 Auger and fluorescent relaxation

The inner-shell vacancy of the ions created after photoionization is immediately filled with an electron from a higher shell, releasing the extra energy via either X-ray fluorescence or Auger emission. In the X-ray fluorescence, a photon is emitted carrying the extra energy, while in the Auger emission another electron from an outer shell is ejected, thus increasing the charge of the ion. In both cases the energy of the emitted particle is fixed and determined by the difference between the initial and final states of the system. Usually, the electron that occupies the vacancy leaves another vacancy in an intermediate shell which also decays; a cascade occurs that leaves the atom in a highly charged state after emitting several photons and/or electrons [43, 44]. Both the yield and energy of every decay channel for the first step of the cascade are known and tabulated in databases [45]; in this work we used those published in the Electron Atomic Data Library (EADL, [46]).

In order to calculate the number of multiply charged ions, photons and electrons emitted from the inner shell ions, we need the probabilities of emission of Auger and fluorescent photons from each inner shell, taking into account the complete cascade, together with

the probability of the ion ending up with a charge of n+:

$$N_e(E_i) = P_e(E_i, X) \cdot N_{Ar}(X) \tag{3.3}$$

$$N_{Ar}(n+) = P_{Ar}(n+, X) \cdot N_{Ar}(X) \tag{3.4}$$

where $N_{Ar}(X)$ is the initial number of ions with a vacancy in the X shell (X = K, L1, L2, L3...), $P_e(E_i, X)$ is the probability of emitting an electron of energy E_i from a ion with a vacancy in X, $P_{Ar}(n+, X)$ is the probability of ending up with a charge $n+$ from an initial X vacancy, and N_e and N_{Ar} are the final number of Auger electrons and ions respectively. Because of the cascade effect, a single ion can emit several electrons, so the sum of emission probabilities might be higher than one: $\sum_i P_e(E_i, X) \neq 1$. The sum of probabilities for the different charge states still must be equal to one: $\sum_n P_{Ar}(n+, X) = 1$. The final charge state can be taken from the literature [47, 48] or calculated from the individual decay probabilities taken from databases [48]. Once the probabilities of the complete cascades are known, they are multiplied by the total number of inner shell ions following equations 3.3 and 3.4 to obtain the total number and energy of Auger electrons (figure 3.4) and the total number of relaxed, multiply charged ions (figure 3.5).

The inner-shell ion deexcitation process is independent from the generation of the ion: the atom remain a small time (in the order of femtoseconds or smaller [49]) in the highly excited state before decaying. Therefore, contrary to the photoelectrons, the direction of the emitted photons and electrons is completely random; when the electron slow-down is computed, the initial direction is taken randomly from all the available space directions.

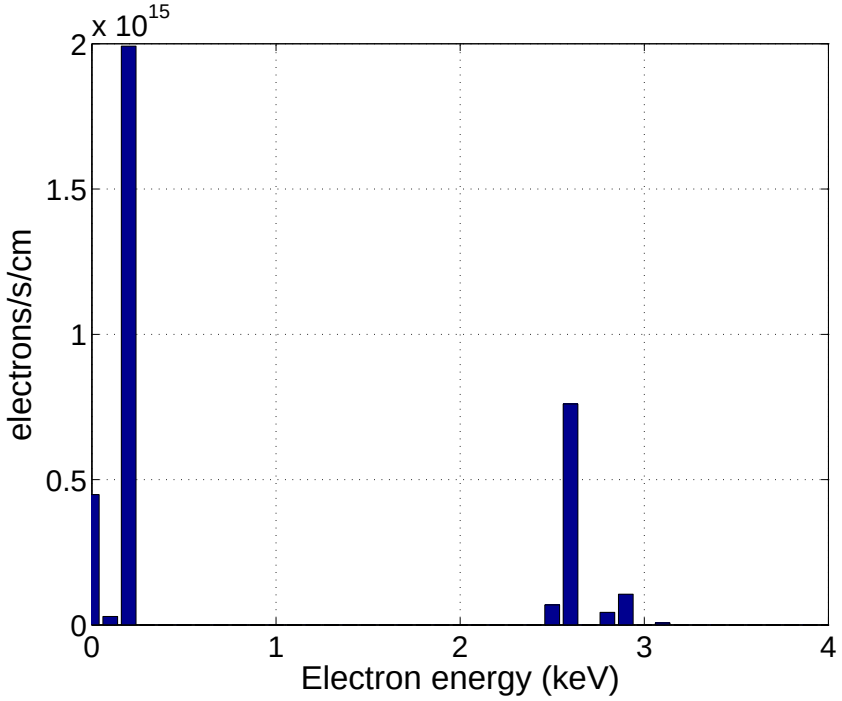

Figure 3.4: Histogram of the Auger electron population after relaxation of the inner-shell argon ions. Bin size 100 eV.

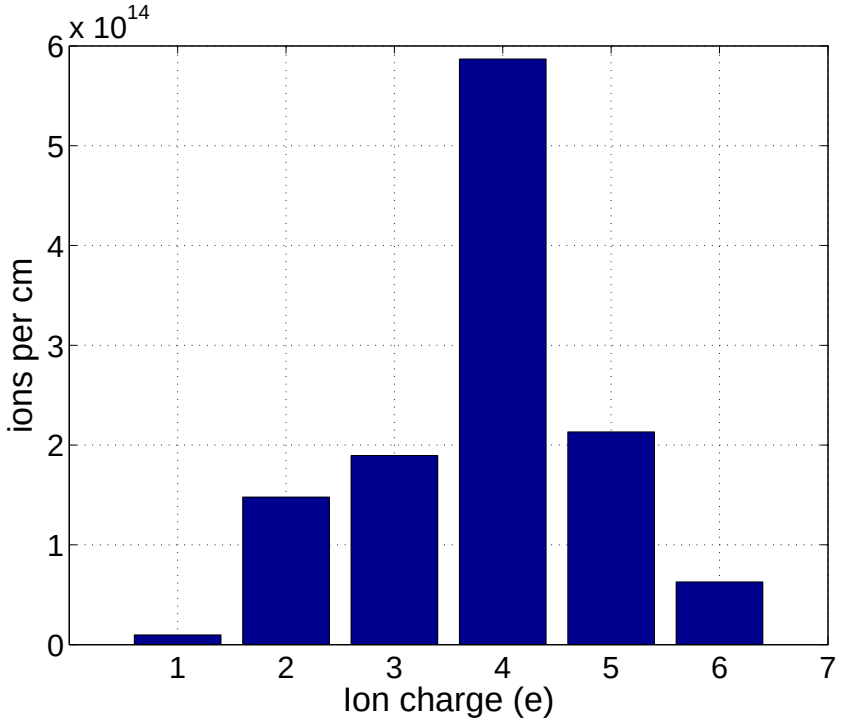

Figure 3.5: Number of single and multiple-charged argon ions after photoionization and Auger and fluorescent deexcitation. All the electron vacancies of the ions are in the outermost shell.

3.3 Electron collisions

At this point we have calculated the high energy electron population and its initial energy distribution, which is far from equilibrium. Hence a continuous modelling approach, fluid for instance, does not seem appropriate. These energetic electrons will start to interact with the surrounding gas, loosing energy in the process and relaxing towards an equilibrium distribution. It is this relaxation process what will be modelled using Monte Carlo, simulating a large number of electron from the initial energy to the thermal one.

Cross sections

The possible collisions of the electrons with the gas atoms are elastic, excitation and ionization collisions. The elastic ones will take place at any electron energy, while the excitation and ionization will take place only if the electron energy is above the collision energy threshold. Due to the large energy range of the slow-down process (from keV to a few eV), the cross sections has been taken from two databases, the Evaluated Electron Data Library (EEDL [50]) and the LXCat [51]. The EEDL is a reference database for nuclear physics, used in PENELOPE and in Geant4, and accurate from a few hundreds of eV to the GeV range. It includes electron ionization collisions for each subshell but only a single inelastic cross section (figure 3.6). LXCat, on the other hand, is a database built for the low-temperature plasma research, to calculate reaction rates and transport coefficients in the eV range among other objectives. It includes the excitation cross section for every excited level but only a single ionization cross section from the outermost shell, the only one possible for the low energy electrons. The problem is that, due to their different scope, the two databases give different cross sections in the overlapping region (figure 3.7). The solution taken here is to use the high energy EEDL database for electron energy above 100 eV and the LXCat for the rest. The choice of this threshold is somehow arbitrary and, nevertheless, changes little the final results: similar results were found by setting the threshold at 1 KeV and at 100 eV. We have chosen to keep it at 100 eV to account for the ionizations in the inner shells, which may take place down to 150 eV for argon.

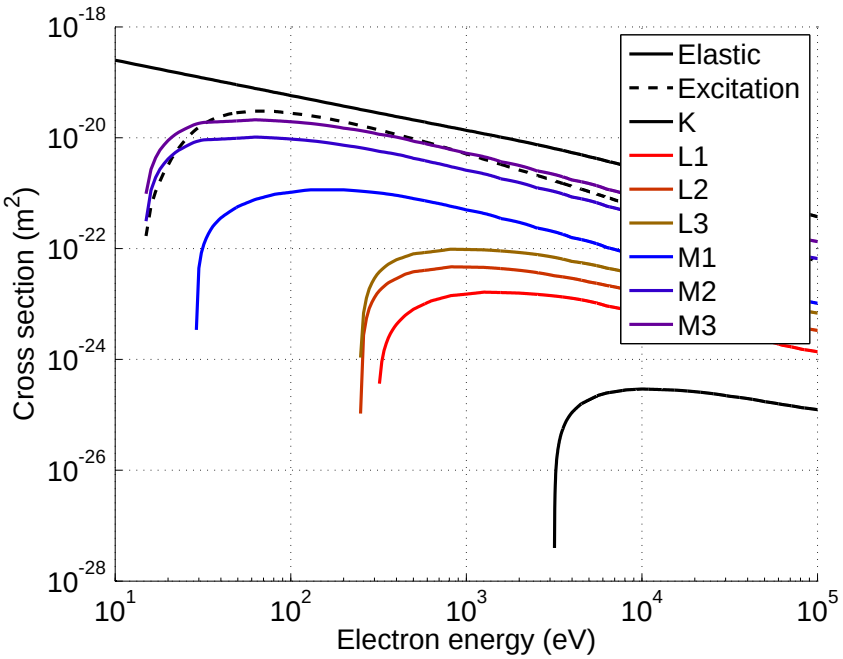

Figure 3.6: Cross sections for electron-impact processes in argon, including ionization for every subshell, as given by EEDL [50]. The inner-shell ionization has a low occurrence probability but may lead to higher charged ions.

In addition, the high energy electrons carry enough energy to ionize several times an atom in a single collision. While these collisions are less likely than the single ionization collisions, the multiply charged ions may play a role due to the stronger forces acting on them for the same electric fields and to their higher internal energy with respect to single-charged ions. The cross sections used here [52] are shown in figure 3.8.

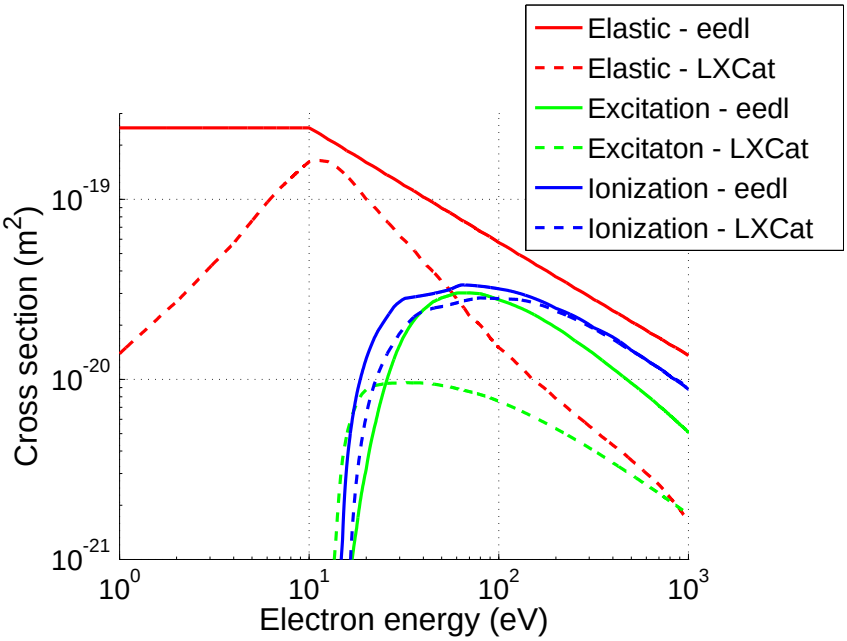

Figure 3.7: LXCat [51] vs. EEDL [50] electron-impact cross sections for elastic, inelastic and ionization collisions in argon. The different scope of each database (eV range for LXCat, keV and higher for EEDL) results in different values of each database for the same collision in the overlapping region.

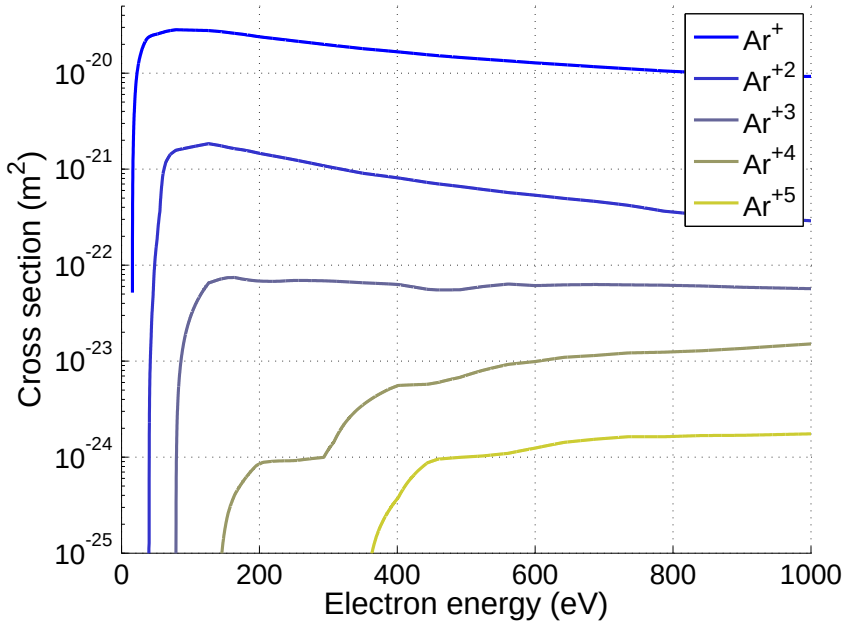

Figure 3.8: Cross section for electron-impact multiple ionization [52]. The electrons produced by the X-ray photoionization have an energy high enough to multiply ionize neutral atoms.

Scattering angle and energy loss

Once the total cross section of every process is known, we need the energy loss and scattering angle (or differential cross section) for every process. The differential cross section for all the collision processes can be taken as [53]

$$\frac{\sigma(\theta, E)}{\sigma(E)} = \frac{E}{4\pi\,(1 + E \cdot sin(\theta/2)) \cdot log(1 + E)} \tag{3.5}$$

where E is the electron energy in eV. Even if it is only approximate, this differential cross section will be good enough because the multiple collisions will tend to reduce the anisotropy of the system, so that the final result will be independent of the details, as long as the integral value remains constant. Then, the scattering angle can be sampled with [37, 38]:

$$\theta = acos\left(\frac{2 + E - 2(1 - E)^R}{E}\right) \tag{3.6}$$

where E is again in eV and R is a random number between 0 and 1.

The energy loss does depend on the collision type. For the elastic collisions, it depends on the scattering angle and can be obtained using classical collision mechanics [37]:

$$E_{el} = E_0\left(1 - \frac{2m_e}{M}(1 - cos(\theta))\right) \tag{3.7}$$

where θ is the scattering angle, m_e is the electron mass and M is the ion mass. Note that, due to the mass difference, the energy loss is in the order of 10^{-5} of the initial energy. However, it might became of importance at low electron energies, when it becomes the only energy loss mechanism. The energy loss after an excitation collision is precisely the energy of the excited level:

$$E_{exc} = E_0 - E_{level} \tag{3.8}$$

where the energy loss due to the change of direction has been neglected, being orders of magnitude smaller than the excited level. The energy loss after an ionization collision must

take into account both the binding energy and the energy of the secondary electron(s)

$$E_{ion} = E_0 - E_{level} + \sum_n E_{n,sec} \tag{3.9}$$

where E_{level} is the binding energy and $\sum_n E_{n,sec}$ is the sum of energy of the secondary electrons, calculated as

$$E_{sec} = B \cdot tan\left(\frac{E_0 - E_{level}}{2B}\right) \tag{3.10}$$

where the energies are in eV and B is an element dependent parameter, whose value for the gases used in this thesis is 10 for Ar and 9.7 for Kr [54].

Collision sampling and null collision method

The magnitude used to calculate both the time between collisions and the collision type is the collision frequency, defined as the number of collisions per second

$$\nu = \rho\sigma v \tag{3.11}$$

where ρ is the scatterer's number density in m^{-3}, σ is the relevant cross section in m^2 and v are the electron velocity in m/s. The probability of collision after a given time is

$$P_{col} = 1 - exp\left(-n\sigma v\Delta t\right) = 1 - exp(-\nu\Delta t) \tag{3.12}$$

where Δt is the elapsed time and P_{col} is the collision probability, with values between 0 and 1. This equation can be inverted to sample the free flight time between two collisions

$$\Delta t = -\frac{log(1-R)}{\nu} \tag{3.13}$$

where R is a number between 0 and 1. By sampling randomly R between 0 and 1 we obtain the time between two collisions.

The cross section used in the previous equations should be in principle the total one,

sum of the considered cross sections of the individual collisions. However, this might lead to some difficulties, taking into account that the electron velocity and kinetic energy may change between two collisions due to electric fields or Coulomb collisions (described in the next section). The solution is to add a virtual collision ("null collision"), so that the total cross section and therefore the collision frequency are constant, independent of the electron energy and equal to the maximum real cross section, i.e. before adding the "null collision":

$$\nu_{tot}(E) = Cte = nv(\sigma_{el}(E) + \sigma_{exc}(E) + \sigma_{ion}(E) + \sigma_{nul}(E)) \tag{3.14}$$

The specific collision is then chosen from a second random number, mapped onto the cumulative sum of the different cross sections. The null collision does not modify the velocity or state of the electron, so we are not adding any artificial effect on the plasma model. This method is widely used in high energy codes like PENELOPE and in low temperature plasma simulation codes [37].

An exception to the null collision method is made here for very low energy electrons. If an electron has an energy much below the smallest excitation energy, the only collision possible is the elastic one. The elastic cross section at very low energies is much smaller than the maximum total cross section (see fig. 3.7), which results in a large fraction of null collisions in this energy range. The gain in avoiding to calculate the collision frequency in every step is offset by the large number of collisions. Therefore, if the energy of the electron is lower than a threshold, the collision frequency is calculated at every step, resulting in a more expensive computation but also in a reduction of the number of steps.

3.4 Coulomb interactions

Apart from the electron collisions with neutral atoms, we have to consider the electric forces acting on the electrons. The main challenge of these interactions is that the Coulomb potential has an infinite range, so that they cannot be easily separated into individual events with a free-fall trajectory between them. The solution employed here is to use a background electrical field accounting for the long range interactions and an

expression for the deflection angle in the short range collisions.

The space-charge electric field is calculated by the fluid model from the steady state, background cold electron and ion populations; the fast electrons (the ones simulated by the MC model) are neglected in the space charge field calculations because their number is considered small enough compared to the cold ones. The trajectory of the electron between two binary collisions with heavy species can be calculated by solving the equation of motion with the time between collisions previously calculated:

$$m_e \ddot{\boldsymbol{x}} = q_e \boldsymbol{E} \tag{3.15}$$

where $\ddot{x}$ is the acceleration of the electron and $\boldsymbol{E}$ the electric field.

To account for the collective phenomena, i.e. Coulomb Collisions, we select an electron from the background cold population with a random direction and energy within the electron energy distribution function (eedf) of that population. The collision is performed in the center of mass (CM) reference system, in which the "collective" scattering angle θ is calculated using the auxiliary variable δ as [55, 56]

$$\delta = tan\left(\frac{\theta}{2}\right) \tag{3.16}$$

which follows a normal distribution with a variance given by

$$< \delta^2 >= \frac{q_1^2 q_2^2 n_i ln\Lambda}{8\pi\epsilon_0^2 m_{12}^2 u^3}\Delta t \tag{3.17}$$

where q_i is the charge of the particles, ϵ_0 is the electrical permittivity, m_{12} is the reduced mass of the system, u the relative velocity in the CM system, n_i is the charged particle density, Δt is the time between collisions with neutrals and $ln\Lambda$ is the Coulomb logarithm. The δ value is randomly sampled from this distribution.

Only collisions between fast electrons and background electrons are considered in this model. The number of fast electrons is assumed to be much smaller than that of cold,

background electrons. This can be validated only a posteriory, after the solution of the complete model has been calculated, as will be done later in section 4.4. As for the ion-electron collisions, the exchange of energy will be negligible compared to that of the electron-electron collisions, so that they only contribute to make the velocity distribution more isotropic.

The effect of the electron-electron collisions will be the exchange of energy between the fast and background electron populations, thermalizing the fast electron population and, given a long enough time, reaching and equilibrium by having the same electron temperature [57].

3.5 Monte Carlo algorithm

The simulations were performed in a 2D domain limited by the diameter of the gas chamber and perpendicular to the X-ray propagation direction. The velocity of the electrons is simulated in 3D and only the positions are projected onto the 2D domain. The position of the simulated domain along the attenuator can be changed. The inputs of the model are the X-ray beam properties (spectrum and total power) set by the user, and the gas and steady-state plasma properties, obtained from the previous loop of the fluid model output. The first step is the absorption of the X-rays by the column of gas in front of the simulated sector. Then, the absorption of the X-ray in the simulated sector is calculated analytically as described in section 3.1, followed by the subsequent Auger and fluorescent cascades described in section 3.2. The resulting fast electron distribution is taken as the starting population at time 0 for the Monte Carlo simulation. The primary and secondary electron trajectories and interactions are then simulated, the time of the simulation being fixed manually as an input. For the pressure and electron energy used here, a time of around 1-5 nanoseconds is usually enough to reduce the electrons energy below the lowest excitation threshold; at lower energies the electrons will just keep thermalizing and diffusing without generating any further secondary particle. The simulation tracks the collisions of a given number of fast electrons for a given simulated time, after which the

spatial and energy electron distributions, as well as the number of heavy particles (ions and excited species) is saved and used further as input for the fluid model.

3.6 Electron slow-down results

The results of the high energy model can be studied independently from those of the complete model (high and low energies) to observe the time evolution of the fast electron population, the power balance and the outputs given to the fluid model. The input parameters in table 3.2 are the ones used for the simulation whose results are discussed in this section. The position of the simulated 2D slice of the attenuator is right after the entrance window, which means that the X-ray beam is not attenuated by any previous mass of gas.

Undulator gap	6 mm
Synchrotron current	200 mA
X-ray total power	654 W
X-ray beam size	2x2 mm^2
Gas pressure (Ar)	200 mbar
Attenuator radius	18 mm
Distance to front window	0 cm

Table 3.2: Input parameters for the simulation of the time evolution of the fast electron population.

Time evolution

The time evolution of the energy distribution of the electron population after the arrival of a single X-ray flash is shown in figures 3.10 and 3.9, one with a keV scale and the other one with an eV scale. In the first one, we see the slow down of the photo- and Auger electrons, which at short times (0.01 and 0.05 ns) still keep a large fraction of their initial energy and the distribution also keeps a memory of the original distribution (figures 3.4 and 3.3). However, already after 1 ns all the electrons with energies in the keV energy range have been slowed down. Accordingly, the number of electrons with energies

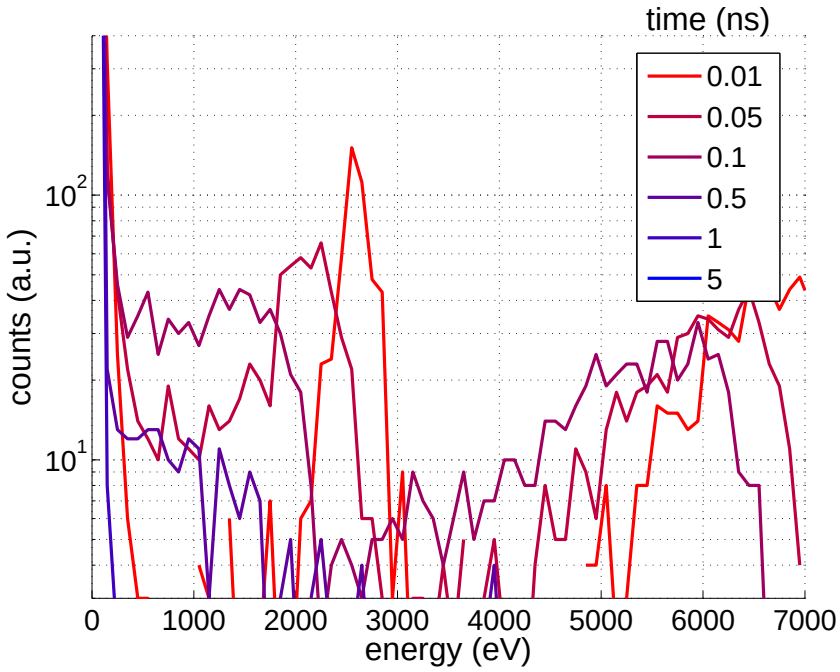

Figure 3.9: Histogram of the simulated electron population energy distribution at different simulation times after the arrival of an X-ray flash. The plots only shows the high energy electrons. Input parameters in table 3.2.

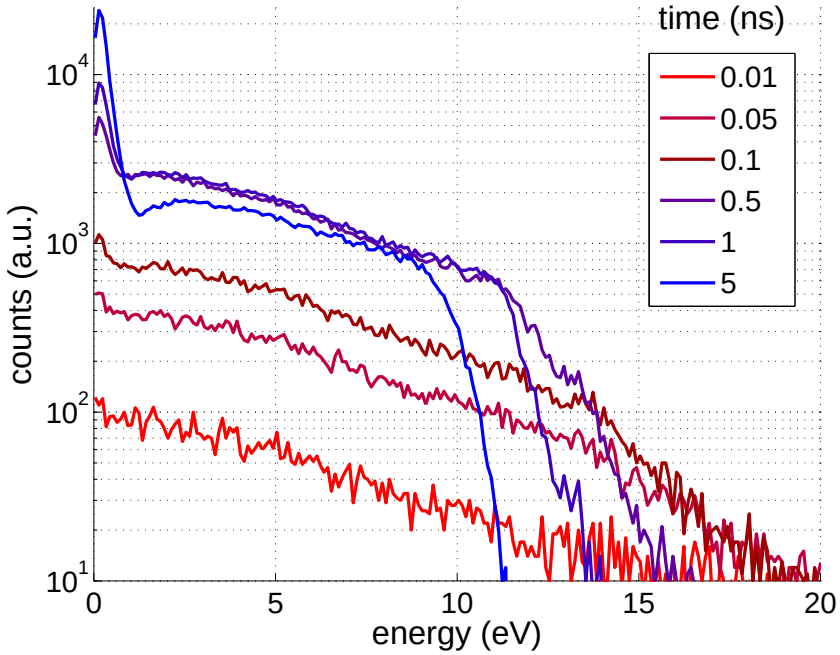

Figure 3.10: Histogram of the simulated electron population energy distribution at different simulation times after the arrival of an X-ray flash. The plots only shows the low energy electrons. Input parameters in table 3.2.

in the eV range is small at short times and increases due to secondary ionizations and slow-down of fast electrons, as can be seen in figure 3.9. Already after 0.5 ns, there is a depletion of the electron population at energies above ∼12 eV, which becomes more and more pronounced at longer (1 and 5 ns) times. Also, the electron population increases steadily between 0.01 and 0.5 ns, after this time we see an increase only below 1-2 eV while the population at higher energies decreases. The reason is that the high energy electrons that created secondary electrons have already dissipated all their energy, so that after that moment, only a redistribution of the energy occurs. In particular, what we see is how the electron population tends to an equilibrium with the background electron population, which has an electron temperature of only 0.3 eV. This is also the reason for not continuing the Monte Carlo simulation any further: the diffusion and thermalization of electrons at this pressure will take a too long time to simulate with this technique, while it can be efficiently simulated by a fluid model without losing any information or effect of fast electrons that we see have already disappeared. Also, the fluid model simulates the losses of electrons in the bulk of the plasma, which happens only at low energy and that has not been included in the Monte Carlo model.

The increase of the electron population during the first nanosecond can also be seen in the spatial distribution of the electrons (figure 3.11). The density increases sharply in the area illuminated by the X-ray beam, while diffusing only slowly towards the attenuator walls. After the first nanosecond the increases stops and we only have diffusion; 5 nanoseconds after the X-ray absorption the density in the central region has started to decrease due to the diffusion. This tendency can be clearly seen in the total number of electrons in the simulation at every time (figure 3.12). In subsequent simulations, the simulation time will be chosen so that most of the electrons have an energy lower than the ionization energy, so that the electron population will not grow further. The resulting output is then passed to the fluid model to obtain the steady state of the attenuator.

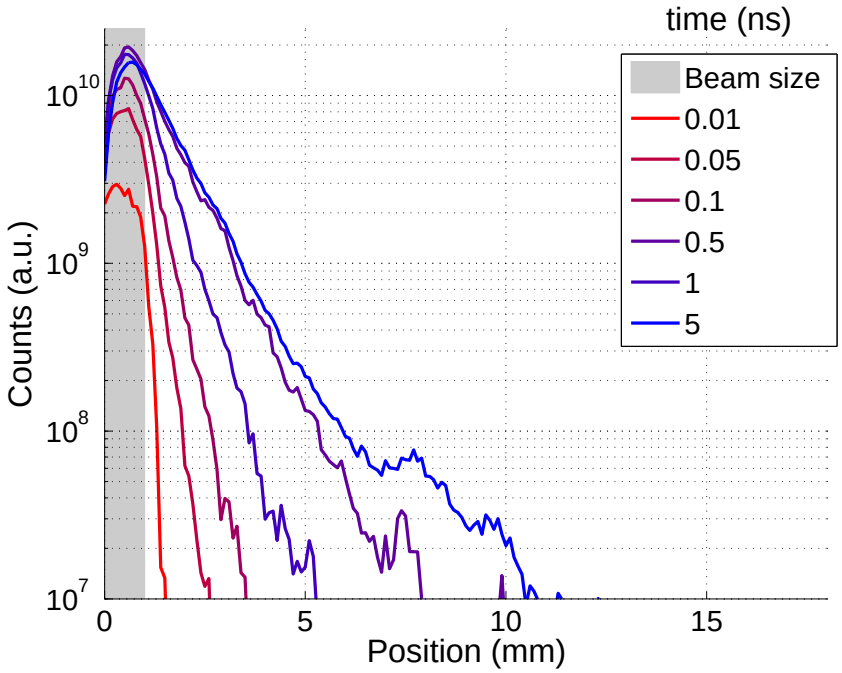

Figure 3.11: Histogram of the simulated electron population spatial distribution (radial coordinate) at different simulation times after the arrival of an X-ray flash. Input parameters in table 3.2.

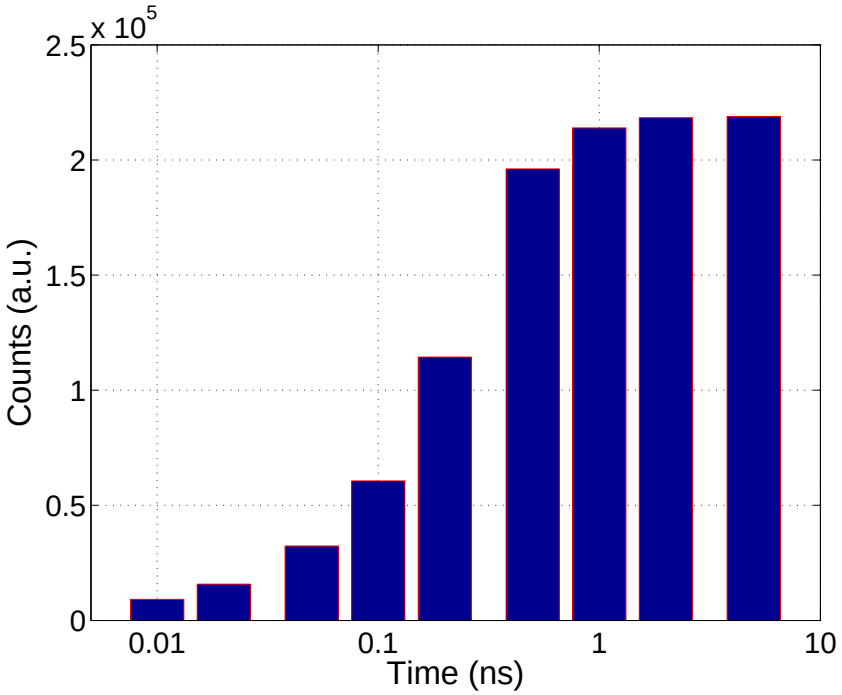

Figure 3.12: Total number of electrons in the simulation as a function of the time after the arrival of an X-ray flash. Input parameters in table 3.2.

Power balance

We can look at the power balance at each of the steps of the high energy model: after the X-ray absorption, after the Auger and fluorescent cascade and after the MC simulation of the fast electrons. On each step some of the power will be directly lost due to scattering and fluorescent decay, that reaches the walls of the attenuator before interacting further with the gas.

Input power		654 W
Energy transfer mechanism		Power loss W/cm
X-ray absorption	Absorbed power	1.82
	Photoionization	1.78
	Scattering	0.04
Fluorescent and Auger decay	Photoelectrons	1.27
	Auger electrons	0.45
	X-ray fluorescence	0.04
	Potential energy (ions)	0.02
Electron slow down (MC)	Input (fast electrons and ions)	1.74
	Slow electrons	0.27
	Single ions	0.85
	Multiple ions	0.11
	Excited species	0.48
	Elastic losses	0.03

Table 3.3: Power balance of the X-ray absorption processes and of the ion deexcitation. Similar proportions are obtained for different spectra of the U18 undulator. Input parameters in table 3.2.

The power balance on each step of the high energy model is shown in table 3.3. In the first step, the X-ray absorption, most of the power is absorbed via photoionization, with only a small fraction scattered. This will be also true for krypton, where the photoionization cross section is also larger than the scattering processes for the keV energy range.

The subsequent deexcitation of photoions takes place for argon mostly via Auger decay, with only a small fraction emitted by fluorescence. The result after this first two steps is that around 95% of the total absorbed power is taken by free electrons, the rest either lost via scattering and fluorescence or kept as potential energy in the multiply-charged ions. This proportion will be different for krypton, where the fluorescence yield of the K

holes is much larger than for argon (0.64 in Kr versus 0.11 in Ar).

Finally, after the slow-down of the fast electrons, the input power is distributed between the single and multiply charged ions, excited species and kinetic energy of the electrons (table 3.3). While a majority of the energy goes as potential energy on the ions (∼55%), significant fractions end up as potential energy of the excited species (∼28%) and as kinetic energy of the electrons (∼16%). The amount of power lost via elastic collisions (including Coulomb interactions) is very small compared with the other mechanisms, which could be expected since the loss in every single collision is much greater for ionization and excitation than for elastic collisions. This will also be true for krypton, where the only significant difference in the MC power balance is a higher fraction of power lost via excitations.

The little importance of the elastic collisions in the high energy module is due to the initial high energy of the electrons and the short simulation time. Once an electron slows down to an energy smaller than the lowest excitation energy, the only possible collisions are the elastic ones. Therefore, even if not significant in the slow-down process, these elastic collisions will be fundamental to the transport properties and the thermalization of the slow electrons and the heating of the gas. These effects will be included in the fluid model described in chapter 4.

Simulation outputs

The main output parameters of the MC model needed as inputs for the fluid model are the number of electrons, ions and excited species created per unit of time, as well as the average electron energy. The absolute numbers for the simulation described before are shown in table 3.4. Both the total absorbed power and number of electrons are given for a slice of 1 cm thickness along the attenuator, where the axial gradients are assumed to be negligible. This assumption must be verified a posteriori on each case, by comparing two contiguous simulated disks. The number of ions and excited states generated is given as a fraction of the total electron number; we have found that these fractions do not

vary significantly when simulating different gas pressures of X-ray sources. To simplify the fluid model, all the multiply charged ions generated in the MC model are assumed to neutralize fast to less charged ions by charge transfer collisions with neutral atoms, so that all the charge carried by them is at the end carried by Ar^{+2} ions. We can verify that the sum of the single and double ion charges equals to one: we have the same amount of positive and negative charges.

Absorbed power (W/cm)	1.82
$e^-/s/cm$	$3.62 \cdot 10^{17}$
$< E_{e^-} >$ (eV)	4.88
N_{Ar^+}/N_{e^-}	0.90
$N_{Ar^{2+}}/N_{e^-}$	0.05
N_{Ar^*}/N_{e^-}	0.63

Table 3.4: Outputs of the high energy Monte Carlo simulation for the absorbed power, equilibrium species rates and mean electron energy, using the input parameters described in table 3.2.

Conclusions

The results obtained in the high energy model show that the main X-ray absorption process is the photoionization, followed by Auger decay, which results in a population of fast electrons and multiply charged ions. These fast electrons slow down to energies in the eV range within a few ns when the pressure is of a few hundreds of mbars, further ionizing and exciting atoms in the gas. After that time, the electrons interact mainly via elastic collisions, thermalizing towards equilibrium with the steady state, background electron population. The steady state of the gas and plasma will be calculated taking the outputs of the MC model after a few ns and using them as inputs for the fluid model described in the next chapter, where the diffusion and recombination of the electrons will be simulated together with the heating of the gas.

Chapter 4

Low energy and fluid modeling

In the previous chapter we have presented a Monte Carlo model of the X-ray absorption by the gas and the evolution of the photo and Auger electrons during the first nanoseconds after the absorption of the X-ray photon flash. During that time, the electrons slow down to an energy of a few eV, so that later they interact with the gas only via elastic collisions. Calculating the steady state of the plasma generated by the attenuator using the MC model would require an impractically long computation time. Instead, the diffusion of the electrons, together with the electrochemical reactions and the heating of the gas and electrons will be calculated together with a self-consistent electric field using a fluid model, in which the spatial distribution of particles and energy densities (heat transfer) are the solutions of diffusion equations.

Fluid models considering the electron and heavy species distributions and solving the diffusion and Poisson equations have been successfully applied to a number of plasmas, including electron beam generated plasma [11], microwave plasmas [58,59], DC columns [60] and excimer and halogen lamps [61–63]. The common characteristics of these sources is that the gas pressure ranges between a few mbar up to atmospheric pressure, where the particle transport is determined or at least strongly influenced by the collisions with the gas rather than by the electromagnetic fields. Another characteristic is that the electron population may not be in thermal equilibrium with the surrounding gas. This is due to the large mass difference between the electrons and the ions and neutral atoms, which results in a very small energy transfer between both populations. On the other hand, electron-

electron collisions do thermalize the population rapidly so that the electron population usually follows a more or less Maxwellian distribution, in some cases better described with two rather than one electron temperatures [64, 65]. It is also possible that the electron population follows a different distribution, like a Druyvestein one [66], a mixed one or a more sophisticated distribution resulting from the detailed consideration of all the processes involved in a collisional-radiative model [67, 68]. In most of cases a simple distribution (Maxwell, Druyvestein or mixed) is considered a good enough approximation to reproduce the physical processes.

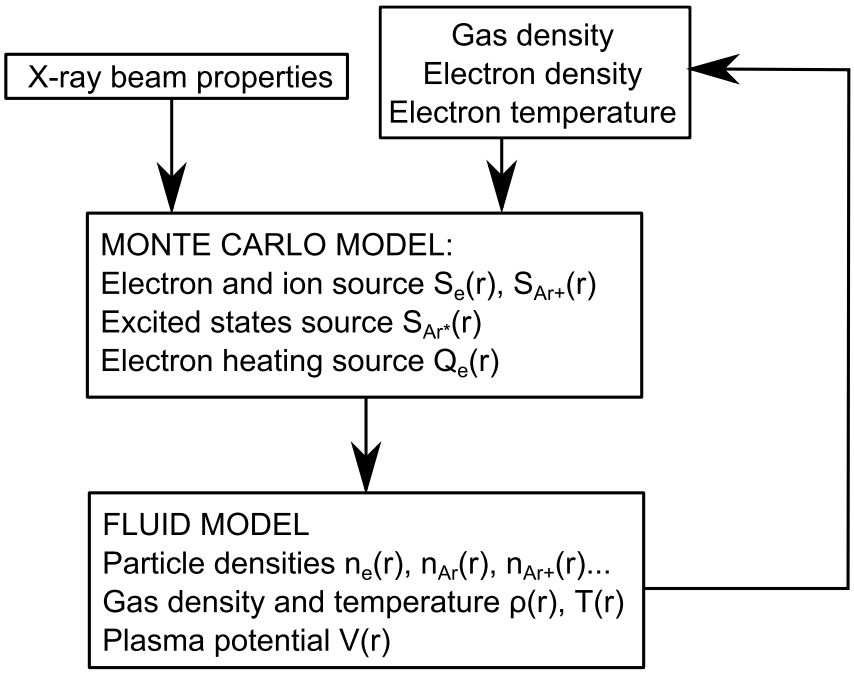

Figure 4.1: Algorithm for the coupling of the high-energy Monte Carlo model and the low energy Fluid model. The outputs of the Monte Carlo simulation are used as the source terms of the fluid simulation; the gas density and electron properties are used as inputs for the Monte Carlo in the following iteration. Convergence is reached after 4-5 iterations.

The basic algorithm of the modelling of the gas attenuator is shown in figure 4.1. The low energy model will take as input the electron spatial distribution produced by each X-ray flash, its mean energy per electron and the excited and ionized species spatial distribution, all of them given by the MC model output. Also, it will require the gas pressure and the boundary conditions on the wall of the attenuator, namely the temperature or heat transfer ratio at the boundary. The output will be the stationary-state electron, ion and excited particle densities, the electron temperature, the reaction rates, the electrical

field in the plasma and most important the gas temperature and density. To obtain complete self-consistency, the gas temperature and the electrical field are used as input in the MC model again, and hence both models are iteratively coupled. After a few iterations the distributions obtained from the fluid model do not change and the true stationary solution has been reached.

The chapter is structured as follows. In section 4.1 the chemical species included in the model are introduced, as well as the transport equations and corresponding boundary conditions. The calculation of the transport coefficients (diffusion and mobility) is explained in section 4.2. The electrochemical reactions of the model are enumerated in section 4.3. Finally, the results of the model are presented and discussed in section 4.4. In addition a study on the effect of the gas convection on the heat transfer is included in section 4.5.

4.1 Transport equations

Chemical species

The chemical species considered in the model for argon gas are electrons, neutral atoms Ar, first and second excited levels blocks Ar^s and Ar^p (treated each as an effective level), single and double charged monoatomic ions Ar^+ and Ar^{++}, diatomic and triatomic ions Ar_2^+ and Ar_3^+ and one excimer state Ar_2^*. A similar model was developed for krypton, without considering the triatomic ions which was found to play a negligible role in the argon simulations.

Conservation equations

The time dependent electron continuity equation solved for this problem can be written as

$$\begin{aligned} \frac{\partial n_e}{\partial t} + \vec{\nabla}\vec{\Gamma}_e &= R_e \\ \vec{\Gamma}_e &= -\mu_e \vec{E} n_e - D_e \vec{\nabla} n_e \end{aligned} \tag{4.1}$$

where n_e is the electron density, $\vec{\Gamma}_e$ is the electron particle flux and R_e is the source and loss term of the electrons, which includes both the input from the MC model and the gains and losses due to ionization and recombination, discussed in detail later in this chapter (section 4.3). The electron particle flux $\vec{\Gamma}_e$ contains the mobility of the electrons in the presence of the electric field $\vec{E}$ according to the mobility coefficient μ_e, and the diffusion of the electrons due to their density gradient according to the diffusion coefficient D_e. Because of the absence of externally applied magnetic fields, the transport coefficients, strictly speaking 2-dimensional tensors, can be described with a single parameter each, which multiples the unity tensor. Both transport coefficients will be obtained in section 4.2. An equivalent equation is written for the electron energy conservation:

$$\begin{aligned} \frac{\partial n_\epsilon}{\partial t} + \vec{\nabla}\vec{\Gamma}_\epsilon + \vec{E}\vec{\Gamma}_e &= Q_\epsilon \\ \vec{\Gamma}_\epsilon &= -\mu_\epsilon \vec{E} n_\epsilon - D_\epsilon \vec{\nabla} n_\epsilon \end{aligned} \tag{4.2}$$

where n_ϵ is the electron energy density, $\vec{\Gamma}_\epsilon$ is the electron energy flux and Q_ϵ is the energy gain and loss by the electron population, including the input from the MC module (in this case the kinetic energy associated to the electron population) and the energy exchanged in ionization, recombination, elastic and inelastic collisions. The additional term $\vec{E}\vec{\Gamma}_e$ on the left-hand side of the equation accounts for the Joule heating (or Ohmic heating) of the electron population in the presence of the electric field. The electron energy flux $\vec{\Gamma}_\epsilon$ is determined by the energy mobility coefficient μ_ϵ and energy diffusion coefficient D_ϵ, also obtained in section 4.2. The mean electron energy is obtained from the solution of the two equations described above, as the ratio between the electron particle density and the electron energy density: $\bar{\epsilon} = n_e/n_\epsilon$.

An identical continuity equation can be written for the transport of the heavy species (ions and neutral atoms) of the plasma

$$\begin{aligned} \frac{\partial n_X}{\partial t} + \vec{\nabla}\vec{\Gamma}_X &= R_X \\ \vec{\Gamma}_X &= -\mu_X \vec{E} n_X - D_X \vec{\nabla} n_X \end{aligned} \tag{4.3}$$

This is equivalent to the electron continuity equation where X stands for every heavy species of the model. The electrical field only affects to the charged particles, and obviously the neutral species are only affected by the diffusion and source terms. The total number of heavy species particles is determined by the gas pressure, so that if the gas pressure is known, one of the continuity equations can be dropped and replaced by the ideal gas law

$$pV = n_t RT \tag{4.4}$$

from where the density of one of the heavy species can be found:

$$n_N = n_t - \Sigma_{i=1}^{N-1} n_i \tag{4.5}$$

where n_i is the density of each of the N heavy species. Note that it is a matter of choice to solve the set of N continuity equations and later calculate the pressure as an output, or to solve a set of $N-1$ continuity equations plus the ideal gas law equation.

The corresponding equation to the electron energy density equation is the heat transfer equation. Here we assume that, due to their similar masses, the different heavy species populations exchange energy efficiently and therefore are well described by a single energy distribution, characterized by a single temperature T:

$$\rho C_p \frac{\partial T}{\partial t} - \vec{\nabla}\left(k\vec{\nabla}T\right) = Q_{gas} \tag{4.6}$$

where C_p is the heat capacity at constant pressure, k is the thermal conductivity and Q_{gas} is the heat source term, including heating by elastic collisions with electrons and heating and cooling from chemical reactions. The heat conductivity and heat capacity

were chosen as those of argon gas [69], as it was assumed that the effect of other heavy species in the heat transport would be negligible.

The electric field $\vec{E} = -\vec{\nabla}V$ is obtained via the electric potential V, which is in turn calculated solving the Poisson equation

$$\nabla^2 V = \frac{\rho_q}{\epsilon} \tag{4.7}$$

where ϵ is the electric permittivity constant of the gas and ρ_q is the charge density. Note that because there is no externally applied electrical field and no strict quasineutrality is assumed, the resulting electric field will correspond to the ambipolar electrical field, except near the attenuator wall where a sheath will develop.

Boundary conditions

The simulation domain is a 2D azimuthally symmetric slice of the attenuator; the gradients and fluxes written above are in this case function only of the radial position. The boundary conditions at the center of the domain are the same for all the equations and dictated by the symmetry of the problem: the derivative of every variable must be zero:

$$\left.\frac{\partial X}{\partial r}\right|_{r=0} = 0 \tag{4.8}$$

where X is the variable considered. As for the boundary condition in the wall of the attenuator, we will assume that any electron, ion and excited species reaching the wall will be absorbed by it, releasing all its energy and being reemitted into the gas as a neutral atom. The absence of an externally applied electric field means that the only field facing the attenuator wall is the sheath field. As it is only of a few volts (see figure 4.4c in section 4.4), the secondary electron emission induced by the ions striking the wall is negligible. The boundary condition reads then

$$X(r = R) = 0 \tag{4.9}$$

The only exception is the gas temperature at the wall, which is water-cooled and kept at a constant temperature of 300 K. The neutral gas atoms are assumed to be in thermal equilibrium with the wall, and according to the ideal gas law the neutral, ground state atoms density remains at a value of $n_{wall} = \frac{p}{RT_{wall}}$.

4.2 Transport coefficients

The transport coefficients of the electron population were calculated using the BOLSIG+ program [68], assuming a Maxwellian electron energy distribution function (eedf) and elastic collisions with neutral atoms only. The cross sections of these collisions were taken form the LXCat database [70]. This assumption keeps only if the ionization degree is small and the electron temperature low, so that the inelastic and ionization collisions are a minority. A priory, the electron energy distribution obtained as output from the MC model (figure 3.9) justifies the assumption of elastic collisions only, since the electron population above the lowest excitation energy threshold is depleted and no external electric field will increase the electron energy above that threshold. As for the assumption of collisions with neutral atoms only, it will be demonstrated a posteriori, in section 4.4 later this chapter. The resulting reduced transport coefficients (multiplied by the gas density so as to make them density independent) are shown in figure 4.2 as a function of the electron mean energy.

The transport coefficients of the heavy species were taken as proportional to the particle density only, so that the reduced transport coefficients are constant. The mobility coefficients of the charged species are shown in table 4.1. The diffusion coefficients of those species were calculated using the Einstein relation $D = \frac{\mu k_B T}{q}$. No data was found in the literature for the mobility of the Ar_3^+ ion, so it was assumed to be equal to that of Ar_2^+ [71]. The reduced diffusion coefficients for all the neutral species was taken as $3.54 \cdot 10^{18}$ $m^{-1}s^{-1}$ [72]. It was found that, due to the relatively high pressure of the studied cases, the excited species decay by radiative deexcitation and are confined to the source region, so that the precise value of the diffusion coefficient would not affect the final result.

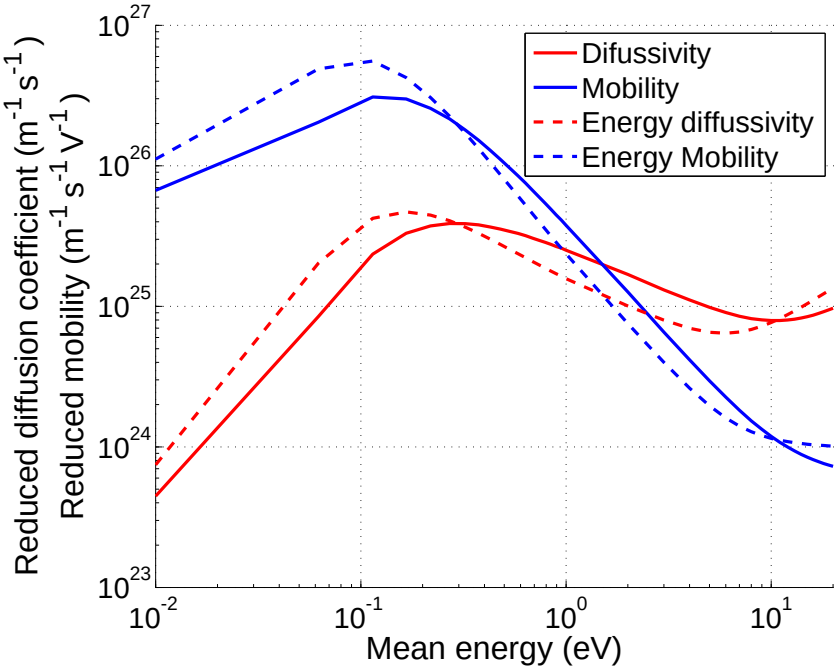

Figure 4.2: Reduced transport coefficients of a Maxwellian electron population in argon gas as a function of the mean electron energy.

Species	μN ($\mathrm{m^{-1}V^{-1}s^{-1}}$)	Ref.
Ar^+	$3.7576 \cdot 10^{19}$	[71, 73]
Ar^{++}	$7.0617 \cdot 10^{19}$	[72]
Ar_2^+	$4.4871 \cdot 10^{19}$	[71, 73]
Ar_3^+	$4.4871 \cdot 10^{19}$	Assumed as Ar_2^+

Table 4.1: Reduced mobility coefficients of the charged species simulated by the fluid model. The corresponding reduced diffusion coefficients have been calculated using the Einstein relation for charged particles: $D = \frac{\mu k_B T}{q}$.

4.3 Reactions

The reactions included in the argon gas model are shown in table 4.2. It includes electron collision cross sections, recombination of electrons via three-body processes and with diatomic and triatomic ions, conversion from atomic to molecular ions, excimer production and radiative deexcitation of excited species. An energy diagram (figure 4.3) shows the energy levels of the species considered and the main reactions between these species.

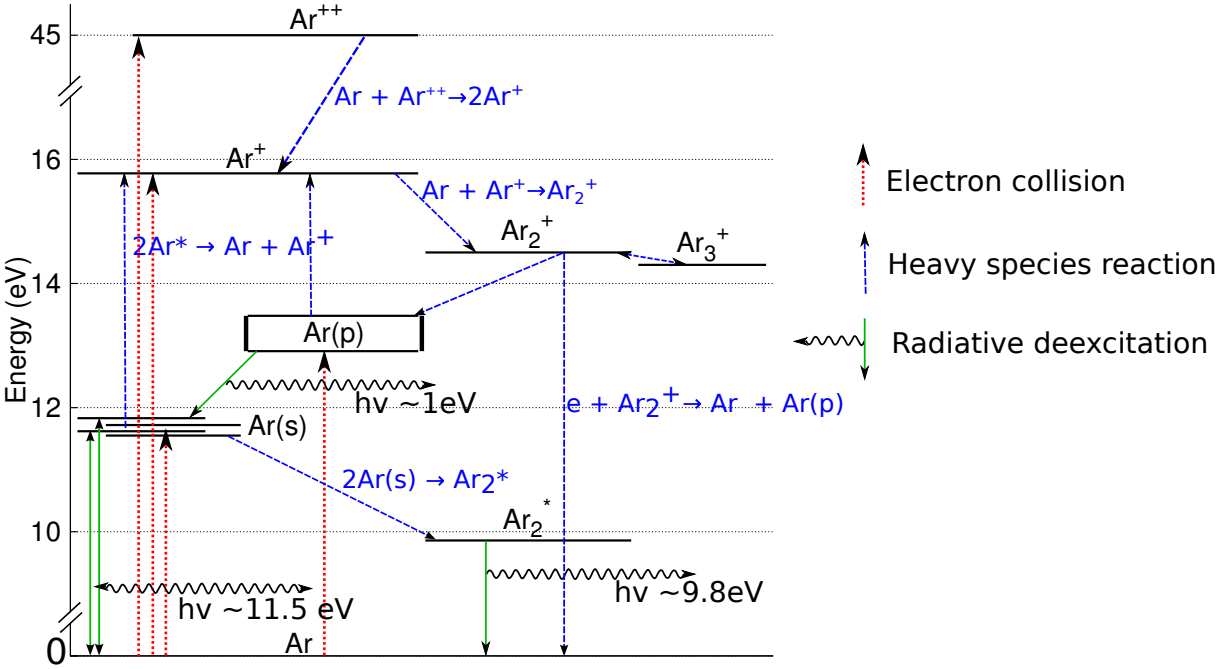

Figure 4.3: Energy levels diagram of argon and main reaction processes.

The reaction rates of the electron-impact reactions were calculated as a function of the mean electron energy by using the program BOLSIG+ and cross sections obtained for LXCat, assuming a Maxwellian eedf for the transport coefficients. The recombination reactions are not usually given with a cross section but rather as a reaction coefficient, function of gas and electron temperature [74, 75]. This temperature dependence is also found in heavy species reactions like the molecular ion formation [76]. Coefficients with gas and electron temperature dependence have been used when available to account for the effect of the thermal gradients expected in the gas.

The radiative deexcitations coefficients are of extreme importance because the power emitted in this way will reach the attenuator walls without heating neither the electrons nor the gas. The lifetime of the Ar^p effective level has been taken directly from the literature [77], as well as for the Ar_2^* excimer state [78]. However, for the Ar^s states the mixture between resonant and metastable states at high pressure requires to take into account the exchange between levels due to electron collisions and the radiation trapping of the emitted UV photons. The result is an effectively longer lifetime of the level block.

The largest possible number of reactions was included in the model in order make it as general as possible. Many reactions will play only a secondary role in the particle and energy densities and could be removed from the simulation without effect in the final result. However, this balance is only verifiable *a posteriori* and valid only for a specific set of input parameters, like range of gas pressure or of power absorption. By including a rich kinetics we expect to be able to use the same model for a wider range of working conditions.

#	Reaction	Reaction coefficient	Ref.
Electron-impact reactions (cross sections)			
1	$e + \mathrm{Ar} => e + \mathrm{Ar}$	LXCat & BOLSIG+	[68, 70]
2	$e + \mathrm{Ar} => e + \mathrm{Ar}^s$		
3	$e + \mathrm{Ar} => e + \mathrm{Ar}^p$		
4	$e + \mathrm{Ar}^s => e + \mathrm{Ar}$		
5	$e + \mathrm{Ar}^p => e + \mathrm{Ar}$		
6	$e + \mathrm{Ar} => 2e + \mathrm{Ar}^+$		
7	$e + \mathrm{Ar}^s => 2e + \mathrm{Ar}^+$		
8	$e + \mathrm{Ar}^p => 2e + \mathrm{Ar}^+$		
9	$e + \mathrm{Ar}^s => e + \mathrm{Ar}^p$		
10	$e + \mathrm{Ar}^p => e + \mathrm{Ar}^s$		
11	$e + \mathrm{Ar}_2^s => 2e + \mathrm{Ar}_2^+$	Cross section & BOLSIG+	[71, 79]
Recombination reactions			
12	$e + \mathrm{Ar}_2^+ => \mathrm{Ar} + \mathrm{Ar}^p$	$8.5 \cdot 10^{-7} \cdot (T_e(K)/300)^{-0.67} \cdot (T(K)/300)^{-0.58}\ cm^3/s$	[74]
13	$2e + \mathrm{Ar}_2^+ => e + \mathrm{Ar} + \mathrm{Ar}^p$	$5.4 \cdot 10^{-27} \cdot T_e(eV)^{-4.5}\ cm^6/s$	[75]
14	$e + \mathrm{Ar} + \mathrm{Ar}_2^+ => 2\mathrm{Ar} + \mathrm{Ar}^p$	$3.7 \cdot 10^{-29} \cdot T_e(eV)^{-1.5} \cdot T(K)^{-1}\ cm^6/s$	[75]
15	$2e + \mathrm{Ar}^+ => e + \mathrm{Ar}^p$	$5.4 \cdot 10^{-27} \cdot T_e(eV)^{-4.5}\ cm^6/s$	[75]
16	$e + \mathrm{Ar} + \mathrm{Ar}^+ => \mathrm{Ar} + \mathrm{Ar}^p$	$3.7 \cdot 10^{-29} \cdot T_e(eV)^{-1.5} \cdot T(K)^{-1}\ cm^6/s$	[75]
17	$e + \mathrm{Ar}_3^+ => 2\mathrm{Ar} + \mathrm{Ar}^p$	$1.6 \cdot 10^{-7} \cdot T_e(eV)^{-0.54}\ cm^3/s$	[11]
18	$2e + \mathrm{Ar}_3^+ => e + \mathrm{Ar} + \mathrm{Ar}_2^s$	$5.4 \cdot 10^{-27} \cdot T_e(eV)^{-4.5}\ cm^6/s$	[75]
19	$e + \mathrm{Ar} + \mathrm{Ar}_3^+ => 2\mathrm{Ar} + \mathrm{Ar}_2^s$	$3.7 \cdot 10^{-27} \cdot T_e(eV)^{-1.5} \cdot T(K)^{-1}\ cm^6/s$	[75]
Heavy species reactions			
20	$2\mathrm{Ar}^s => e + \mathrm{Ar} + \mathrm{Ar}^+$	$5 \cdot 10^{-10}\ cm^3/s$	[11]
21	$\mathrm{Ar}^s + \mathrm{Ar}^p => \mathrm{Ar} + \mathrm{Ar}^+$	$5 \cdot 10^{-10}\ cm^3/s$	[11]
22	$2\mathrm{Ar}^p => e + \mathrm{Ar} + \mathrm{Ar}^+$	$5 \cdot 10^{-10}\ cm^3/s$	[11]
23	$2\mathrm{Ar}^s => e + \mathrm{Ar}_2^+$	$5 \cdot 10^{-10}\ cm^3/s$	[11]
24	$2\mathrm{Ar} + \mathrm{Ar}^+ => \mathrm{Ar} + \mathrm{Ar}_2^+$	$9.4 \cdot 10^{-33} \cdot T(K)^{-0.27}\ cm^6/s$	[76]
25	$\mathrm{Ar}^s + \mathrm{Ar} => 2\mathrm{Ar}$	$3 \cdot 10^{-21}\ cm^3/s$	
26	$\mathrm{Ar}^p + \mathrm{Ar} => \mathrm{Ar}^s + \mathrm{Ar}$	$5 \cdot 10^{-11}\ cm^3/s$	[80]
27	$\mathrm{Ar}^p + 2\mathrm{Ar} => \mathrm{Ar}^s + 2\mathrm{Ar}$	$5 \cdot 10^{-32}\ cm^6/s$	[80]
28	$\mathrm{Ar}^s + 2\mathrm{Ar} => \mathrm{Ar}_2^s + \mathrm{Ar}$	$10^{-32}\ cm^6/s$	[11, 81]
29	$2\mathrm{Ar} + \mathrm{Ar}_2^+ => \mathrm{Ar} + \mathrm{Ar}_3^+$	$6.96 \cdot 10^{-32} \cdot (T(K)/298)^{-0.47}\ cm^6/s$	[82]
30	$\mathrm{Ar} + \mathrm{Ar}_3^+ => 2\mathrm{Ar} + \mathrm{Ar}_2^+$	$8.65 \cdot 10^{-12} \cdot (T(K)/298)^{-0.73}\ cm^3/s$	[82]
31	$\mathrm{Ar} + \mathrm{Ar}^{+2} => 2\mathrm{Ar}^+$	$4.1 \cdot 10^{-13}\ cm^3/s$	[83]
Radiative decays			
32	$\mathrm{Ar}^s => \mathrm{Ar} + h\nu$	$6.25 \cdot 10^6\ s^{-1}$	[77]
33	$\mathrm{Ar}^p => \mathrm{Ar}^s + h\nu$	$3.76 \cdot 10^8\ s^{-1}$	[77]
34	$\mathrm{Ar}_2^s => 2\mathrm{Ar} + h\nu$	$3.5 \cdot 10^5\ s^{-1}$	[78]

Table 4.2: List of reactions included in the argon fluid model.

4.4 Fluid model results

The input parameters of the results shown in this section correspond to those used in section 3.6. The output of the MC model is taken as the input of the fluid model: the spatial distribution of the electron, ion and excited species source follow the output spatial distribution of the electron population after the MC simulation time, with their respective amplitude according to the ratios in table 3.4. The source is assumed continuous instead of pulsed, which simplifies the problem allowing to reach a stationary state.

Plasma parameters

The electron and heavy particles species concentrations, plasma potential, electron and gas temperature and gas density are shown in figure 4.4. The absolute (fig. 4.4a) and relative (fig. 4.4b) particle densities are shown separately to account for the changes in the total gas density due to the temperature gradient. The dominant ion is the monoatomic ion around the axis of the attenuator, where the ionization degree is the highest, and the diatomic ion closer to the wall, where the ionization degree is smaller. The flat profile of the diatomic ion density near the center indicates that it is the neutral gas density rather than the ion density the limiting factor in the conversion from monoatomic to diatomic argon ion; otherwise the diatomic ion distribution should follow that of the monoatomic ion. The triatomic ion plays only a secondary role, with its density being below 10% of the electron density and only near the attenuator wall. The excited neutral species are only present near the attenuator axis, with virtually no presence outside this central region. The reason is that the diffusion of excited species is so small that the decay happens virtually in the same position they were created, which is mainly in the region where the X-ray is absorbed. The particle densities far from the attenuator axis (r>8 mm) are heavily affected by the source term, which comes from the Monte Carlo module, so that the oscillations arising from the small statistics in this region result in oscillations in the source term and the particle density. To avoid this problem, the source terms are strongly smoothed for r>8 mm, although this smoothing may not be necessary for lower pressure situations where the diffusion of particles increases and recombination decreases.

The plasma potential (fig. 4.4c) remains at a low value in all the volume of the attenuator, reaching a peak of ∼16 V at the center and ∼14 V before the sheath near the wall, at 17 mm from the center. This corresponds to an average electric field of 125 V/m, clearly insufficient to heat the electron population. The electron temperature is correspondingly low, with an almost constant value of ∼0.25 eV everywhere except neat the attenuator wall (fig. 4.4d). This results are in agreement with measurements of the electron temperature of pulsed UV-generated plasma at mbar pressure, where the electron population cools down to room temperature in a few microseconds [12]. The oscillations of the electron temperature in the wall sheath arise from the fast diffusion of electrons and electron energy density towards the wall; the large changes of the magnitude values in a small region makes it difficult to be accurately captured by the fluid model.

We can also compare here the validity of the assumption made taking the X-ray beam as continuous, despite their time structure. The total number of electrons created in one single flash, in the continuous mode, was $6.63 \cdot 10^{8}$ cm^{-1}, integrated in the whole 2D domain. The total number of electrons in the steady state calculated by the fluid model is $4.9 \cdot 10^{15}$ cm^{-1}, again integrated in the 2D domain. Therefore, the electrons on a single pulse are only $1.35 \cdot 10^{-7}$ of the steady-state ones. We see that the individual flashes will not impact greatly the steady state, and it is only by accumulation of many of them that the stationary state is reached. This process should be verified when using the same model for different time structures of the X-ray beam.

Finally, the gas temperature and density are shown in figure 4.4e. These are the key values required from the model, since it is the gas density what determines the degree of X-ray absorption, plasma source and gas heating. In this case, the temperature reaches more than 800 K from the initial 300 K near the wall, and the density decreases accordingly to about one third of its value near the attenuator wall.

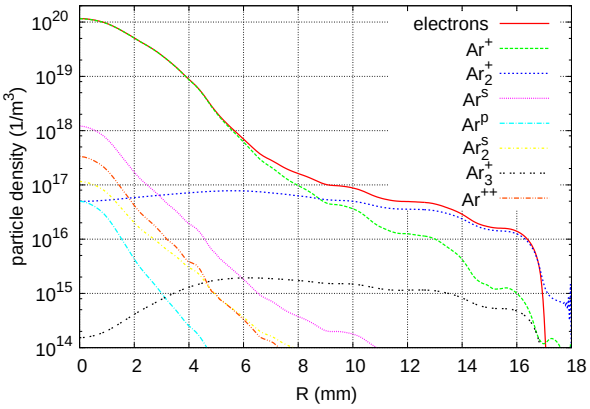

(a) Absolute particle density.

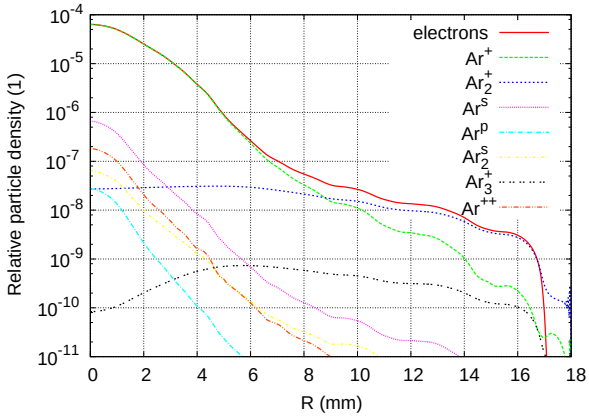

(b) Relative particle density.

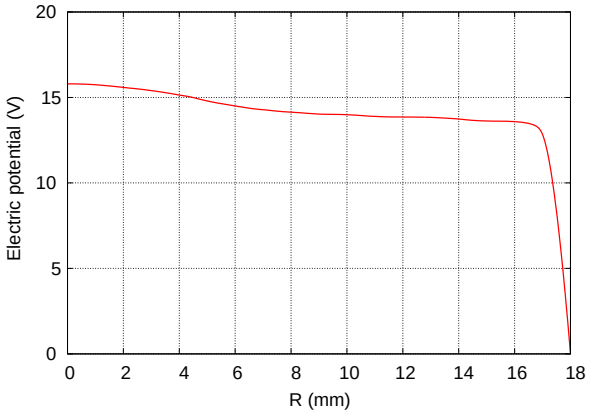

(c) Plasma potential.

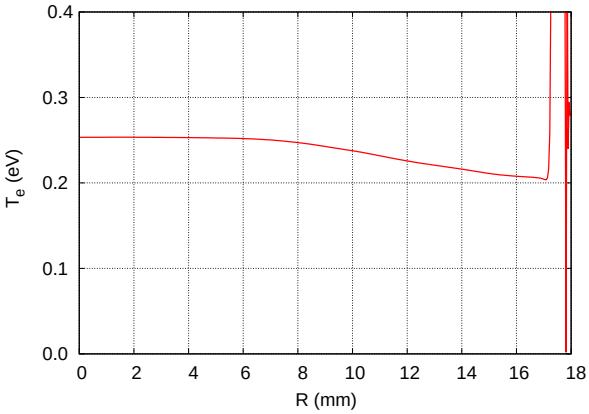

(d) Electron temperature.

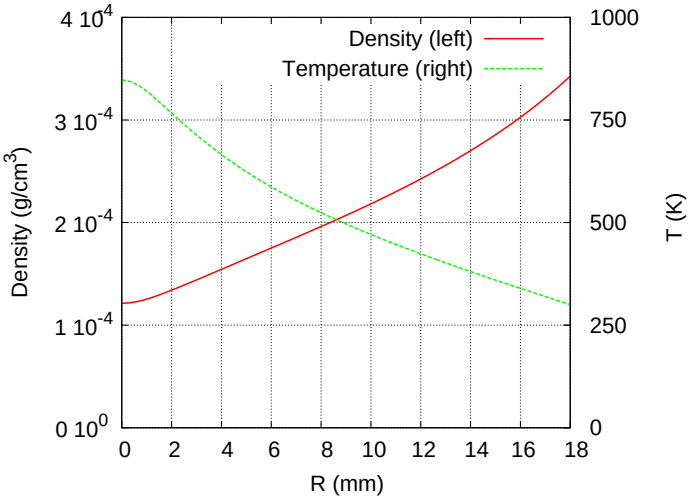

(e) Gas density and temperature.

Figure 4.4: Outputs of the plasma simulation as a function of the radial position. The absolute and relative particle numbers have been plotted separately to account for the change in the total gas density.

Power balance

The output power balance of the fluid model is detailed in table 4.3. The sum of all the power dissipation channels is not equal to the X-ray absorbed power due to the previous dissipation in the MC module of a fraction of the power via scattered and fluorescent photons. Within the low energy processes, the main power dissipation mechanisms correspond to the radiative deexcitation of excited states. This power exceeds the power carried by excited states in the output of the MC module (table 3.3); the reason is that the two body recombination of an electrons with a molecular ion results in a ground state and a excited state as output. Therefore, not only all of the input excited states decay via radiative deexcitation but also a significant fraction of those produced in the recombination. The heating of the gas accounts for most of the rest of the absorbed power, being distributed between electron elastic collisions ($\sim$2/3 of the heating power) and the heat of reaction of the heavy species ($\sim$1/3 of the heating power).

Loss mechanism	Power loss (W/cm)	Power loss fraction (%)
Ar^s radiation	1.05	62.4
Ar^p radiation	0.23	13.6
Ar_2^s radiation	0.01	0.3
Heating - electron collision	0.26	15.7
Heating - heavy species reactions	0.13	8.0
Heating - total	0.40	23.6

Table 4.3: Output power balance of the fluid simulation for 200 mbar argon gas. Input parameters given in tables 3.6 and 3.4

Of special importance is the fact that all of the power input of the plasma is dissipated either as deexcitation or as gas heating within the bulk of the plasma, with a negligible amount resulting from the recombination and ion bombardment near the wall (figure 4.5). This is due to the relatively high pressure of the gas, which prevents efficient diffusion of charged and excited particles, and to the absence of an externally applied electric field. The result is that the heating occurs in a narrow region around the X-ray beam path, determined by the size of the X-ray beam. A lower pressure would increase the particle diffusion, however in all the cases studied with this model, down to 50 mbar, the diffusion still was negligible.

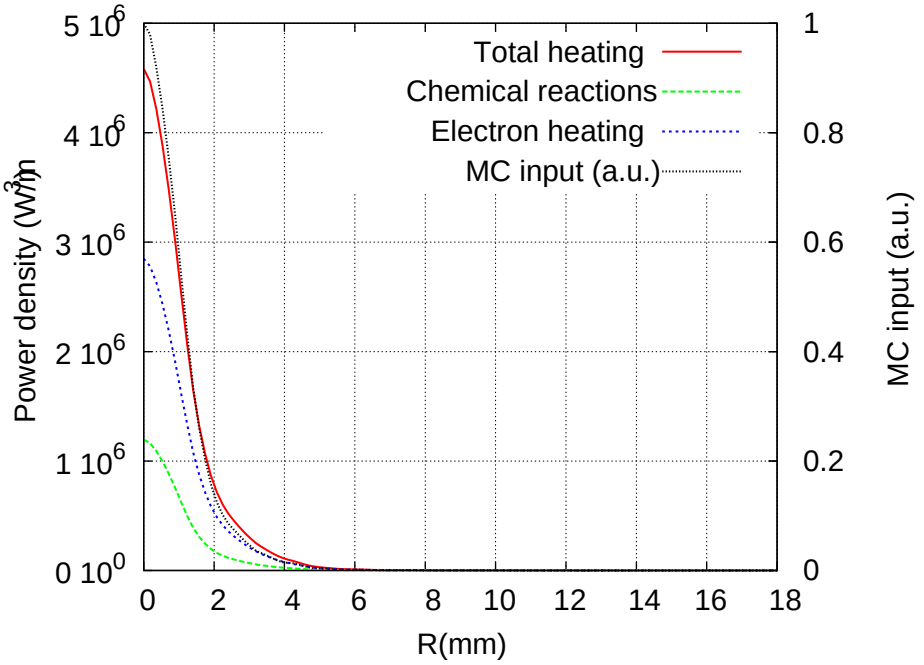

Figure 4.5: Gas heating as a function of the radial position, compared to the Monte Carlo output of the electron distribution which is in turn the source of electrons in the fluid model.

Convergence of solutions

The convergence of the fluid model was archived by using time-dependent equations and calculating the evolution until no changes in the distributions are observed. This smooths the changes in the particle distributions and makes the simulation more stable. The number of elements used in the simulations can be varied; in the example showed in this model it consisted in 200 elements. An increase in the number of elements results in a more difficult convergence, due to the orders of magnitude difference in the particle concentration between the center of the attenuator and the wall. COMSOL gives the option of solving logarithmic equations, which makes easier to treat the large density gradients at the cost of making the equations non linear. The solutions of the fluid model were found to be independent of the specific solver chosen to compute the solution. This also indicates that the large oscillations on electron temperature and density near the attenuator wall are due to the formulation of the problem and not to the solution method.

The final solution of the model reaches convergence after a few iterations. In figure 4.6 is shown the evolution of the absorbed power (4.6a), electrons generated per X-ray flash (4.6b), mean electron energy (4.6c) and ratios of heavy species (ions and excited states) to electrons (4.6d) as obtained from the Monte Carlo simulation on each iteration. The strong first oscillation comes from assuming room-temperature density as starting density, before the first loop is completed. It affects the power absorbed and the number of electrons produced in a similar way, which means that the number of electrons produced per absorbed unit of power remains fairly constant. The change in the mean electron energy are due to the changes in gas density, which affects the collision frequency and the energy loss of the electrons. The ratios of single and double charged ions and excites states to the number of electrons do not change between iterations, as expected since all the collision frequencies are proportional to the gas density, and therefore their ratios independent of it.

Conclusions

The fluid model simulations show a recombining plasma constrained by the high gas pressure to a small region around the source (X-ray beam), with the ionization degree dropping several orders of magnitude in the few millimeters between the attenuator axis and the wall. The electron temperature is extremely low ($\sim$0.25 eV), in agreement with experiments on UV-generated plasma in which the electron population thermalizes after a few microseconds [12]. A large fraction of the input power is dissipated via radiative deexcitation, with the rest being dissipated as thermal energy, heating the gas. The gas density results will be used in chapter 5 to simulate the X-ray absorption by the attenuator.

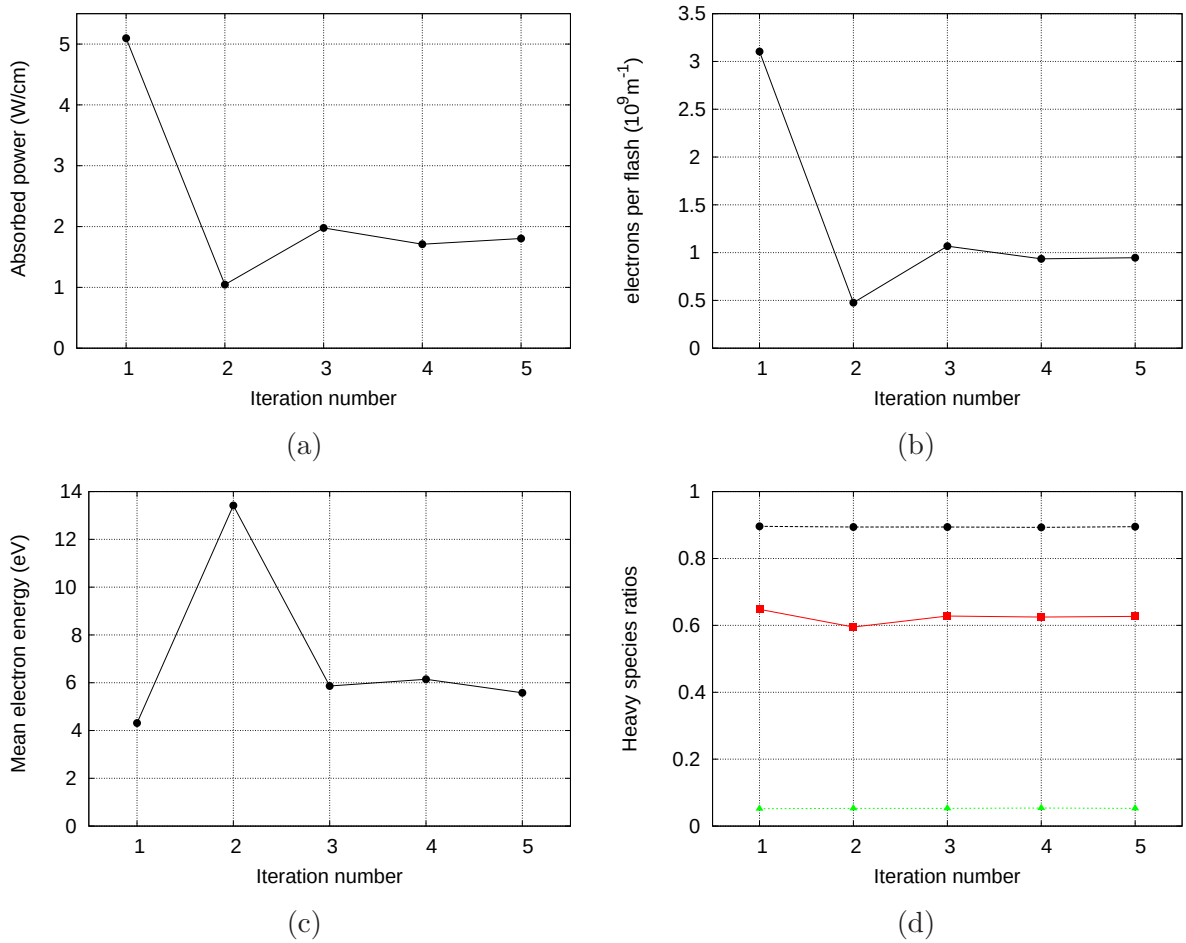

Figure 4.6: Convergence of the power absorption (a), number of electrons (b), mean electron energy (c) and heavy species to electrons ratios (d) as function of the iteration number.

4.5 Effect of gas convection

The model described before assumed that the heating of the gas would not lead to a significant fluid motion due to buoyancy, or that this motion would not affect the plasma parameters or the heat transfer. While this is usually true at pressures on the order of mbars, where the density is so low that the buoyant forces are negligible, this might not be true at a few hundreds of mbars. To verify this assumption, a model considering laminar fluid in a 2D domain with heating in the center of a disc and cooling in the walls was built. The gas properties of the model were those of krypton [69], with the results extrapolable to argon. Only the effect on the heat transfer is studied in this model. The model was implemented using COMSOL Multiphysics.

Model of gas convection

The equations solved for this model are the time-independent mass, momentum and energy continuity equations:

$$\vec{\nabla}\left(\rho\vec{u}\right) = 0 \tag{4.10}$$

$$\rho\left(\vec{u}\cdot\vec{\nabla}\vec{u}\right) = \vec{\nabla}\left(\rho I + \mu\left(\vec{\nabla}\vec{u} + \left(\vec{\nabla}\vec{u}\right)^T\right) - \frac{2}{3}\mu\left(\vec{\nabla}\vec{u}\right)I\right) + \vec{F} \tag{4.11}$$

$$\rho C_p\vec{u}\cdot\vec{\nabla}T = \vec{\nabla}\cdot\left(k\vec{\nabla}T\right) + Q \tag{4.12}$$

where ρ, $\vec{u}$ and T are the gas density, velocity and temperature, μ is the viscosity coefficient, k is the thermal conductivity, C_p is the heat capacity at constant pressure, I is the unity tensor and $\vec{F}$ and Q are the external forces and heat sources respectively. The external force is in this case the gravity force $\vec{F} = -\rho\vec{g}$, and the external heat source is the heating of the gas by the X-ray source in the center of the attenuator. Because of the symmetry of the system given by the direction of the gravity, only half a disk needs to be solved, with symmetry boundary conditions in the vertical diameter. These conditions are the zero derivative for the gas density, temperature and vertical velocity component and zero value for the horizontal velocity component:

$$\left.\frac{\partial\rho}{\partial x}\right|_{x=0} = 0 \qquad \left.\frac{\partial T}{\partial x}\right|_{x=0} = 0 \qquad \left.\frac{\partial u_y}{\partial x}\right|_{x=0} = 0 \qquad u_x(x=0) = 0 \tag{4.13}$$

where $x = 0$ is the vertical diameter of the disc. The boundary conditions in the wall of the attenuator are fixed temperature equal to that of the wall and zero gas velocity:

$$T(r=0) = T_{wall} \qquad \vec{u}(r=0) = 0 \tag{4.14}$$

The gas density in the wall is not obtained directly but via a specified gas pressure and the ideal gas law:

$$pV = nRT \tag{4.15}$$

To analyze the results of the simulation we will use two adimensional numbers: the

Nusselt number and the Rayleigh number [84]. The Rayleigh number (eq. 4.16) is the equivalent in buoyancy-driven flows to the Reynolds number in pressure-driven flows: a large Rayleigh number is associated with high velocities and turbulent flow, while a low number indicates low velocities and laminar flow [85]. It is calculated in turn as the product of two adimensional numbers: the Grashof number (ratio between buoyant and viscous forces) and the Prandtl number (ratio between viscous and thermal diffusion rates). The Nusselt number (eq. 4.17) is the ratio between the local heat transfer at the boundary of the fluid and the heat transfer between the hot and the cold boundaries assuming linear temperature gradient. This number is well-defined for planar geometries with a hot boundary opposing a cold boundary; in that situation, the value of Nu is one if there is no convection and increases as convection increases. To keep this property in our non-planar geometry, two simulations will be run for each set of initial conditions, one with the gravity force active and another one without, so that in the second case the heat transfer is only by conduction. Only two equations, corresponding to the heat transfer by conduction (eq. 4.19) and to the mass conservation (eq. 4.10) need to be solved in this case. Also, because of the non-planar geometry, the Nusselt number value changes along the position of the wall; we will use the averaged Nusselt number (eq. 4.18) rather than the local value. The ratio between the Nusselt numbers of both cases is then taken as the "effective" Nusselt number, which will be close to one if convection does not play a role and will increase and convection increases.

$$Ra = Pr \cdot Gr = \frac{C_p}{\mu} k \frac{g\rho_0^2 (t_h - T_c) L^3}{T_0 \mu_0^2} \tag{4.16}$$

$$Nu = \frac{L}{k_0 (T_h - T_c)} k \left. \frac{\partial T(r)}{\partial r} \right|_{wall} \tag{4.17}$$

$$\overline{Nu} = \frac{1}{L} \int_L Nu(R) dR \tag{4.18}$$

$$-\frac{1}{r} \frac{\partial}{\partial r} \left(r \cdot k(T) \frac{\partial T}{\partial r} \right) = Q(r) \tag{4.19}$$

Simulation results

The simulation was run for input powers between 1 and 700 W/m and pressures between 50 and 500 mbar. In all the cases the wall temperature was fixed and equal to 300 K. Two samples of the resulting temperature and velocity profiles are shown in figure 4.7, corresponding to the cases of 200 mbar with 100 W input power and 400 mbar with 20 W input power. At low pressure and at high power input, we find that the temperature distribution is almost radially symmetric (fig. 4.7a), with the gas velocity distribution not affecting the temperature and being almost symmetric to the horizontal axis (fig. 4.7b). Only when the gas pressure is high and the power input not too high the effect of gas convection appears. Figures 4.7c and 4.7d show the temperature and velocity distributions obtained for a pressure of 400 mbar and a power input of 20 W. Here the temperature distribution appears distorted by the gas movement, with the hot area displaced upwards and the eddy on the velocity distribution also displaced upwards from the position at lower pressure.

The relation between the Rayleigh and the Nusselt numbers of the simulated cases is shown in figure 4.8, with the points linked by common pressure (fig. 4.8b) and by common power (4.8a) to facilitate the interpretation. For a given input power, at low pressure (50 mbar) the Nusselt number remains as one and the Rayleigh number stays low: the heat transfer is made mainly by conduction (fig 4.8a). As the pressure increases, the density and therefore the density gradient increases, and so does the buoyancy force. The result is that at higher pressure the heat transfer by convection increases. If we take a fixed gas pressure, at low input power the heat transfer is also made mainly by conduction, and as the power increases so does the effect of convection and the Nusselt and Rayleigh numbers. However, after a certain input power value, a rather unintuitive behaviour appears: both Nusselt and Rayleigh numbers decrease, which means the heat transfer by convection *decreases* as we increase the power input further. This can be explained taking into account that while the buoyancy force and the density gradients are bounded by the

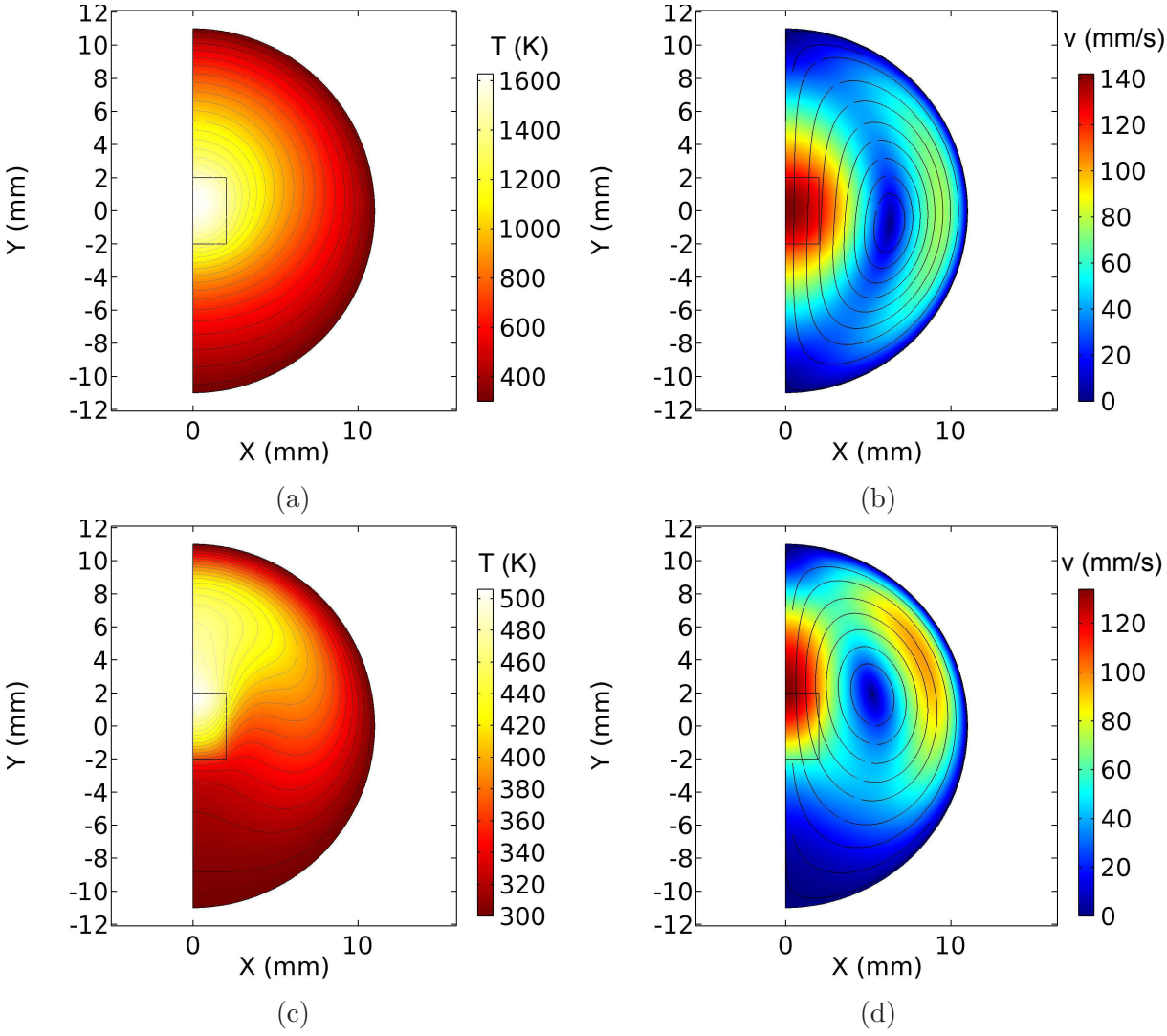

Figure 4.7: Temperature and velocity distributions from the heat transfer simulations, for 200 mbar of pressure and 100 W input power (a and b) and 400 mbar and 20 W (c and d). The solid lines represent isothermal curves in the temperature plots and streamlines in the velocity plots. The color legend represents the intensity of temperature and velocity respectively.

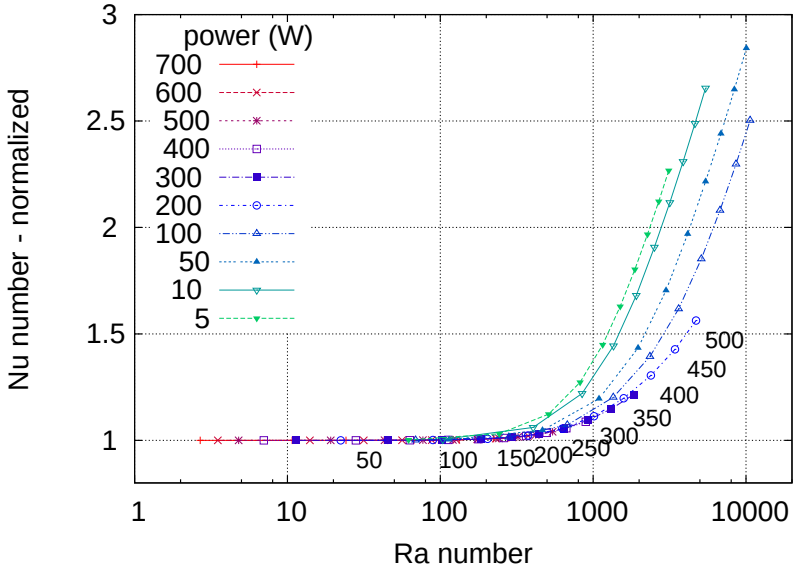

(a)

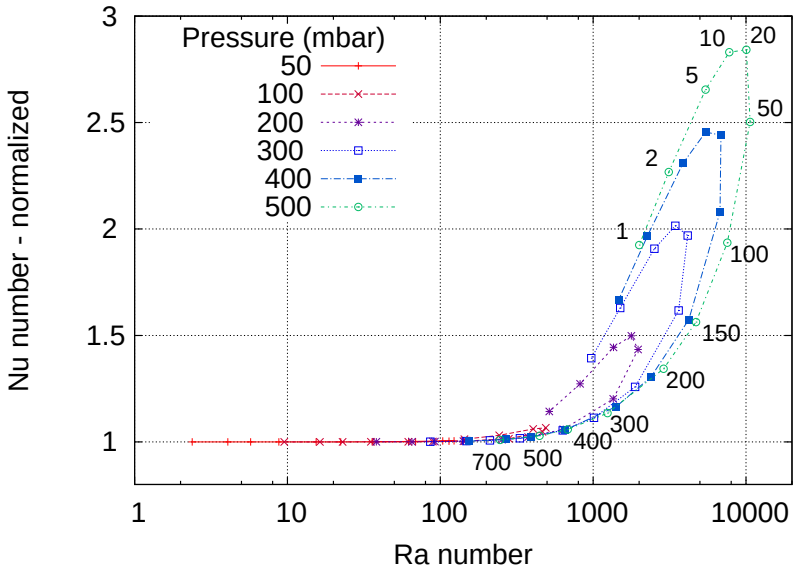

(b)

Figure 4.8: Nusselt vs. Rayleigh numbers of the gas flow inside a 12-mm radius gas attenuator filled with krypton gas. Both plots presents the same simulated points, in the first case linked by common heating power and with varying gas pressure, and in the second linked by common gas pressure and with varying heating power.

maximum gas density, the temperature gradient can increase indefinitely:

$$\rho = \frac{p}{RT} \quad \rightarrow \quad \Delta\rho = \frac{p}{R}\left(\frac{1}{T_h} - \frac{1}{T_c}\right) \qquad \text{if } T_h \rightarrow \infty \text{ then } \Delta\rho \rightarrow \frac{p}{RT_c} \tag{4.20}$$

The final result is that for high (>50 W) and low (<10 W) heat power input, the gas convection can be neglected in the range of pressure at which the gas attenuator operates (50-500 mbar) and might play a non-negligible role for an intermediate power input values and the upper end of the operation scale. This result applies only for laminar flow, which is the one expected since the Rayleigh number obtained ($< 10^5$) is lower than the expected for the onset of the turbulence, starting around Ra$\sim 10^9$ [85].

Chapter 5

Comparison between model and experimental results

In chapters 3 and 4 we have presented a hybrid model combining Monte Carlo and fluid modeling to obtain the gas density and plasma parameters on a 2D slice of the gas attenuator. To be able to compare the results of the simulation with the experimental ones, we need to go from the 2D simulation results to the 3D simulation of the attenuator. The difficulty is that the X-ray beam is attenuated during its trajectory through the attenuator, so that different 2D slices receive not only different power input but also a different X-ray spectrum, because the absorption is not uniform in the whole spectrum. In addition, the gas density is not know *a priori* but only from the simulations; this would require to simulate every single slice of attenuator one by one, using the previous ones to calculate the X-ray absorption. In this chapter we present a method to simulate the 3D attenuator from the 2D models which does not require the exhaustive simulation of the whole length of the attenuator. The results thus obtained will be compared with the experimental measurements from chapter 2.

5.1 Pseudo-3D model algorithm

To obtain the incoming X-ray spectrum arriving to a 2D slice at a distance z, we use the Beer-Lambert law for each energy component

$$I_{in,z}(E) = I_0(E) \exp\left(-\sigma(E) \int_0^z \rho(z) dz\right) \tag{5.1}$$

where I_0 is the spectrum at the entrance of the attenuator, $I_{in,z}$ the spectrum at the z position and $\rho(z)$ the gas density along the attenuator. One can notice that the X-ray absorption depends not directly on the gas density but on the integral along the line of sight, this is, the areal density in m^{-2}. Therefore, one can calculate a distance within the attenuator z_0 with a density ρ_0 (not necessarily the average of $\rho(z)$) which has the same incoming spectrum as a point at a distance z with the real gas density:

$$\int_0^z \rho(z) dz = \rho_0 z_0 \tag{5.2}$$

This result will be used to simulate the absorption of the 3D attenuator. The process is graphically shown in figure 5.1. First, a number of simulations assuming room-temperature density and an initial given set of distances (for instance, 0, 5, 10, 20 and 50 cm) is calculated, with the incoming spectrum on each case attenuated according to the distance and room-temperature density. All the simulations have in common the gas pressure, the radius of the gas chamber and the initial X-ray spectrum. Then, the density of the simulated points is used to recalculate the real position of the points, assuming the gas density between them can be approximated as a linear interpolation between the simulated points. Once the real position of all the simulated slices has been determined, it is possible to calculate the absorption at any given length by integrating the interpolated density profile.

When simulating the total power absorption by this method, one must take into account that, depending on the X-ray spectrum and gas pressure, steep gradients may

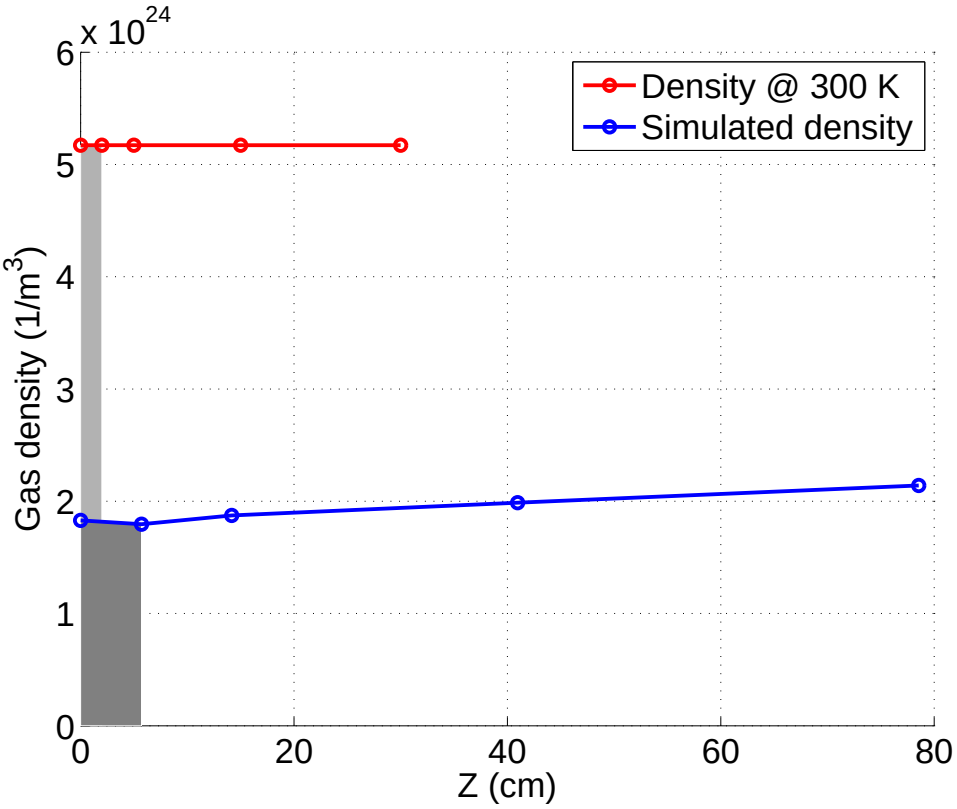

Figure 5.1: Position of the simulated 1-cm slices assuming constant, room-temperature density (red) and interpolating the simulation density (blue). The grey areas have equal size, therefore providing the same X-ray absorption before the second simulated point. The simulation parameters were 200 mbar of argon gas, 18 mm of attenuator radius and X-ray spectrum corresponding to a U18 undulator with 2x2 mm^2 beamsize.

appear in the frontal side of the attenuator, where the X-ray intensity and the absorption is higher. If after recalculating the positions of the discs this is the case, the solution would be to simulate extra positions in the region where the gradient is steeper.

5.2 Model results and comparison with experimental data

Electron density profiles

While the simulation of a sufficient number of slices is necessary to obtain an accurate profile of the gas density, it might be possible to avoid in a given simulated slice the repe-

tition of some steps taken in a previous slice. In particular, the eedf and the spatial profile of the electron distribution as obtained by the MC model for one slice may be reusable for other slices. Figure 5.2 shows the electron eedf and projected spatial distributions for all the points simulated for 200 mbar of argon, as sown in figure 5.1. The results on the distributions are normalized by the total number of electrons generated, so that the changes in the total absorbed power and therefore on the total number of electrons are not reflected here. The resulting profiles are found to be very similar, with the differences from the average value being less than 10% in the energy range from 0 to 12 eV and in the radial range from 0 to 2.5 mm, which covers most of the electron distribution in energy and spatial dimensions. It would possible therefore to use a single Monte Carlo simulation to calculate the slow down of the electrons, and then to use the same profile renormalized to the local X-ray absorption for different positions.

Power absorption

The proposed model was applied to the experimental conditions described in chapter 2, in particular to the cases with 200 mbar of initial pressure. The length of the attenuator was taken as 50.8 cm and the radius as 18 mm. The effect of the 4-ways crosses was not considered in this case, and the attenuator was simulated as a single cylinder with no ports on the sides. The results of the total absorbed power and of the error relative to the measured absorbed power are shown in figure 5.3. The error bars in the experimental power absorption correspond to 10% of its total value. The simulated power absorption was found to be lower than the experimentally measured one, with a difference between 10 and 20% of the absorbed power. A lower power absorption than measured means an average gas density also lower than in reality, and therefore a higher gas temperature. The outcome is that the gas is heated more efficiently in the simulation than in reality, or that the cooling is less efficient. Possible sources of this additional cooling may come from the windows of the attenuator, which are water cooled and that may absorb part of the heat generated in the gas immediately next to them. Also, if some turbulence or instability is present in the gas but has not been taken into account, it could lead to a more efficient energy transfer to the walls and to a reduction of the gas temperature,

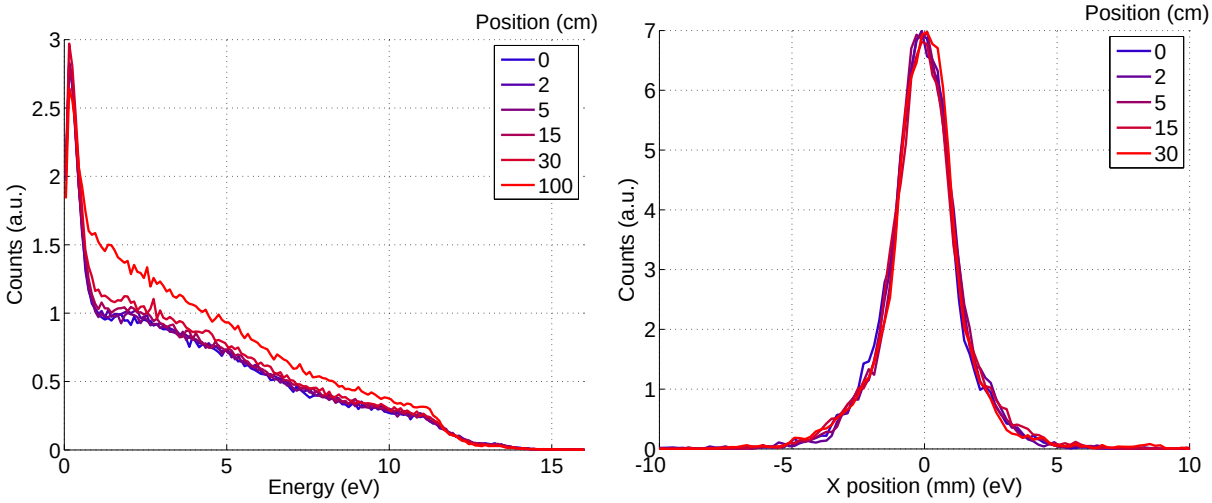

(a)

(b)

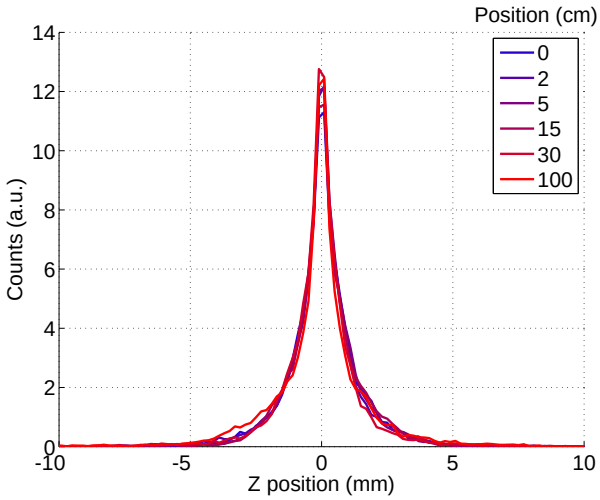

(c)

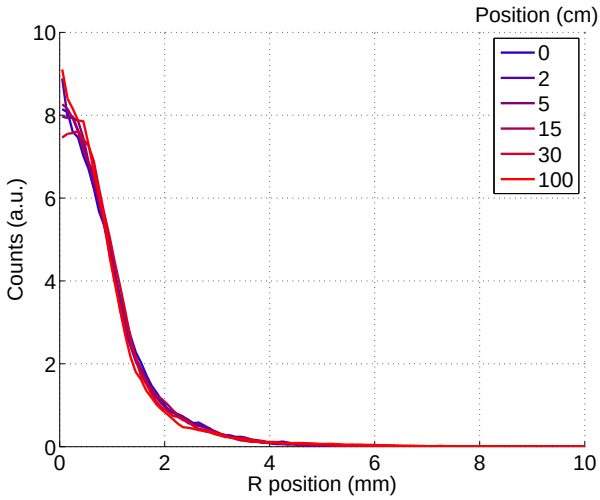

(d)

Figure 5.2: Electron population at the end of the MC simulations for 200 mbar of argon after as a function of the electron energy (a), projected X position (within the simulation plane), b), projected Z position (out of the simulation plane), c) and projected radial position (d).

therefore increasing the absorption. The behavior of the electron population could also affect greatly the heating of the gas, since more than half of the heating comes from electron collision reactions. If the eedf is not Maxwellian as assumed, the reaction rates, the collisional heating and the electron diffusion could change significantly enough to account for the error in the current simulation.

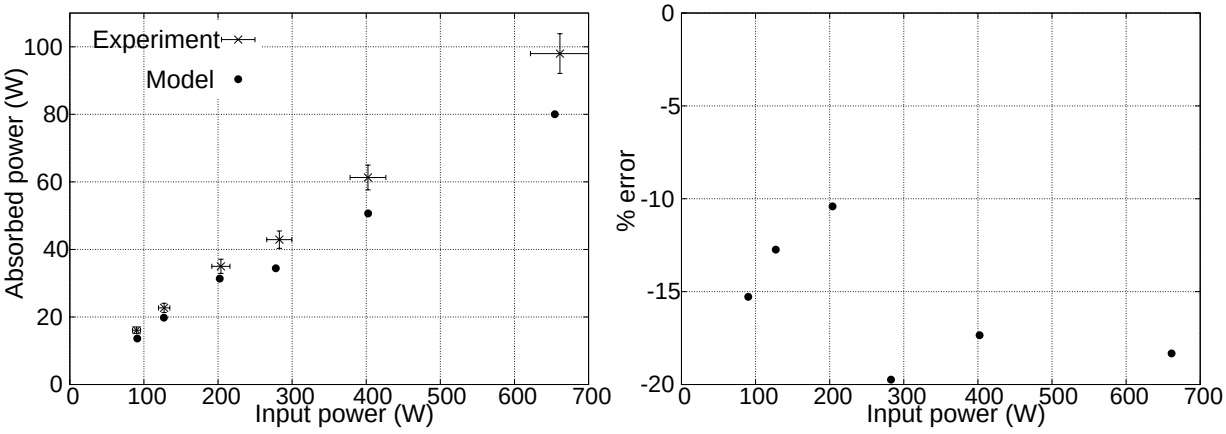

(a) (b)

Figure 5.3: Comparison of power absorption measured and predicted by the model (a) and relative error of the model prediction (b) for 200 mbar argon gas, under a U18 undulator source at different gaps and beam sizes.

Excited states density profiles

Another quantity which can be compared between the experiments and the model is the excited states density profile. The absolute value of the metastable density was found to be very different, with a difference of around one order of magnitude lower in the model. This value, however, is not a good magnitude to compare because assumptions on the proportion of the four 1s states within the block population could change its lifetime in the model, affecting significantly the number density without changing the heat transfer of the radial profile. Also, the 1s and 2p excited states were found to have the same profile in the model, so both OES and TLAS measurements are compared simultaneously here.

Figure 5.4 shows the excited state profiles obtained with OES and TLAS together with the simulated profile. The OES profile correspond to that obtained with 100 torr argon gas (133 mbar) while the TLAS and simulated profile correspond to that obtained

with 200 mbar of argon. All the cases shown here share the same X-ray source, a U18 undulator with 6 mm gap and a beam size of 2x2 mm^2. While both OES and TLAS profiles are very similar, they show a somewhat broader distribution than the simulated one, and especially a more important density far from the X-ray beam irradiated area. This characteristic is common to all the cases studied, which indicates that a mechanisms exciting the neutral atoms of the gas has not been taken into account in the model. A possible mechanism is the interaction of fluorescent and scattered X-rays within the gas; however, they carry a very small fraction of the power and their interaction probability before reaching the walls is small, so that it is unlikely that this is the cause. A more likely reason is a longer range of the fast electrons, so that the region in which they excite and ionize atoms before thermalizing is larger than simulated. Finally, a different eedf could increase the temperature and the diffusion of cold electrons, therefore increasing the excitation ratios by the cold electron population.

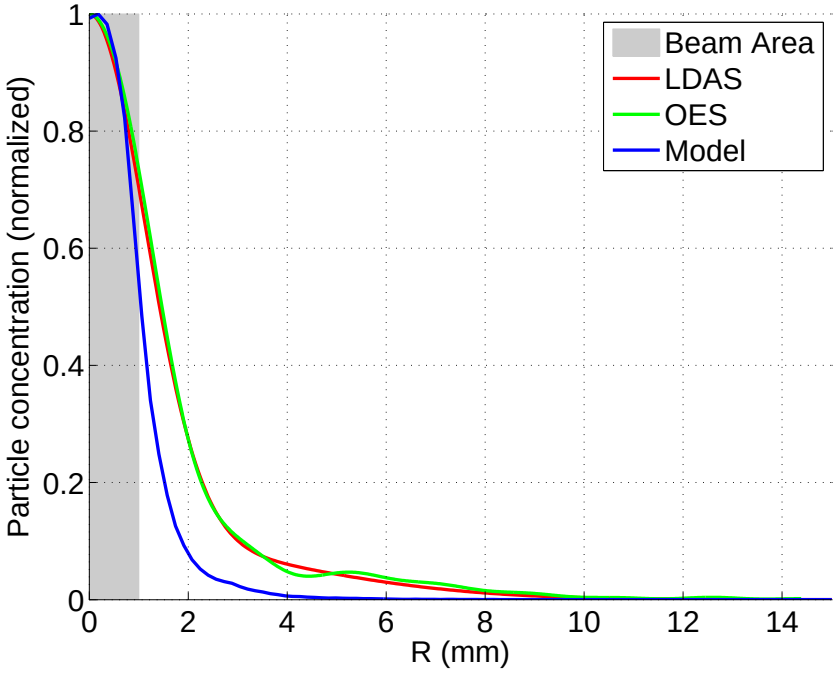

Figure 5.4: OES profile, TLAS profile and simulated excited states profiles for 200 mbar argon, an X-ray source from a U18 undulator at 6 mm and a beam size of 2x2 mm. The profiled have been normalized to their respective maximum values.

Discussion

The 3D model of the attenuator reproduces the trend on the power absorption obtained by the experimental measurements, although the values of the absorbed power are systematically between 10 and 20% lower than experimental. This indicates either a cooling mechanism not taken into account or an overestimation of the gas heating. Possible cooling mechanisms are related to turbulent phenomena, either by movement of the fluid or by dynamical instabilities in the plasma properties. A reduced heating could come from a non-maxwellian eedf increasing the diffusion and reducing the efficiency of the heat transfer to the gas, or from a heavy-species reaction coefficient not set to the real value. Finally, the cooling of the gas in contact with the windows of the attenuator could become efficient enough to reduce the gas temperature in this region and increase the X-ray absorption.

The spatial profile of the excited species obtained in the model also follow the trend of the experimental measurement, with a sharp peak around the X-ray beam path and a quick decrease in density outside this region. The experimental profile is actually broader than the simulated one, indicating that either the actual diffusion of excited species is larger than expected, or that the fast electrons exciting and ionizing the gas travel a longer distance within the gas before thermalizing than in the MC model.

A possible simplification on the model could be based in the fact that, if the axial density gradient is not too steep, the MC modeling of different slices results in the same eedf and spatial electron distributions, which could be used to simplify the simulation or even in taking this result to a true 3D fluid simulation, in which the MC part would model only a reduced number of slices would be requires to obtain the radial distributions, which would be the scaled according to the local X-ray absorption. This 3D modeling would include the effect of the attenuator windows and would allow for more complex geometries to be simulated.

Chapter 6

Conclusions and outlook

A study on a high power X-ray gas attenuator has been carried out, analyzing the plasma processes within the gas both experimentally and theoretically. This is the first time to our knowledge that plasma processes have been considered for an X-ray gas attenuator and indeed one of the few detailed studies beyond the measurement of the X-ray absorption for commissioning.

The experimental study included the measurement of the excited species distribution by OES (Optical Emission Spectroscopy) and TLAS (Tunable Laser Absorption Spectroscopy), together with the power absorption from the X-ray beam as described in chapter 2. The excited species distribution showed a plasma confined to the surroundings of the X-ray beam, due to the relatively high pressure, between 50 and 500 mbar, that prevented diffusion, and to the absence of an externally applied electric field. The size of the region with high concentration depended only on the cross section of the X-ray beam, not on the gas pressure or power absorbed. This means that, even at the lowest operating pressure, the fast electrons produced via photoionization and Auger decay slow down to thermal energy within a distance smaller than the beam cross section. Both Ar(4s) and Ar(4p) excited state levels, measured by TLAS and OES respectively, showed the same spatial distribution.

The measurement of the power absorption showed that the higher is the power of the X-ray beam, the lower is the fraction of the power absorbed by the attenuator. The reason

is that as the absorbed power increases, so does the temperature of the gas around the beam path. The result is a decrease in density and therefore in the power absorption. The gas temperature on the X-ray beam path, calculated from the X-ray absorption, resulted to be as high as 850 K for an absorbed power of 87 W.

An hybrid model of the gas attenuator combining a Monte Carlo model and a fluid model was also developed. The Monte Carlo model, described in chapter 3, simulated the X-ray absorption, ion deexcitation and fast electron thermalization, giving as outputs the slowed-down electron population together with the number of ions and excited species created. According to this model, the fast electrons created after the X-ray absorption thermalize within a few nanoseconds in a region only slightly larger (1-2 mm larger radius) than the X-ray beam cross section. This electron population is taken as input by the fluid model described in chapter 4, which solved the diffusion and recombination of ions and electrons, the decay of excited species and the heating of the gas. The resulting plasma was also confined around the X-ray beam, recombining in the bulk of the gas with the diatomic ion of argon, Ar_2^+. The plasma potential was found to be low ($\sim$15 V) due to the absence of externally applied electric fields. The electron temperature was also found to be rather low, around 0.2 to 0.3 eV, in agreement with other studies in plasmas created by EUV laser pulses. The gas temperature and density also exhibited large gradients, with the temperature being as high as 850 K for 182 W of absorbed power and the density around 1/3 of that next to the cooled walls. The effect of the gas flow on the heat transfer was also studied. Both Rayleigh and Nusselt number were found to be small, so that no turbulence is expected and the gas convection can be neglected in a first approximation.

The hybrid model was able to reproduce the increase of the absorbed power with the input power, with an error of between 10 and 20% of lower absorption than in the experiment for the studied cases, as shown in chapter 5. Also, it was able to reproduce the confinement of the excited species due to the high pressure, with the excited species profile being somewhat narrower in the model than in the experiment. Overall, the model has been able to reproduce correctly the type of plasma present in the gas attenuator, with the small differences coming possibly from the necessary simplifications made regarding

the eedf or the geometry of the system. In particular, the temperature obtained in the model was lower than in the experiment, which means that the heating of the gas might be overestimated, the cooling underestimated, or both. An possible reason may be a non-maxwellian electron distribution with a different mean energy than the calculated one. This would affect both the collisional heating of the gas and the recombination ratio, two important factors both dependent on the electron population properties. Also, a higher diffusion could increase the cooling efficiency and account for the difference on the excited states profile. Finally, dynamical turbulence or instabilities in the gas and plasma would enhance the heat transfer towards the walls, reducing the gas temperature and increasing the density and power absorption. This work has focused on the stationary state and properties of the plasma; a dynamical measurement of its properties could provide an insight on additional cooling mechanisms.

Implications for gas attenuators

The model developed in this thesis can be applied directly to existing gas attenuators to predict the absorption for current and future working conditions, enabling a more efficient operation by reducing the commissioning time determining the power absorption and transmission of the attenuator. It can be also applied to the design of future attenuators, by simulating different designs and helping to determine which one will be better adapted to the given physical and technological constrains. This includes not only attenuators for synchrotron beamlines but also attenuators for X-ray free electron lasers, in which the time-averaged emitted power has a similar value. In this case, the model should be modified to take into account the different time structure of these sources, with more intense X-ray pulses separated by longer dark times, but the essential physical processes would remain the same.

6.1 Outlook

In the first place, the model and algorithm developed in this thesis could be transformed in an user-friendly application with the possibility of predicting the power absorption of a beamline, allowing the user to increase the photon flux at the useful energy while keeping the total power taken by the optical elements under control. Such an application would have to reconsider the way in which the transition from the 2D simulations to the 3D is performed, in order to obtain the results in a reasonable computing time. Possible changes are the use of a single Monte Carlo simulation of the electron slow-down for several slices or the use of a 3D fluid model using COMSOL Multiphysics.

Possible future studies in the attenuator plasma should be directed towards deeper understanding of the electron population properties and its impact on the gas heating. From the modelling side, considering different electron energy distribution functions, like a Druyvestein distribution or one obtained from a collisional-radiative model would show the impact of the different distributions on the final power absorption. From the experimental side, the measurement of the electron density and temperature would provide a validation of the model, or a indication on what distribution should be used. Some techniques that measure directly the population properties are Thompson scattering or microwave cavity resonance spectroscopy. Other techniques like Langmuir probe measurements or microwave interferometry may not be adapted to this kind of plasma. For the Langmuir probe, the pressure exceeds that of the standard theory, the presence of ionizing radiation might affect the probe measurements and the gradients might be larger than the probe size, making difficult the interpretation of data. For the microwave interferometry, the small size of the plasma and large gradients might induce diffraction of the wavefront, so that the transmission results cannot be attributed only to the phase shift and absorption, making the interpretation and analysis difficult.

An indirect method of measuring the electron properties would be to obtain the density of all the four 1s states, whose relative densities are in equilibrium with the electron temperature, provided that the electron density is high enough. Another indirect method

would be the dynamical measurement of the excited states, either via OES or TLAS, which would show the creation of theses states when the X-ray beam is turned on or its decay when turned off. Especially during the decay, this would allow to determine the fraction of excited states coming from direct electron excitation, which will decay rapidly, and the fraction coming from dielectronic recombination, with a probably longer apparent lifetime. Dynamical studies might also be relevant for the operation modes with longer times between X-ray flashes, like the ESRF 16-bunch mode in which the flashes are separated by 284 ns (3.52 MHz) or the standard XFEL mode with 37 μs of separation (27 kHz). In this case, the inter-pulse heat dissipation will change the gas density when the following pulse arrives, as opposed to that obtained from a quasi-continuous irradiation.

In any case, the current study and the developed model could be used as a starting point for further research on the gas attenuator physics. Also, the model can be used in the design on future attenuators, to obtain a first approximation on the final power absorption for the different expected operation modes.

Bibliography

[1] J.-l. Revol, et al. *ESRF Upgrade Phase II Status*. Ipac2013, pages 1140–1142, 2013.

[2] M. Borland, V. Sajaev, and Y. Sun. *Hybrid seven-bend-achromat lattice for the advanced photon source upgrade*. Ipac2015, 2015.

[3] J. Baruchel, J. L. Hodeau, M. S. Lehmann, J. R. Regnard, and C. Schlenker, editors. *Neutron And Synchrotron Radiation For Condensed Matter Studies, Volume I: Theory, Instruments And Methods*. Springer and Les Editions de Physique, Berlin and Les Ulis, 1993.

[4] A. C. Thompson and D. Vaughan, editors. *X-ray Data Booklet*. Lawrence Berkeley National Laboratory, University of California, second edition, January 2001.

[5] H. Requardt, et al. *A new gas attenuator system for the ID17 biomedical beamline at the ESRF*. J. Phys. Conf. Ser., **425**(2):022002, mar 2013.

[6] A. Chumakov, et al. *Performance of a cryogenic silicon monochromator under extreme heat load*. J. Synchrotron Radiat., **11**(2):132–141, mar 2004.

[7] L. Zhang, et al. *Thermal deformation of cryogenically cooled silicon crystals under intense X-ray beams: measurement and finite-element predictions of the surface shape*. J. Synchrotron Radiat., **20**(4):567–580, jul 2013.

[8] Y. Feng, et al. *Filamentation effect in a gas attenuator for high-repetition-rate X-ray FELs*. J. Synchrotron Radiat., **23**(1):21–28, jan 2016.

[9] C. F. Hernández. *Study of a gas absorber for synchrotron's light*. master thesis, ETSII Madrid - Grenoble INP, 2010.

[10] D. D. Ryutov, et al. *The physics of the gas attenuator for the linac coherent light source, lcls-tn-09-5*. Technical report.

[11] E. Elson and M. Rokni. *An investigation of the secondary electron kinetics and energy distribution in electron-beam-irradiated argon*. J. Phys. D. Appl. Phys., **29**(3):716–725, mar 1996.

[12] J. Beckers, R. M. van der Horst, E. A. Osorio, G. M. W. Kroesen, and V. Y. Banine. *Thermalization of electrons in decaying extreme ultraviolet photons induced low pressure argon plasma*. Plasma Sources Sci. Technol., **25**(3):035010, jun 2016.

[13] C. Aragón and J. A. Aguilera. *Characterization of laser induced plasmas by optical emission spectroscopy: A review of experiments and methods.* Spectrochim. Acta - Part B At. Spectrosc., **63**(9):893–916, 2008.

[14] T. Belmonte, C. Noël, T. Gries, J. Martin, and G. Henrion. *Theoretical background of optical emission spectroscopy for analysis of atmospheric pressure plasmas.* Plasma Sources Sci. Technol., **24**(6):064003, dec 2015.

[15] R. Álvarez, A. Rodero, and M. Quintero. *An Abel inversion method for radially resolved measurements in the axial injection torch.* Spectrochim. Acta Part B At. Spectrosc., **57**(11):1665–1680, nov 2002.

[16] S. Hübner, N. Sadeghi, E. A. D. Carbone, and J. J. A. M. Van Der Mullen. *Density of atoms in Ar*(3p54s) states and gas temperatures in an argon surfatron plasma measured by tunable laser spectroscopy.* J. Appl. Phys., **113**(14), 2013.

[17] E. A. D. Carbone, S. Hübner, J. J. a. M. van der Mullen, G. M. W. Kroesen, and N. Sadeghi. *Determination of electron-impact transfer rate coefficients between argon $1s_2$ and $1s_3$ states by laser pump–probe technique.* J. Phys. D. Appl. Phys., **46**(41):415202, oct 2013.

[18] L. Latrasse, N. Sadeghi, a. Lacoste, a. Bès, and J. Pelletier. *Characterization of high density matrix microwave argon plasmas by laser absorption and electric probe diagnostics.* J. Phys. D. Appl. Phys., **40**(17):5177–5186, 2007.

[19] J. M. de Regt, R. D. Tas, and J. A. M. van der Mullen. *A diode laser absorption study on a 100 MHz argon ICP.* J. Phys. D. Appl. Phys., **29**(9):2404, 1996.

[20] J. Jonkers, J. V. Dijk, and J. a. M. V. D. Mullen. *Absorption measurements on a low-pressure inductively coupled argon/mercury discharge for lighting purposes: 2. Electron density and temperature.* J. Phys. D. Appl. Phys., **32**(8):898–905, 1999.

[21] R. J. Leiweke and B. N. Ganguly. *Diode laser spectroscopic measurements of gas temperature in a pulsed dielectric barrier discharge using collisional broadening and shift of $1s_3$-$2p_2$ and $1s_5$-$2p_7$ argon transitions.* J. Appl. Phys., **113**:143302, 2013.

[22] O. Chubar and P. Elleaume. *Accurate and efficient computation of synchrotron radiation in the near field region.* proc. EPAC98 Conf., pages 1177–1179, 1998.

[23] J. C. Biasci, B. Plan, and L. Zhang. *Design and performance of ESRF high-power undulator front-end components.* J. Synchrotron Radiat., **9**(1):44–46, dec 2001.

[24] R. Stevens and J. Boerio-Goates. *Heat capacity of copper on the ITS-90 temperature scale using adiabatic calorimetry.* J. Chem. Thermodyn., **36**(10):857–863, oct 2004.

[25] E. Saloman, J. Hubbell, and J. Scofield. *X-ray attenuation cross sections for energies 100 eV to 100 keV and elements Z = 1 to Z = 92.* At. Data Nucl. Data Tables, **38**(1):1–196, jan 1988.

[26] A. Sáinz, et al. *Abel Inversion Applied to a Small Set of Emission Data from a Microwave Plasma.* Appl. Spectrosc., **60**(3):229–236, mar 2006.

[27] G. Pretzier. *A New Method for Numerical Abel-Inversion.* Zeitschrift für Naturforsch. A, **46**(7):639–641, jan 1991.

[28] J. Palomares, et al. *Thomson scattering on argon surfatron plasmas at intermediate pressures: Axial profiles of the electron temperature and electron density.* Spectrochim. Acta Part B At. Spectrosc., **65**(3):225–233, mar 2010.

[29] N. Konjevic, A. Lesage, J. R. Fuhr, and W. L. Wiese. *Experimental Stark Widths and Shifts for Spectral Lines of Neutral and Ionized Atoms (A Critical Review of Selected Data for the Period 1989 Through 2000).* J. Phys. Chem. Ref. Data, **31**(3):819, sep 2002.

[30] J. F. Ziegler. *Stopping of energetic light ions in elemental matter.* J. Appl. Phys., **85**(3):1249, 1999.

[31] S. Agostinelli, et al. *Geant4—a simulation toolkit.* Nucl. Instruments Methods Phys. Res. Sect. A Accel. Spectrometers, Detect. Assoc. Equip., **506**(3):250–303, jul 2003.

[32] J. Allison, et al. *Geant4 developments and applications.* IEEE Trans. Nucl. Sci., **53**(1):270–278, feb 2006.

[33] J. Sempau, E. Acosta, J. Baro, J. Fernández-Varea, and F. Salvat. *An algorithm for Monte Carlo simulation of coupled electron-photon transport.* Nucl. Instruments Methods Phys. Res. Sect. B Beam Interact. with Mater. Atoms, **132**(3):377–390, nov 1997.

[34] J. Sempau, J. Fernández-Varea, E. Acosta, and F. Salvat. *Experimental benchmarks of the Monte Carlo code penelope.* Nucl. Instruments Methods Phys. Res. Sect. B Beam Interact. with Mater. Atoms, **207**(2):107–123, jun 2003.

[35] E. Secco and M. Sánchez del Río. *Monte Carlo simulations of scattered power from irradiated optical elements.* volume 8141, page 81410Z. sep 2011. ISBN 9780819487513.

[36] I. Cornelius, et al. *Benchmarking and validation of a Geant4–SHADOW Monte Carlo simulation for dose calculations in microbeam radiation therapy.* J. Synchrotron Radiat., **21**(3):518–528, may 2014.

[37] J. P. Verboncoeur. *Particle simulation of plasmas: review and advances.* Plasma Phys. Control. Fusion, **47**(5A):A231–A260, may 2005.

[38] V. Vahedi and M. Surendra. *A Monte Carlo collision model for the particle-in-cell method: applications to argon and oxygen discharges.* Comput. Phys. Commun., **87**(1-2):179–198, may 1995.

[39] T. Minea, C. Costin, A. Revel, D. Lundin, and L. Caillault. *Kinetics of plasma species and their ionization in short-HiPIMS by particle modeling.* Surf. Coatings Technol., **255**:52–61, sep 2014.

[40] M. H. L. van der Velden, W. J. M. Brok, J. J. A. M. van der Mullen, W. J. Goedheer, and V. Banine. *Particle-in-cell Monte Carlo simulations of an extreme ultraviolet radiation driven plasma.* Phys. Rev. E, **73**(3):036406, mar 2006.

[41] D. E. Cullen, J. H. Hubbell, and L. Kissel. *The Evaluated Photon Data Library.* Technical report, Lawrence Livermore National Laboratory, 1997.

[42] M. Gavrila. *Relativistic K-Shell Photoeffect.* Phys. Rev., **113**(2):514–526, jan 1959.

[43] J. Levin, et al. *Argon-Photoion-Auger-Electron Coincidence Measurements following K-Shell Excitation by Synchrotron Radiation.* Phys. Rev. Lett., **65**(8):988, 1990.

[44] D. P. Almeida, A. C. F. Santos, M. G. P. Homem, A. N. de Brito, and G. G. B. de Souza. *Multiple photoionization of Ar in the K-edge region: New results.* J. Electron Spectros. Relat. Phenomena, **155**(1-3):109–112, 2007.

[45] M. O. Krause. *Atomic radiative and radiationless yields for K and L shells.* J. Phys. Chem. Ref. Data, **8**(2):307, 1979.

[46] S. T. Perkins, et al. *Tables and graphs of atomic subshell and relaxation data derived from the LLNL Evaluated Atomic Data Library (EADL), Z=1-100.* Technical report, Lawrence Livermore National Laboratory, 1991.

[47] T. A. Carlson, W. E. Hunt, and M. O. Krause. *Relative Abundances of Ions Foriried as the Result of Inner-Shell Vacancies in Atoms.* Phys. Rev., **151**, 1966.

[48] A. H. Abdullah, A. M. El-Shemi, and A. A. Ghoneim. *Yields of multiply charged ions produced from inner-shell ionization in neutral Ne, Ar and Kr atoms.* Radiat. Phys. Chem., **68**(5):697–705, 2003.

[49] M. Drescher, et al. *Time-resolved atomic inner-shell spectroscopy.* Nature, **419**(6909):803–807, oct 2002.

[50] S. Perkins, D. Cullen, and S. Seltzer. *Tables and graphs of electron-interaction cross sections from 10 eV to 100 GeV derived from the LLNL Evaluated Electron Data Library (EEDL), Z = 1–100.* Technical report, Lawrence Livermore National Laboratory (LLNL), Livermore, CA, nov 1991.

[51] M. C. Bordage, et al. *Comparisons of sets of electron–neutral scattering cross sections and swarm parameters in noble gases: III. Krypton and xenon.* J. Phys. D. Appl. Phys., **46**(33):334003, aug 2013.

[52] A. Kobayashi, G. Fujiki, A. Okaji, and T. Masuoka. *Ionization cross section ratios of rare-gas atoms (Ne, Ar, Kr and Xe) by electron impact from threshold to 1 keV.* J. Phys. B At. Mol. Opt. Phys., **35**(9):307, may 2002.

[53] M. Surendra, D. B. Graves, and G. M. Jellum. *Self-consistent model of a direct-current glow discharge: Treatment of fast electrons.* Phys. Rev. A, **41**(2):1112–1125, jan 1990.

[54] C. B. Opal, W. K. Peterson, and E. C. Beaty. *Measurements of Secondary-Electron Spectra Produced by Electron Impact Ionization of a Number of Simple Gases.* J. Chem. Phys., **55**(8):4100, 1971.

[55] T. Takizuka and H. Abe. *A binary collision model for plasma simulation with a particle code.* J. Comput. Phys., **25**(3):205–219, nov 1977.

[56] M. A. Hussein, G. A. Emmert, N. Hershkowitz, and R. Claude Woods. *Effect of collisions on ion dynamics in electron-cyclotron-resonance plasmas.* J. Appl. Phys., **72**(5):1720, 1992.

[57] T. Hori, M. Kogano, M. D. Bowden, K. Uchino, and K. Muraoka. *A study of electron energy distributions in an inductively coupled plasma by laser Thomson scattering.* J. Appl. Phys., **83**(4):1909, 1998.

[58] R. L. Kinder and M. J. Kushner. *Consequences of mode structure on plasma properties in electron cyclotron resonance sources.* J. Vac. Sci. Technol. A Vacuum, Surfaces, Film., **17**(5):2421, 1999.

[59] G. J. M. Hagelaar, K. Makasheva, L. Garrigues, and J.-P. Boeuf. *Modelling of a dipolar microwave plasma sustained by electron cyclotron resonance.* J. Phys. D. Appl. Phys., **42**(19):194019, oct 2009.

[60] T. Farouk, B. Farouk, D. Staack, A. Gutsol, and A. Fridman. *Simulation of dc atmospheric pressure argon micro glow-discharge.* Plasma Sources Sci. Technol., **15**(4):676–688, 2006.

[61] G. N. Zvereva, M. I. Lomaev, D. V. Rybka, and V. F. Tarasenko. *Possible application of a volume avalanche discharge initiated by an electron beam for designing a krypton dimer laser.* Opt. Spectrosc., **102**(1):30–37, jan 2007.

[62] M. H. R. Hutchinson. *Excimers and excimer lasers.* Appl. Phys., **21**(2):95–114, feb 1980.

[63] S. Bendella, B. Larouci, and A. Belasri. *Modeling of Kr-Xe discharge of excimer lamp.* EPJ Web Conf., **44**:04004, mar 2013.

[64] T. E. Sheridan. *Observation of two-temperature electrons in a sputtering magnetron plasma.* J. Vac. Sci. Technol. A Vacuum, Surfaces, Film., **9**(3):688, may 1991.

[65] J. Mostaghimi, P. Proulx, and M. I. Boulos. *A two-temperature model of the inductively coupled rf plasma.* J. Appl. Phys., **61**(5):1753, 1987.

[66] N. Laidani, R. Bartali, P. Tosi, and M. Anderle. *Argon–hydrogen rf plasma study for carbon film deposition.* J. Phys. D. Appl. Phys., **37**(18):2593–2606, sep 2004.

[67] G. J. M. . G. . HAGELAAR. *MODELLING METHODS FOR LOW-TEMPERATURE PLASMAS.* Hdr edition.

[68] G. J. M. Hagelaar and L. C. Pitchford. *Solving the Boltzmann equation to obtain electron transport coefficients and rate coefficients for fluid models.* Plasma Sources Sci. Technol., **14**(14):722–733, 2005.

[69] E. Bich, J. Millat, and E. Vogel. *The viscosity and thermal conductivity of pure monatomic gases from their normal boiling point up to 5000 K in the limit of zero density and at 0.101325 MPa.* J. Phys. Chem. Ref. Data, **19**(6):1289, 1990.

[70] *Biagi-v8.9 database, www.lxcat.net, retrieved on July 1, 2015.*

[71] G. M. Petrov and C. M. Ferreira. *Numerical modelling of Ar glow discharge at intermediate and high pressures.* pages 1–30, aug 2013.

[72] A. Bogaerts and R. Gijbels. *Role of Ar^{2+} and Ar_2^+ ions in a direct current argon glow discharge: A numerical description.* J. Appl. Phys., **86**(8):4124, 1999.

[73] W. McDaniel and E. Mason. *The mobility and diffusion of ions in gases.* Wiley series in plasma physics. Wiley, 1973. ISBN 9780471583875.

[74] F. J. Mehr and M. A. Biondi. *Electron-temperature dependence of electron-ion recombination in Argon.* Phys. Rev., **176**(1):322–326, 1968.

[75] L. M. Biberman, V. S. Vorob'ev, and I. T. Iakubov. *Kinetics of nonequilibrium lowtemperature plasma.* Plenum Publishing Corporation New York, 1987.

[76] C. J. Chen. *Temperature Dependence of Dissociative Recombination and Molecular-Ion Formation in He, Ne, and Ar Plasmas.* Phys. Rev., **177**(1):245–254, jan 1969.

[77] W. Wiese and G. Martin. *Wavelengths and transition probabilities for atoms and atomic ions: Part 2. transition probabilities.* Wavelengths and transition probabilities for atoms and atomic ions: Part 2. Transition probabilities, NSRDS-NBS Vol. 68., **1**, 1980.

[78] S. Neeser, T. Kunz, and H. Langhoff. *A kinetic model for the formation of excimers.* J. Phys. D. Appl. Phys., **30**:1489–1498, 1997.

[79] L. Vriens and A. H. M. Smeets. *Cross-section and rate formulas for electron-impact ionization, excitation, deexcitation, and total depopulation of excited atoms.* Phys. Rev. A, **22**(3):940–951, sep 1980.

[80] R. S. F. Chang and D. W. Setser. *Radiative lifetimes and two-body deactivation rate constants for Ar(3p5, 4p) and Ar(3p5,4p') states.* J. Chem. Phys., **69**(9):3885, 1978.

[81] T. Oka, M. Kogoma, M. Imamura, S. Arai, and T. Watanabe. *Energy transfer of argon excited diatomic molecules.* J. Chem. Phys., **70**(7):3384, 1979.

[82] D. L. Turner and D. C. Conway. *Study of the $2Ar+Ar_2^+=Ar+Ar_3^+$ reaction.* J. Chem. Phys., **71**(4):1899, 1979.

[83] F. Howorka. *Thermal rate constant for $Ar^{++}+Ar \rightarrow 2Ar^+$.* J. Chem. Phys., **67**(6):2919, 1977.

[84] W. M. Rohsenow, J. P. Hartnett, and E. N. Ganic. *Handbook of heat transfer fundamentals (2nd edition).* 1985.

[85] R. Henkes, F. Van Der Vlugt, and C. Hoogendoorn. *Natural-convection flow in a square cavity calculated with low-Reynolds-number turbulence models.* Int. J. Heat Mass Transf., **34**(2):377–388, feb 1991.

Résume en français

Introduction

Le faisceau X généré par un synchrotron à haute énergie comme l'ESRF porte une grande quantité de puissance, dans l'ordre de centaines de watts par millimètre carré et une puissance totale de plusieurs kW. Cette puissance est distribué dans une spectre qui couvre plusieurs keV, les détails du spectre dépendant de la source de rayons X de chaque ligne de lumière. Dans presque toute ligne, le faisceau X initial est monochromatisé par un monochromateur à cristal double (DCM par ses sigles en anglais), qui transmettre une seule énergie (ou longueur d'onde) de le spectre incident, absorbant ou dispersant le reste. Par raison de la faible bande passante du DCM, dans l'ordre de 10^{-4}, virtuellement tout la puissance est absorbé ou dispersé dans la surface du première cristal. Cet puissance est dissipé comme chaleur, donc la température du cristal dans la empreinte du faisceau X augmente et conduite à l'expansion thermique de la surface du cristal, en la déformant. Systèmes de refroidissement spécialement dessinés, basés sur l'utilisation d'azote liquide, peuvent réduire les déformations dessous un certain limite de la puissance incidente; dessus cet valeur les déformations apparaîtront.

Il y a deux stratégies pour réduire la puissance incidente sans réduire la transmission à l'énergie d'opération. La première c'est utiliser un miroir de rayons X, qui fonctionne en réflexion total externe à faible angle. Par raison de la dépendance en énergie de l'index de réfraction, seulement la partie de baisse énergie du spectre serait réfléchi. Le miroir se comporte donc comme une filtre passe-bas. La deuxième c'est utiliser un atténuateur, qui est basé dans l'absorption des photons X qui traversent n'importe le matériel. Par raison de la dépendance du coefficient d'absorption, les photons de plus basse énergie seront

absorbés plus efficacement que ceux de plus haute énergie. L'atténuateur se comporte donc comme une filtre passe-haut. Traditionnellement, atténuateurs d'état solide ont été utilisés, consistent en un bloc de matériel situé dans le parcours du faisceau. Néanmoins, ils ont un nombre de désavantages, comme un taux d'absorption fixé par l'épaisseur du bloc et un limite dans la puissance absorbé maximale, en dessus lequel ils peuvent dépasser la température de fusion. A plus récent alternative c'est les atténuateurs à gaz, consistent en un vaisseau cylindrique avec le gaz que absorbera le faisceau X. Les avantages de ces atténuateurs sont un taux d'absorption ajustable en changeant la pression donc la densité du gaz, une besoin de refroidissement limités aux parois du vaisseau et l'absence de stresses mécaniques dans la substance d'absorption. Toutefois, le chauffage du gaz suite à l'absorption du faisceau X crée gradients de température et densité le long du parcours du faisceau, changeant le taux d'absorption par rapport a celui prévue a partir de la densité initial. Peu études on été faites dans atténuateurs à gaz, et aucun d'eux a étudié le plasma qui peut apparaitre suite a l'ionisation du gaz par le faisceau X, ni a crée un modèle auto-consistent de l'absorption en incluant processus plasma. Ces sont précisément les objectifs de cet thèse: créer un modèle de l'absorption du faisceau X et son validation expérimental, incluant des mesures de quelques propriétés du plasma.

Études expérimentaux

Le principal objectif des études expérimentaux c'est mesurer l'absorption des rayons X par l'atténuateur. Deux techniques redondants ont été utilisés: calorimétrie et transmission de faisceau X à une énergie sélectionné par le DCM. La calorimétrie mesure la puissance incidente et transmis pas l'atténuateur; la différence c'est la puissance absorbé. La transmission de faisceau X mesure l'intensité à une énergie avec et sans gaz dans l'atténuateur; la densité moyenne du gaz peut être calculé en inversant la loi de Beer-Lambert. Comme la densité du gaz détermine l'absorption du faisceau X, la puissance totale peut être calculé si le spectre incident est connu. Ces techniques ont été utilisés sur un atténuateur a gaz avec de l'argon ou du krypton, à pressions entre 10 et 550 mbar. Les résultats des deux techniques étaient effectivement consistantes entre eux. Les résultats ont montré une ab-

sorption plus importante pour krypton que pour argon, un augmentation de l'absorption avec la densité du gaz et un diminution de la densité du gaz dans le parcours du faisceau X quand la puissance incidente augmente. Les résultats seront utilisés pour valider le modèle théorique de l'absorption.

Deux techniques optiques ont été utilisés pour mesurer la distribution spatial des états excités du gaz: spectroscopie d'émission optique (OES par ses sigles en anglais) et spectroscopie d'absorption à laser accordable (TLAS par ses sigles en anglais). La OES mesures l'émission spontanée des états excités, dans notre cas des transitions 2p→1s de argon et de krypton, avec une longueur d'onde entre 700 et 1000 nm. La TLAS mesures l'absorption d'une laser de diode par une transition entre deux niveaux d'un atome. Dans notre cas on a utilisé la transition à 772.38 nm entre les niveaux $1s_5$ et $2p_7$ d'argon. Tous les deux OES et TLAS ont scannée le profil des états excités en perpendiculaire à la direction du faisceau X. Les résultats des deux techniques ont été identiques, montrant un région central avec haute concentration des états excités. La taille de cet région ne dépende pas de la pression du gaz ou de la puissance du faisceau X, mais seulement de la taille du faisceau. Ça indique que le plasma générée par l'absorption du faisceau X est confiné autour du parcours du faisceau, et que la diffusion des particules chargés et excités reste très faible.

Modèle haute énergie

Le principal défi pour construire un modèle de l'absorption des rayons X c'est prendre en compte tous les processus concernés, qui ont une énergie caractéristique entre les keV la l'absorption X et les meV du transfert de chaleur. Il n'y a aucun technique de modélisation qui prends en compte tous ces processus efficacement. La stratégie choisi a été séparer le modèle en deux parties: un modèle à haute énergie qui simule l'absorption du faisceau X et le refroidissement des électrons, et un modèle fluide qui simule la diffusion et recombinaison des particules chargés, l'émission de lumière par les états excités, et le transfert de chaleur. Le modèle global itère entre les deux modèles jusqu'à arriver à une solution

convergente.

Le première pas du modèle à haute énergie est l'absorption des rayons X par le gaz. Le principal mécanisme d'absorption est la photoionisation, dans laquelle un photon est totalement absorbé par une atome et une électron est éjecté, laissant une vacante dans une couche électronique interne. L'ion résultante est dans un état très excité, ce qui provoque l'émission des électrons Auger et photons fluorescentes. L'absorption X et la deexcitation des ions sont calculés a partir de sections efficaces et ratios de décroissance connues. La population électronique résultante a une énergie dans l'ordre de keV. Elle interactionne avec le gaz de l'environnement, excitant et ionisant atomes dans sont parcours et perdant de l'énergie dans les processus. L'ionisation et excitation du gaz a été calculé avec une modèle Monte Carlo, dans laquelle l'histoire d'un nombre des électrons est simulé en détail. La simulation s'arrête après un temps de quelques ns, quand l'énergie des électrons est dessous l'énergie d'excitation. Après cet moment les électrons seulement diffuse vers les parois de l'atténuateur sans exciter ou ioniser le gaz. Les résultats du modèle à haute énergie montrent que le refroidissement a lieu autour de faisceau X, donc les électrons ne diffuse pas trop loin du parcours de rayons X pendant cet refroidissement. Les outputs du modèle ont le nombre d'électrons, ions et états excités et ses distributions énergétiques et spatiaux. Ces outputs seront utilisés comme données d'entrée par le modèle fluide.

Modèle fluide

Le modèle à baisse énergie simules la diffusion et recombinaison des ions et électrons, l'émission de lumière depuis les états excités et le transfert de chaleur dans le gaz. Il utilises le logiciel COMSOL Multipysics pour résoudre les équations de transport de chaque espèce chimique considéré, l'équation de transport d'énergie des électrons, l'équation de chaleur et l'équation de Poisson pour le champ électrique. Le domaine de la simulation était 1D avec symétrie azimutale. Les conditions limites étaient dérivative nulle dans l'axe de symétrie pour toutes les variables et zero concentration de particules dans la paroi de l'atténuateur, zero potentiel électrique et température fixe. Les coefficients de transport

et les taux de collision ont été calculés utilisant sections efficaces de LXCat et le logiciel BOLSIG+, en supposant un distribution d'énergie des électrons maxwellienne. Les taux de recombinaison et des réactions entre espèces lourdes ont été pris de valeurs publiés, avec des dépendances des températures électroniques et du gaz. Les résultats de la simulation ont montré un plasma confiné autour du faisceau X, avec très peu de diffusion vers les parois de l'atténuateur. Ils ont montré aussi une température électronique baisse (∼0.2-0.3 eV) et un potentiel plasma faible (∼15-18 V), tous les deux conséquence de l'absence d'un champ électrique externe. Finalement, le modèle a calculé les profils de température et densité du gaz, qui peuvent être utilisés pour calculer l'absorption totale du faisceau X et comparer les résultats avec ceux obtenus dans l'expérience.

Comparaison

Pour comparer les résultats de la simulation avec eux de l'expérience, on doit arriver a une simulation 3D de l'atténuateur à partir des résultats en 1D. On fait ça en simulant un nombre de domaines 1D à différents positions supposés le long de l'atténuateur. La densité du gaz obtenu dans ces simulations et utilisé pour recalculer la position réel de chaque domaine, en interpolant la densité entre eux. Ça permettre simuler complètement l'atténuateur avec seulement quelques simulations 1D. La densité du gaz dans le parcours du faisceau est intégré dans la simulation et utilisé pour calculer l'atténuation du faisceau X. La comparaison avec les cas expérimentaux montre un accord dans la tendance de l'absorption avec les changement de puissance incidente, avec un puissance totale absorbé entre 10-20% plus bas dans la simulation que dans l'expérience.

Le profil spatiale des états excités du gaz peut être aussi comparé. Tous les deux simulation et expérience ont montré un plasma confiné autour le faisceau X. La taille la région centrale de haute concentration dépendait seulement de la taille du faisceau et pas de la pression du gaz ou de la puissance du faisceau. Dans la simulation la taille du région centrale était légèrement plus petite que dans l'expérience, indiquant que la diffusion est plus rapide dans la réalité.

Conclusions

Un étude dans un atténuateur à gaz de rayons X de haute puissance a été réalisé, analysant le plasma processus dans le gaz théoriquement et expérimentalement. Ceci est la première fois à notre connaissance que plasma processus ont été considérées pour un atténuateur à rayons X. Les expériences et la modélisation ont montré un plasma confiné autour du faisceau X. Le modèle a montré aussi un plasma avec faible potentiel électrique et température électronique baisse, conséquence de l'absence d'un champ électrique externe. La puissance absorbé prédit par le modèle était 10-20% plus baisse que dans l'expérience, indiquant que quelques processus de dissipation de l'énergie ont été sous-estimés ou négligés.

Le modèle crée ici peut être utilisé comme point de partie dans futures études d'atténuateurs à gaz. Concrètement, il serait intéressante mesurer la température électronique du plasma et modifier le modèle pour considérer distributions d'énergie électroniques non-maxwelliennes. Un changement dans la température électronique changerait les coefficients de diffusion et les taux de recombinaison, et pourrait exprimer les différences observés entre le modèle et l'expérience.

Le modèle peut être aussi utilisé dans de dessin et opération des atténuateurs a gaz présentes et futures, comme outil pour prédire l'absorption du faisceau X a partir de la géométrie de l'atténuateur et des condition initiaux. Finalement, il est possible aussi appliquer le modèle à sources X de lasers à électrons libres (FEL par ses sigles en anglais), considérant les différences dans la structure temporelle de ces sources et a différent pression a laquelle les atténuateurs à gaz de FELs opère.